



*Università degli Studi di Firenze*

*Scuola di Ingegneria*

*DIEF - Department of Industrial Engineering of Florence*

---

PhD School: *Energetica e Tecnologie Industriali ed Ambientali Innovative*

Scientific Area: *ING-IND/09 - Sistemi per l'energia e l'ambiente*

# MEASUREMENT OF HEAT TRANSFER DISTRIBUTION OF COOLED REAL GEOMETRY USING INFRARED THERMOGRAPHY

**PhD Candidate:** ING. ASIF ALI

**Tutor:** PROF. ING. BRUNO FACCHINI

**CoTutor:** ING. ALESSIO PICCHI

**PhD School Coordinator:** PROF. ING. MAURIZIO DE LUCIA

---

XXXI PhD School Cycle - 2016-2019



*To my late father,  
because I hope you're proud of me,  
wherever you are.*

*To my mother,  
because you always trusted me,  
your love only allowed me to reach this goal.*

*To my wife,  
because you've always been beside me,  
every day you make me a better man.*



# Acknowledgments

*First and foremost, I would like to thank God Almighty for giving me the strength, knowledge, ability and opportunity to undertake this research study and to persevere and complete it satisfactorily. Without his blessings, this achievement would not have been possible.*

*In my journey towards this degree, I have found a teacher, a friend, an inspiration, a role model and a pillar of support in my Guide, **Professor Bruno Facchini, Director, Department of Industrial Engineering, University of Florence**. He has been there providing his heartfelt support and guidance at all times and has given me invaluable guidance, inspiration and suggestions in my quest for knowledge. He has given me all the freedom to pursue my research, while silently and non-obtrusively ensuring that I stay on course and do not deviate from the core of my research. Without his able guidance, this thesis would not have been possible and I shall eternally be grateful to him for his assistance.*

*I have great pleasure in acknowledging my gratitude to my colleagues and fellow research scholars at HTC research group, Department of Industrial Engineering, University of Florence, **Dr. Alessio Pichi** and **Dr. Lorenzo Cocchi** in ensuring that the fire keeps burning and being there at times when I required motivation and propelling me on the course of this thesis and also for assisting me in collation of data for my research. Their support, encouragement and credible ideas have been great contributors in the completion of the thesis.*

*I also want to thank all the other past and present colleagues which made every day of these years pleasant both inside and outside the University:*

*Prof Calo, Antonio, Lorenzo M., Daniele, Davide, Lorenzo W., Sabrina, Tommaso F., Andrea, Dominique, Matteo N. , Lorenzo P., Carlo A.E., Tommaso L., Matteo P., Leonardo, Simone, Tommaso D., Piercarlo, the lab guys Daniele, Guilo, Riccardo, Tommaso B., Tommaso L. and Valter,. These few lines are not sufficient to express not even a part of my gratitude to all of you.*

*My acknowledgement would be incomplete without thanking the biggest source of my strength, my family. The blessings of my late parents **Mrs.Islam Bibi & Mr. Amir Zada** and the love and care of my wife **Dr. Shezr e anam Chaghtai** and her family, and of course my prime source of ideas, my brothers and sisters who never let things get dull or boring, have all made a tremendous contribution in helping me reach this stage in my life. I thank them for putting up with me in difficult moments where I felt stumped and for goading me on to follow my dream of getting this degree. This would not have been possible without their unwavering and unselfish love and support given to me at all times.*

*I would like to dedicate this work to my late father **Mr. Amir Zada** whose dreams for me have resulted in this achievement and without his loving upbringing and nurturing; I would not have been where I am today and what I am today. Had it not been for my father's unflinching insistence and support, my dreams of excelling in education would have remained mere dreams. I thank my father with all my heart and I know he is up there, listening, watching over me and sending me her blessings constantly and is my guardian angel.*

*This one is for you " lala ".*

*Asif Ali*

# Abstract

Over the years, gas turbine industry is continuously exploring different methods to increase the turbine inlet temperature for improving the specific power output and thermal efficiency of gas turbine engines, which leads to thermal loads for the engine components, which are usually managed thanks to the introduction of complex internal cooling systems. For this reason, it is necessary to develop tools able to accurately and quickly estimate thermal loads on turbine components. Typical experimental methods for assessing the heat transfer characteristics of such systems commonly rely upon scaled-up models investigated at nearly ambient conditions, since the size and operating environment of real engine parts make it extremely difficult to perform direct measurements. By doing so, however, many geometric and flow features of the real cooling system get lost, since the studied geometry is ideal and measurement constraints often require a simplification of the system itself. So there is a need for the development of a non-invasive, non-destructive, transient inverse technique which allows testing of real turbine blades temperature measurements. A much more reliable evaluation of cooling performance would thus be obtained by studying the real hardware, which requires the development of a suitable technique. As an additional advantage, a similar method could also be employed for in-line inspection of manufactured parts, as to clearly identify faults and defects before the actual installation. The aim of this work is to present the development and application of a measurement technique that allows to record internal heat transfer features of real components. In order to apply this method, based on

similar approaches proposed in previous literature works, the component is initially heated up to a steady temperature, then a thermal transient is induced by injecting cool air in the internal cooling system. During this process, the external temperature evolution is recorded by means of an IR camera. Experimental data are then exploited to run a numerical procedure, based on a series of transient finite-element analyses of the component. Then two different approaches can be followed, which will be referred as fluid model method and regression method respectively.

In fluid model method at the end of transient, finite element output external surface temperature is compared to the one which is obtained with experiment and the convective internal heat transfer coefficient is iterated continually with a root finding algorithm until the convergence between them is achieved. The coolant temperature will be updated during the transient with the help of a fluid model. This approach works very well for simplified geometries, in which convective internal heat transfer coefficient converges specific value but as we move to more complex geometries it may diverge. The reason is the inability of the fluid model to find accurate coolant temperature at certain regions, so a second approach is introduced for more complex geometries, the regression which is a modification version of the first approach.

In the regression method, the test duration is divided into an appropriate number of steps and for each of them, the heat flux on internal surfaces is iteratively updated to target the measured external temperature distribution at the end of step. Heat flux and internal temperature data for all the time steps are eventually employed in order to evaluate the convective heat transfer coefficient via linear regression. This technique has been successfully tested on a cooled high-pressure vane of a Baker Hughes heavy-duty gas turbine, which was realised thanks to the development of a dedicated test rig at the University of Florence, Italy. The obtained results provide sufficiently detailed heat transfer distributions in addition to allowing to appreciate the effect of different coolant mass flow rates. The methodology is also capable of identifying defects, which is demonstrated by inducing controlled faults in the component.



# Contents

<b>Contents</b>	<b>v</b>
<b>Nomenclature</b>	<b>vii</b>
<b>1 Introduction</b>	<b>1</b>
1.1 Background of present research . . . . .	1
1.2 Gas turbine cooling systems . . . . .	4
1.2.1 Internal cooling systems . . . . .	6
1.2.2 Pin-Fins . . . . .	9
1.2.3 Dimples . . . . .	10
1.2.4 Impingement cooling . . . . .	11
1.3 Problem overview . . . . .	12
1.4 Thesis outline . . . . .	16
<b>2 Proposed Methodology</b>	<b>19</b>
2.1 Fluid Model Method . . . . .	19
2.1.1 Experimental Part . . . . .	20
2.1.2 Finite element analysis part . . . . .	21
2.1.3 Fluid Model Method Issues . . . . .	25
2.2 Regression . . . . .	28
2.2.1 Advantage of regression . . . . .	31
2.2.2 Disadvantage of regression . . . . .	31

<b>3</b>	<b>Experimental Test Rig</b>	<b>33</b>
3.1	Generic layout of the test rig . . . . .	33
3.1.1	Heating system . . . . .	34
3.1.1.1	Oven . . . . .	34
3.1.1.2	Variac . . . . .	37
3.1.1.3	Guide rail with carriage . . . . .	38
3.1.2	Air supply system . . . . .	38
3.1.2.1	Pressure regulator . . . . .	39
3.1.2.2	Coriolis flow-meter . . . . .	40
3.1.2.3	3-way solenoid valve . . . . .	40
3.1.3	Data acquisition system . . . . .	41
3.1.3.1	ThermoVision <sup>TM</sup> A40M . . . . .	41
3.1.3.2	Thermocouple . . . . .	43
3.2	Paint calibration . . . . .	43
3.2.1	Emissivity vs angle . . . . .	45
3.3	Mirror selection . . . . .	46
3.4	Test procedure . . . . .	49
3.5	Data postprocessing . . . . .	52
<b>4</b>	<b>Preliminary Test Cases</b>	<b>55</b>
4.1	Circular duct . . . . .	55
4.1.1	Re 50,000 . . . . .	58
4.1.2	Re 75,000 . . . . .	64
4.1.3	Re 25,000 . . . . .	65
4.1.4	Nu vs Re . . . . .	65
4.1.5	Uncertainty analysis . . . . .	66
4.2	Blade with U-bend internal channel . . . . .	67
4.2.1	Re = 41220 case . . . . .	71
4.2.2	Effect of Re number . . . . .	75
4.2.3	Comparison with literature data . . . . .	76
4.2.4	Concluding remarks . . . . .	77

---

<b>5 Industrial Application</b>	<b>79</b>
5.1 BH's engine nozzle . . . . .	79
5.1.1 Test rig rearrangement for the vane . . . . .	80
5.1.2 Camera view . . . . .	81
5.1.3 Replicating engine condition . . . . .	83
5.2 Heat transfer calculation . . . . .	83
5.2.1 LTCM heat transfer coefficient . . . . .	84
5.2.2 Camera view limitation . . . . .	88
5.2.3 Final results . . . . .	89
5.2.4 Effect of Reynolds number . . . . .	97
5.2.5 Comparison with literature data . . . . .	99
5.3 Fault detection . . . . .	102
5.3.1 Half channel slots blocked . . . . .	103
5.3.2 Two channel slots blocked . . . . .	105
5.3.3 Impingement holes blocking . . . . .	106
5.4 Uncertainty analysis . . . . .	107
5.5 Concluding remarks . . . . .	108
 <b>Conclusions</b>	 <b>109</b>
 <b>List of Figures</b>	 <b>117</b>
 <b>List of Tables</b>	 <b>119</b>
 <b>Bibliography</b>	 <b>129</b>



# Nomenclature

## Acronyms

<i>FEM</i>	Finite Element Analysis
<i>HTC</i>	Heat Transfer Coefficient
<i>IR</i>	Infrared camera
<i>LTCM</i>	Lumped thermal Capacitance Model
<i>LE</i>	Leading edge
<i>PS</i>	Pressure side
<i>SAS</i>	Secondary air system
<i>SS</i>	Suction side
<i>Sec</i>	External area of the section of the geometry
<i>TLC</i>	Thermochromic Liquid Crystals
<i>TE</i>	Tailing edge
<i>TIT</i>	Turbine inlet temperature
<i>TC</i>	Thermocouple

## Greeks

$\lambda$	Thermal conductivity	$[W/mK]$
$\mu$	Dynamic viscosity	$[kg/ms]$
$\nu$	Kinematic viscosity	$[m^2/s]$
$\rho$	Density	$[kg/m^3]$

## Letters

---

$c$	Specific heat capacity	$[J/kgK]$
$D$	Diameter	$[m]$
$h$	Convective heat transfer coefficient	$[W/m^2K]$
$L$	Characteristic length	$[m]$
$Nu$	Nusselt number	$[-]$
$m$	Mass flow rate	$[g/s]$
$Re$	Reynolds number	$[-]$
$T$	Temperature	$[K]$
$t$	Time	$[s]$
$u$	Speed of free current	$[m/s]$
$U$	Velocity	$[m/s]$

### Subscripts

$amb$	Ambient temperature
$air$	Air temperature of the section
$bottom$	Bottom surface
$coolant$	Coolant Temperature
$Cr$	Crossflow
$E$	Exit of the section
$exp$	Experimental
$FEM$	Finite element model
$in$	Internal
$int$	Inlet
$I$	Inlet of the section
$i$	Current value
$initial$	Initial Temperature
$j$	Jet
$lx$	Left side
$out$	Outlet
$rx$	Right side
$ref$	Reference value
$s$	At specific instant or time
$sec$	Section of a geometry

<i>surface</i>	Duct surface
<i>top</i>	Top surface
<i>w</i>	Wall





# Chapter 1

## Introduction

The present work fits within the background of gas turbine cooling, a important design branch which led to past, current and future enhancement of such engine. The context of this research work as well as its focus and objective in alliance to the present available knowledge will be discuss in this chapter.

### 1.1 Background of present research

The most widely employed device in both power generation and propulsion is the gas turbine till present day. The reasons behind such success is the combination of different favourable features like the large power-to-weight ratio, the high reliability and lifespan and the short start up time. These characteristics lead the gas turbine to be an almost universal solution for aircraft propulsion and to an increasingly extensive use for electricity production. Because of these feature it is the only universal solution for aircraft propulsion and also use for electricity production in an increasingly extensive manner. Driven by both these environments, the global gas turbine market size is expected to register an average annual growth rate of 4.8% in the period 2018-2025 [1]. By considering power generation only, increase in growth prospects for gas turbine are driven by the combination of the increasing global energy demand and

the expanding environmental consciousness, which goes towards reduction of pollutant emissions and greenhouse gases. Previously the increase in power generation from renewable energy sources which requires a higher operational flexibility from the other power plants, provide a non-programmable output even in a very limited time frame. This requirement can be adequately satisfied by gas turbine engines, which can be started within minutes and ramped up and down quickly [2]. Keeping two aspects in mind, the lower carbon emissions and the higher efficiency, gas turbine provides satisfactory results in comparison with other combustion-based power generation applications (e.g. coal-fired plants). Lower emission is achieved because most of the gas turbine used natural gas as employed fuel. Over the years these two aspects increases the employment of gas turbines [1]. On the other side, as considering the propulsion employment in aviation, ICAO projects that global passenger traffic will grow at 4.6% annually to 2032, and that freight traffic will grow at 4.4% annually over the same period [3]. Around 2% of the overall human carbon emissions [4] nowadays is caused by aviation, but the expansion of this sector will dramatically increase this percentage if no counter-measurements are taken [5]: as a result, the desire for more energy efficient and sustainable aero engines is increasingly growing. So development of the gas turbine is necessary because of its expanding employment: increasing the performance of such devices is positive both from an economic and an environmental point of view. In this case the engine performance, both in terms of specific power output and efficiency, is directly bound to the temperature of the gases entering the turbine and the overall pressure ratio of the thermodynamic cycle. The relation between turbine inlet temperature (TIT) and the specific power output is shown in the chart of Figure 1.1 as a solid line, which shows the ideal machine output with 100% turbine efficiency and no leakage or cooling flows. The same charts also presents the corresponding values for some well known machines which report that, starting from the very first aero engines developed by Whittle and Von Ohain [6], the trend in gas turbine development leads towards ever increasing values of TIT in order to obtain higher efficiencies

and power outputs.

An increasingly severe environment is needed for the engine components

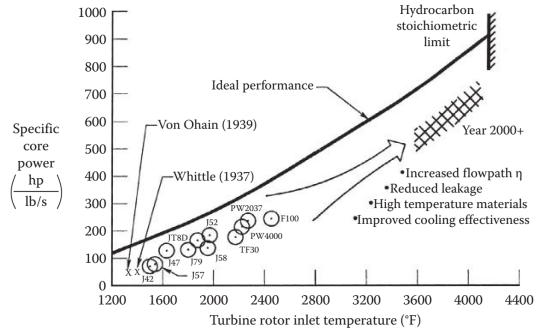


Figure 1.1: Improvement of specific power output with TIT [7].

to counter the flow temperature growth because this temperature increase may lead to lifespan reduction and eventually to component failure because of the resulting thermal stresses add to the existing mechanical and chemical ones. For highlighting this issue, a main research topic targeted on the development high temperature resistant materials like nickel and cobalt-based superalloys, innovative casting techniques (such as single-crystal solidification) and ceramic coatings. But still, present day temperature level have only been obtained thanks to the parallel development of cooling techniques for the most thermally stressed gas turbine components, which made it feasible to run these devices at largely temperature value exceeding the material melting point, as shown by fig 1.2.

Given the increasing importance of gas turbine cooling systems in the framework of the current research, more detail overview and discussion on such topic, and in particular the blade cooling systems, will be shown in the Section 1.2.

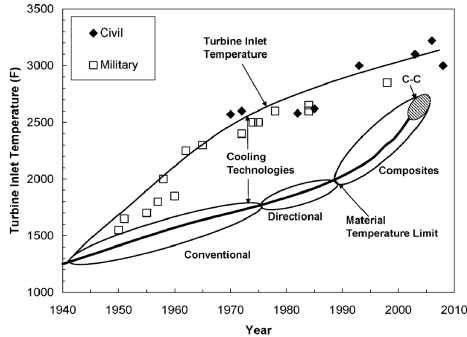


Figure 1.2: TIT and material limit temperatures during the years [8].

## 1.2 Gas turbine cooling systems

The first stage blades and vanes are the most thermally stressed components of a gas turbine engine: as a result, numerous cooling systems are implemented to such devices in order to keep the material temperature at an acceptable level. Depending upon the side of the blade wall to which the cooling schemes or systems are applied, they can be listed either as *internal* or *external*. These schemes normally employ the working fluid (air) as coolant, which is extracted from the compressor at several axial locations. Since some part of the working fluid does not evolve in the combustion chamber and into a part of the turbine leads to a decrease in engine specific power. Moreover, the used coolant is ejected into the main flow, and the consequent mixing results both the birth of secondary flows and a decrease in main flow enthalpy. It worth to consider that the air used as coolant shows poor heat transfer properties. But still these disadvantage are widely counter-balanced by the weight requirements and the small dimensions of this type of systems (which is especially appreciable in aerospace applications) and by the easy coolant procurement.

The air involved in the cooling scheme is not used to create work, so the usage of cooling system actually results to a penalty in term of thermodynamics cycle performance. This penalty increase as the amount

of air used as coolant grows. As a result, it is not applicable to face the increasing heat loads bound to the growing TIT trend by simply increasing the amount of coolant. This requires the growth of more and more suitable and effective cooling schemes, which can provide higher performance keeping the same coolant mass flow rate. Moreover, cooling systems are also subject to various constraints, which further increase the complexity of the design. First of all, a complex feeding system so-called secondary air system (SAS) is used for providing the air to the cooled devices., whose design is especially hard given the spatial constraints and the relevant effect of thermal displacements on the passage sections [9]. Relevant constraints are also provided by the shape of vanes and blades, which results by the size of such components (high pressure foils span can be as small as a few centimetres) and from the aerodynamic design of the main flow path. Finally, also the available manufacturing techniques need to be considered. As of today, turbine blade and vanes are realized by casting through the lost wax process [10]: as a consequence, the achievable complexity of the internal cooling structures is limited by the constraints of such technique. From this point of view, a promising trend is embodied by the recent development of additive manufacturing techniques, which would theoretically allow to realize much more complex geometries [11]: even if at the present day no blades or vanes realized through this technique are operational, other components are already employed both in power generation and aeronautic environments [12], and the development of new thermal treatments for increasing component strength and resilience is aimed at extending the application of this technique to cooled airfoils. Taking the aforementioned constraints into account, several blade and vanes cooling systems were developed in order to maximize the heat removed by the coolant flow. In this sense, cooled turbine components can be seen as highly specialized and complex heat exchangers [14]. The heat transfer process needs to be considered together with the associated pressure losses: as so, the design of the internal cooling systems requires an accurate knowledge of both fluid-dynamic and thermal phenomena in order to promote heat pickup while limiting pressure losses. Moreover,

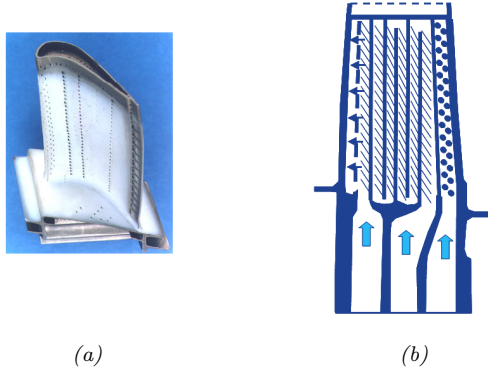


Figure 1.3: Example of cooled gas turbine blade (a) and corresponding internal cooling system (b) [13].

since present day cooling systems are based upon the combination of different techniques (see fig 1.3), the performance of the single cooling features may be compounded by their interaction, which requires that the whole cooling system is considered during the design phase. Finally, if the cooling of rotating equipment is considered, the effect of the intense centrifugal field on the internal flow also needs to be taken into account. In order to understand the different features of the system investigated in the present work, a quick overview of internal cooling systems for gas turbine airfoils will be provided in the followings.

### 1.2.1 Internal cooling systems

Internal cooling systems are the refrigeration methods in which inside the thermal load gas turbine component, heat transfer happens. This type of systems, being very distinguish from one another, shows some commonalities. The use of turbulent convective flows is involved in all highly cooled regions of high pressure turbine components: heat transfer enhancement methods make full use of the turbulent flow nature, with the objective to generate mixing mechanisms in the coolant flow that actively exchange cooler fluid for the heated fluid near the walls. According to the different systems, these mechanisms can include boundary layer disruption,

vortex generation and shear layers, [14]. Dissimilar to the convectional heat exchangers, gas turbine cooling systems do not rely upon an increase of the cooling surface area: even if this effect may actually be present and beneficial for heat transfer, this is not the primary goal of the systems.

The main basic cooling system is represented by radial ducts (fig 1.4):

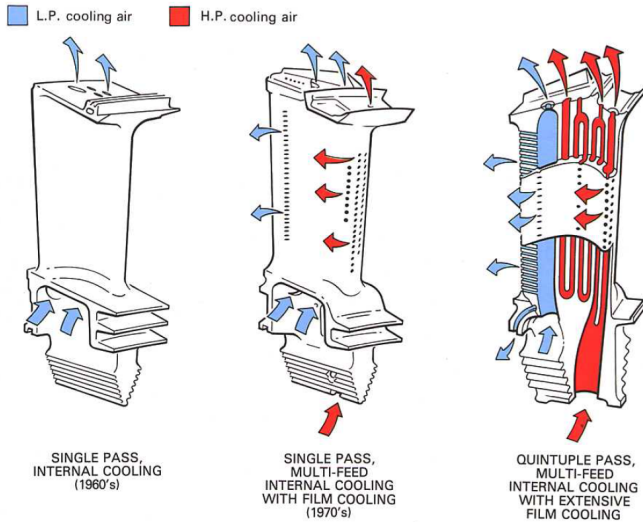


Figure 1.4: Radial single and multi-pass cooling channels,[15].

in their simplest form. Radial ducts are a series of smooth channels where the coolant flow enters from the hub of the blade, and sometimes also from the tip, and develops along the radial direction. To increase heat transfer coefficient, turbulence value or total surface cooled by the flow can be increased; HTC is increased going from a single pass to a multi-pass configuration, where total surface is widely increase. Such channels will be either single pass or multi pass: in this last case, radial straight sections are connected by U-bends, thus achieving a serpentine passage. In order to remove the heat from the blade material by means of solid conduction and internal convection, the coolant flow is circulated

inside the ducts. The used coolant is finally discharged from the blade tip. To design and manufacture the smooth duct is easy but it shows poor cooling effectiveness because of the development of thermal boundary layers and thick dynamic.

One way of increasing the heat transfer is the employment of turbulence promoters inside internal ducts. The most common used forms of such devices is the use of ribs, which is also known as turbulators, consist of trip strips arranged transverse to the bulk flow direction. Their function is to simply trip the boundary layer, thus increasing heat transfer by means of both increased flow field alteration and turbulence. In fact, the main flow separates after the rib and then reattaches after a recirculation vortex: this creates a local impingement zone, and thus a relatively high heat transfer region (see fig 1.5). The recirculation, separation and

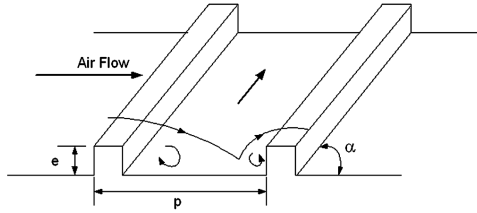


Figure 1.5: Scheme of flow field induced by ribs [16].

reattachment pattern is repeated for each rib, leading to a continuous heat transfer increase along the channel if multiple ribs are employed. Thanks to this system, surface averaged heat transfer coefficients within stationary, turbulated passages may be increased by factors from 1.8 to 2.8, while the friction factors or required pumping power are enhanced by factors from 3 to 10 [14]. Another way of improving internal ducts heat transfer is to use pin fins, which will be described below.



### 1.2.2 Pin-Fins

Pin-fins widely used in gas turbine trailing edge cooling, are prismatic support, generally having circular cross sections. For maximizing forced convection cooling, they are arranged orthogonally to the flow direction; the main advantage consists in enhancing heat transfer coefficient without increasing the airfoil blade thickness. The behavior of the flow around the pin fin is same as around a single cylinder: the coolant separates and wakes are shed downstream, whereas a horseshoe vortex forms upstream of the pin base, wrapping it and creating additional mixing. The pin fin not only provides flow disturbances, but also conduct thermal energy away from the heat transfer surface, and long pins can increase the effective heat

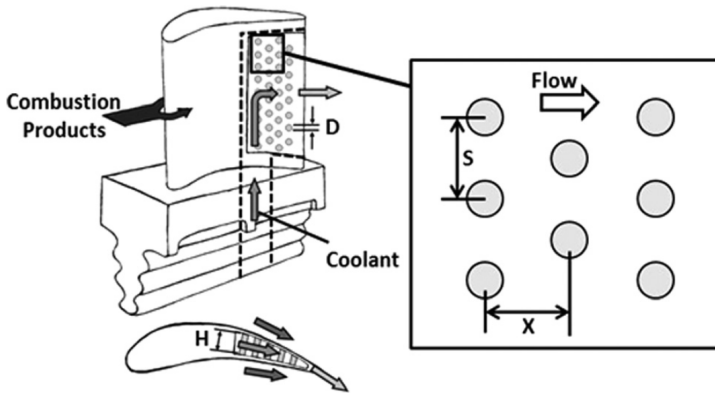


Figure 1.6: Schematic of a pin-fin array at the trailing edge of a gas turbine airfoil, [17].

transfer area. The shape, size, spacing (in both streamwise and spanwise direction) fillet radii dimensions, are all pin factors that can influence heat transfer performance. Pin fins are commonly employed to cool down the airfoil trailing edge, as their application strengthens the structure and enhances the heat transfer without thickening the cooling channel (see

fig 1.6) Most important correlations for pin-fin cooling are developed by VanFossen [18] and Metzger et al. [19] for short pin-fin arrays (height over diameter  $< 3$ ), and by Faulkner [20] for tall pin-fin arrays (height over diameter  $> 3$ ), as stated by Armstrong and Winstanley [21] in their review.

### 1.2.3 Dimples

A different cooling approach is exploited by the dimples (also known as concavities), which consist in an array of indentations along the internal surfaces. These are most usually spherical in shape, although a variety of other shapes have also been used, including tear-drop and triangular. Arrays of dimples are useful techniques for internal cooling because they create multiple vortex pairs which increases local Nusselt number distributions as they advect downstream. They are observable for the low pressure drop penalties which they create, which is because they do not protrude into the flow to produce significant amounts of form drag. With this advantages, dimples offer benefits for cooling later turbine stages where lower pressure cooling air is employed. They are also advantageous because the pressure drop that they create through an airfoil passage is relatively low, which permits favorable pressure margins to be maintained in parts of the airfoil interior which are further downstream [22, 23]. Another advantage is dimple manufacture removes material from internal cooling passage components, in contrast to rib turbulators and pin fins, which need addition of extra weight and material [22]. Heat transfer in a dimpled channel is typically 2 - 2.5 times greater than the heat transfer in a smooth channel with a pressure loss penalty of 2 to 4 times that of a smooth channel, while ribbed surface can have higher heat transfer augmentation but only with higher friction factor augmentation [22]. Dimpled surface performances show little dependence on Reynolds number and channel aspect ratio, but dimple size, dimple depth, distribution, and shape can strongly affect heat transfer distribution in the channel [24]. The main advantage of dimples is the low pressure drop they produce, despite not being able to provide as much heat transfer increase as the

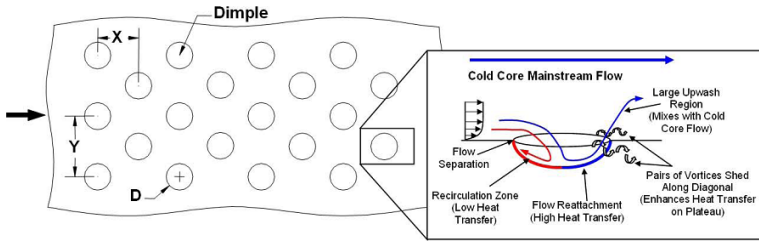


Figure 1.7: A typical test model for dimple cooling studies with a conceptual view of dimple induced secondary flow, [24].

protrusions (ribs or pin fins): in particular, heat transfer enhancements ranging from 2 to 2.5 times over a smooth duct are possible with friction increases from 1.5 to 4 [14].

#### 1.2.4 Impingement cooling

For trailing edge(TE) and midchord of the airfoil both protrusions and concavities are effective ways to cool down, but considering the leading edge(LE) region it doesn't provides sufficient results. Impingement systems are commonly used for LE in many gas turbine cooling applications. The cooling air is forced to impinge on the blade or vane internal surfaces, and the increased level of turbulence that is generated increases the heat transfer considerably. Single jet impingement cooling is the application of a high velocity coolant mass flow ejected from a hole (or slot) and directed to the target surface. The jet first begins to spread due to intensive shear interaction with the surroundings in the free jet region, which produces entrainment of energy, momentum, mass, and energy. Simultaneously, as the shear layers surroundings the jet increase, the potential core - the region where the velocity is still equal to the bulk velocity - starts decline in width. Core is typically visible up to 6 - 7 jet diameters from the nozzle. Figure 1.8 presents an example of typical surface impingement induced by a single jet. Flow field of an impinging jet from single round

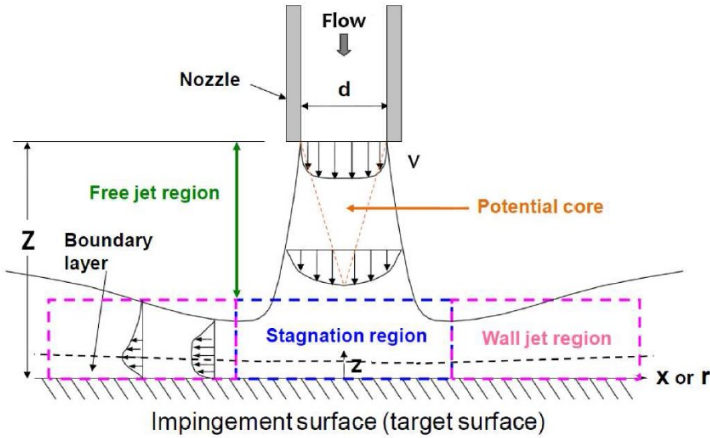


Figure 1.8: Scheme of flow regions in an impingement jet, [25]

nozzles can be divided into three characteristic regions: free jet region, stagnation region and wall jet region. Many researcher already worked in the impingement cooling area: which is based upon studies performed on a single impinging jet, like the one of Marti [26], Gardon and Akfirat [27] or Bradbury [28], that studied the details of fluid mechanics in a free jet. Sparrow and Wong [29] studied the effect of jet-to-target plate spacing for a single jet and Goldstein et al. [30] produces variations in single jet heat transfer with considerations of Reynolds number and again by changing jet-to-target plate spacing; Goldstein and Seol [31] compete the heat transfer between a row of circular jet and a slot jet, while an analysis of the crossflow impact on the jet structure was done in [30] by Goldstein and Behbahani.

### 1.3 Problem overview

The effectiveness of any internal cooling scheme can be defined by measuring the convective internal heat transfer coefficient: which is a di-

rect product of the internal cooling scheme which consists of impingement, pin fin and many other cooling features. During the years, a wide range of experimental methodologies has been developed to measure convective heat transfer, each suitable for different kinds of environments and applications. Such techniques differ for the employed experimental procedure (transient or steady-state) and for the physical quantities evaluated to determine heat transfer (temperature or heat flux). According to such differences a classification can be performed, a scheme of which is reported in fig 1.9. For a deeper discussion on experimental techniques, the reader can refer to von Wolfersdorf and Weigand [32].

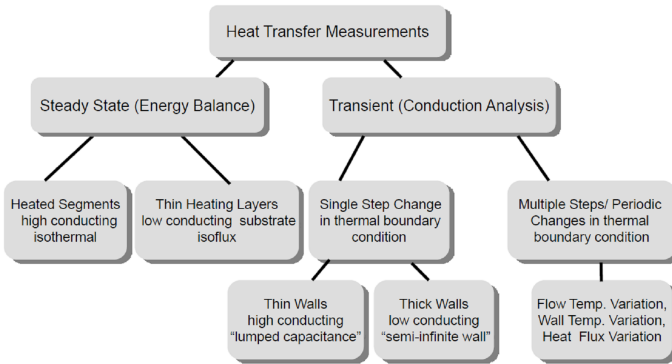


Figure 1.9: Classification of heat transfer measurement techniques [32].

In order to obtain space resolved heat transfer coefficient distributions, a point-by-point temperature measurement is required, which is usually performed by means of optical measurements which consists of liquid crystal thermography and Infrared thermography. Most of these techniques are implemented on simplified models representing the actual significant turbine blade part. For example, Park et al. [33] studied the performance of different ribbed rectangular channels using the heater foil technique. These channels were to be seen as simplified models representing any cooling passage in a gas turbine blade. Liquid crystal thermography combined with 180° bend model was used by Ekkad and Han [34] and by Pape et

al. [35]. To allow optical access to the inner surface these models were made of Plexiglas. Liquid crystals applied on the inner surfaces enable the measurement of heat transfer coefficient spatial distribution. A wide number of researchers also used Plexiglas for modeling the actual internal cooling schemes as described by Poser et al. [36]. If transient techniques are employed, much more effort is needed to evaluate liquid crystal results because of the complexity of the internal cooling scheme's passage. Poser et al. [37] described an advanced evaluation technique which considered local internal air temperature within the model.

Infrared thermography can also be used for measuring external surface temperature of turbine blades in a nondestructive way during a thermal transient test. This measured temperature distribution can be used as qualitative evaluation of appropriate or inappropriate blade cooling technique. A thermal transient is induced by flowing a medium through a turbine blade from some known thermal state at initial time ( $t = 0$ ). Infrared thermography has some advantages over liquid crystal thermography, i.e. it is less sensitive to illumination and viewing angle [38]. A number of researchers used IR thermography for measuring heat transfer coefficient. Bantel and Mack [39] developed an early version of this methodology in which they forced hot gas to pass through a channel and then observed the transient response of the channel with the help of IR camera. IR thermography was also used for quantitative evaluation of defects in any metal surface and gas turbine blade ([40], [41]). Beckeis et al. [42] and Stiglich et al. [43] used quartz lamp for heating purpose and then introduced coolant to induce transient response in order to retrieve information about the internal heat transfer distribution. In both methods the thermal response was compared to a known standard for indirect evaluation of the heat transfer distribution. Lynch and Thole [44] used IR thermography for endwall HTC evaluations; Cocchi et al. [45] and Goodro et al. [46] applied IR techniques for a detailed analysis of impingement jets. An extensive review of IR thermography application to heat transfer measurements was performed by Carlomagno and Cardone [47].

One of the first attempts to get complete a internal heat transfer coefficient distribution of a metallic airfoil prototype was done by Nirmalan et al. [48]. The scheme of this approach is shown in the fig 1.10. The

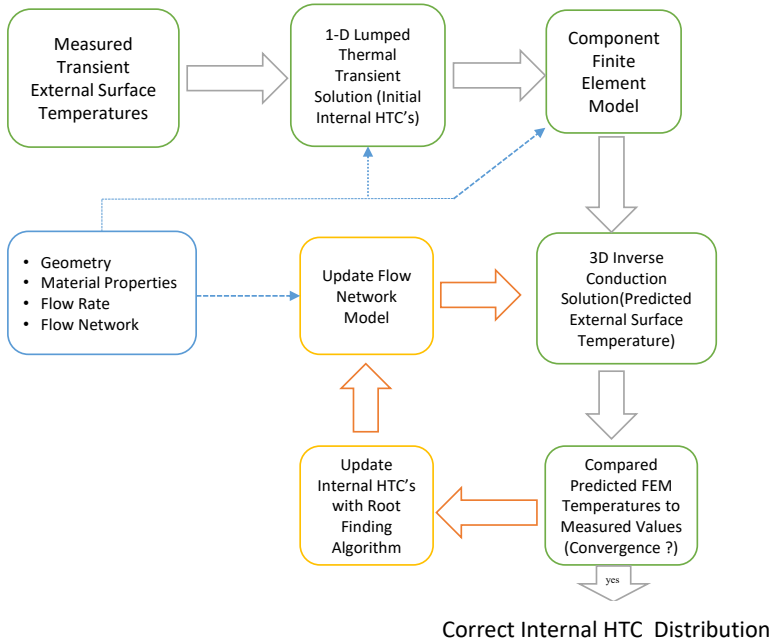


Figure 1.10: Schematic of Nirmalan approach [48].

external surface temperature during the transient test was recorded with a IR camera. Then an inverse conduction methodology was implemented with the help of finite element model starting with heat transfer coefficient obtained from lumped thermal capacitance model with the assumption of one-dimensional wall of finite thickness and no conduction within the wall. A constant coolant temperature inside the geometry was considered during the transient test duration. They extended this method to quantify the flow features for film cooling holes by comparing the results with

a known standard one [49]. Heidrich, P. [50] applied a little different approach by taking into account the conduction within geometry wall and then solving a one dimensional inverse heat transfer problem. A slightly different approach was employed by Heidrich et al. [50] and Egger et al. [51],[52], which retrieved the internal heat transfer distribution using an improved lumped thermal capacitance model, capable of taking into account lateral conduction and external heat losses. A similar, full 3D approach was also employed by Christensen and Mathison [53] to obtain the cooling features of a straight duct with different inlet geometries. This brief review highlights that a growing interest is present in the research community regarding the possibility of performing heat transfer measurements on real scale, high conductivity samples. Moreover, the recent development of rapid prototyping and additive manufacturing techniques makes the availability of fast and reliable techniques for real hardware testing even more desirable. The present work fits within this research trend, since its goal is to develop and apply a measurement procedure for internally cooled metal samples, which can be applied both to evaluate the cooling performance and to reveal possible defects of the investigated device.

## 1.4 Thesis outline

In this research activity a heat transfer coefficient measurement methodology is proposed and implemented on real gas turbine cooled geometry. First baseline geometries, a circular duct and a blade with U-bend internal channel were chosen for investigation through this methodology. After finding some satisfactory results for each case we moved to a real gas turbine cooled geometry, a high pressure nozzle provided by Baker Hughes. The obtained results were compared against correlation data and a good agreement were retrieved . The manuscript will be organized as follows:



**Chapter 1** In this chapter some introduction to the topic, gas turbine cooling systems will be revised. Different techniques which are very useful and already implemented will be explained in details. Convective heat transfer coefficient measurement methodologies which are usually implemented on scaled up models are available in the literature; these may be beneficial in most of the cases but still some real geometric and flow features will be not evaluated properly. This is one of the reasons for this work to suggest and investigate a procedure which can be implement for the evaluation of convective heat transfer coefficient of real gas turbine cooled geometry.

**Chapter 2** For achieving the desire goal a procedure is proposed on the base of Nirmalan [48] technique. We will use two different approaches during the procedure, one which will be named as fluid model method and the other which will be refereed as regression method. Both approaches consists of two sub parts: experimental and finite element modeling. The first method is the replication of Nirmalan technique on a real geometry while the regression is the modification of Nirmalan technique used for implementing on a BH's engine nozzle.

**Chapter 3** The experimental part of the methodology will be carried out with the help of a test rig setup, which consists of three sub systems: a heating system, in which the geometry will be heated to a certain temperature, an air supply system which will provide the coolant to the geometry for inducing a thermal transient, and the data acquisition system which will record the external surface temperature history during the transient. We will need some data processing procedure for converting the obtained 2D data into 3D data.

**Chapter 4** To develop the proposed methodology, two preliminary test cases, a circular duct and blade with U-bend channel, were selected. The circular duct is the baseline geometry which is of axisymmetrical nature. The obtained data will be compared with a number of available literature

correlations. Blade with U-bend channel will require a full 3D mapping procedure, which will be implemented for obtaining a full 3D surface temperature history during the transient test.

**Chapter 5** After implementing the procedure on the preliminary test cases we move to Baker Hughes engine nozzle. First it is already established in chapter 2, that the regression approach provides more reliable and converging results for this geometry. Different tests were performed with different Reynolds numbers to investigate the heat transfer phenomenon, results will be compared with open literature correlations. This method is also used for detecting controlled faults in the cooling network of this vane.

## Chapter 2

# Proposed Methodology

The detailed study which is illustrated in chapter 1 points that the definition and quantification of convective heat transfer coefficient of any cooled gas turbine system is very essential. Many researchers demonstrate a number of methods to find heat transfer coefficient but mostly used scaled-up model of the actual geometry. In this chapter we will discuss in details about methodology used for measuring heat transfer coefficient of real geometry. Depending upon the complexity of the geometry we will use two different methods a fluid model method and regression. Both methods are actual based upon on Nirmalan approach ([48]) but the second one, the regression is a modified version of this approach, details about them will be explained in the following sections.

### 2.1 Fluid Model Method

The complete procedure for finding internal heat transfer coefficient of geometry is described in the following fig 2.1. The overall procedure is further subdivided into two parts experimental and finite element analysis.

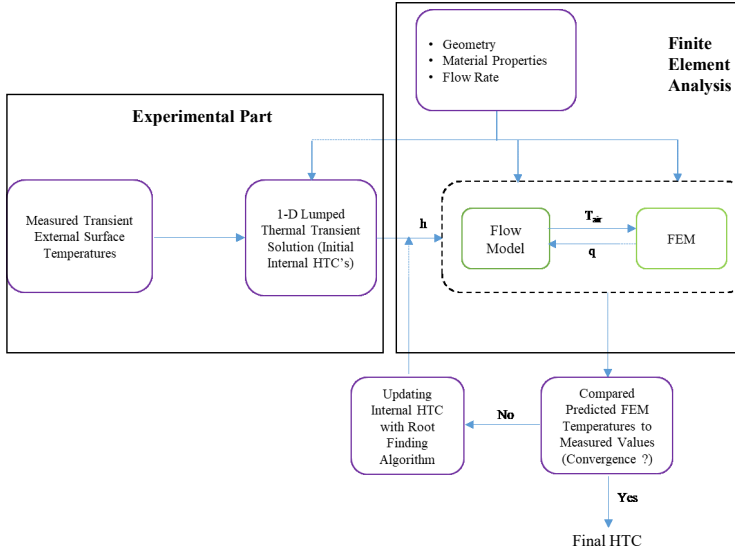


Figure 2.1: Fluid Model Method.

### 2.1.1 Experimental Part

The first step of the procedure is to place any geometry of interest on test stand and start heating it up to a known thermal state ( $t = 0$ ). Coolant is then introduced into the geometry for inducing a thermal transient on the internal surfaces. By knowing the initial temperature distribution of the geometry, the heat source, the coolant temperature and the flow rate, a controlled thermal transient can be induced. During the actual test ( $t > 0$ ) the heat source must be uniform or at zero value and flow rate and temperature of the coolant must be known. During the thermal transient, the external surface temperature  $T_s(x, y, z, t)$  history of the geometry is recorded with the help of IR camera (Sampling frequency of 25 Hz and Spatial Resolution 1 to 3 mrad). The thermal history of each surface location contains response data related to internal surface heat transfer coefficient.

After getting the surface temperature of the geometry during the transient test, an initial attempt is made to calculate HTC by using the following lumped thermal capacitance model (LTCM) by assuming that the geometry can be represented by a simple 1D wall of finite thickness and neglecting the conduction laterally within the wall.

$$\frac{T_s(t) - T_{initial}}{T_{coolant} - T_{initial}} = e^{-at} \quad (2.1)$$

where  $a = h/\rho l C$

$h$  is the heat transfer coefficient,  $l$  is the wall thickness,  $C$  is the specific heat capacity and  $\rho$  is the density.  $T_s(t)$  is the surface temperature at that time instant,  $T_{initial}$  is the initial temperature of the surface at time  $t = 0$  and  $T_{coolant}$  is the coolant temperature.

### 2.1.2 Finite element analysis part

To find the spatial variation in the heat transfer and obtaining full 3D corrections for the local effect of conduction, the geometry with its material properties are modeled by finite element model using ANSYS Mechanical which is our second part of methodology. The FEM model is executed for the same thermal transient period with the same known boundary conditions like initial external temperature, coolant flow rate as well as its temperature. It is provided with initial internal HTC obtained from LTCM, which allows us to improve the stability of the procedure by imposing a physically meaningful first attempt distribution. External convection (which is evaluated by a suitable correlation, [54]) and radiation are also set on the outer surface although their contribution to the total heat transfer is very low as compared to internal HTC. FEM model output provides the solid temperature at all nodes of the geometry, including the external surface temperature distribution. In the case of simplified geometry like circular duct only a  $1^\circ$  section of the duct was actually simulated in order to reduce the computation cost, which is possible because of axisymmetrical geometry and boundary conditions. But for other more complex geometries which are not axisymmetrical

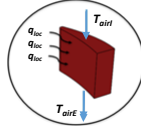


Figure 2.2: A section of the geometry.

such assumption was not taken. A FEM of the actual geometry was implemented considering all other boundary conditions.

In order to allow a continuous update of both material temperature and fluid conditions, the total transient test duration is subdivided into further time steps. For each time step the FEM is executed with same HTC value but with updated other boundary conditions like initial temperature and coolant temperature. The initial temperature for the first time step is obtained from the IR data, after that the final FEM output temperature of each previous time step acts as input for the next time step. For each time step the coolant temperature inside the geometry is updated continuously by using a fluid model.

Fluid model is based on a section-by-section energy balance between solid and fluid. The geometry is divided into a series of stream wise sections. Heat flux at each of these sections along the inner channel of a geometry can be found by using the following equation.

$$Q = h \cdot Sec \cdot (T_w - T_{air}) \quad (2.2)$$

Where  $Q$  is the heat flux,  $h$  is the heat transfer coefficient,  $Sec$  is the area of the section,  $T_w$  is the average surface wall temperature of the section and  $T_{air}$  is the average air temperature in that section. Now using energy balance equation we find the  $T_{airE}$  at the exit the section. The figure 2.2 shows a section of internal channel of a geometry.

$$T_{airE} = T_{airI} + Q/m_{sec} \cdot C_p \quad (2.3)$$

$T_{airE}$  represents the air temperature at exit of the section,  $T_{airI}$  is the section inlet temperature,  $m_{sec}$  is the mass flow rate at the section and  $C_p$  is the specific heat capacity. Since  $T_{air}$  in eq. (2.3) depends upon  $T_{airE}$  its value is initialized with the inlet air temperature  $T_{airI}$  and then recalculated as soon as  $T_{airE}$  value is available. This cycle is repeated until convergence. In this way the fluid temperature along the internal channel of the geometry in each section is calculated. The fluid model updates the air temperature at each time step according to the geometry surface wall temperature which changes after each time step. This fluid model is implemented with help of a MATLAB macro, which reads all the inputs required for calculating air temperature after each time step and updates this to FEM.

At the end of transient test duration, FEM output surface temperature is compared with experimental one obtained with IR camera. If the LTCM HTC value represents the reality then both temperatures must be the same, but if this is not the case then the temperature difference (*Tempdiff*) between them can be used to improve the value of the internal HTC. For finding the correct internal HTC an iterative scheme is followed (which is described by Fig. 2.3) in which we updates the HTC until convergence is achieved. Starting with LTCM HTC value, then the onward iterations are based upon a secant method which is described by equation 2.4.

$$h_{i+1} = h_i - \frac{Tempdiff_i}{(Tempdiff_i - Tempdiff_{i-1})}(h_i - h_{i-1}) \quad (2.4)$$

Where  $h_{i+1}$  is the updated heat transfer coefficient value,  $h_i$  and  $h_{i-1}$  are HTC value from the two previous iterations while  $Tempdiff_i$  and  $Tempdiff_{i-1}$  are the temperature differences between FEM and experimental values at the two previous iterations. Since two starting points are required in the secant method, a second attempt HTC is imposed starting from the first attempt  $h$  and  $Tempdiff$ . The second iteration of the HTC will depend upon the  $Tempdiff$  between the FEM surface temperature ( $T_{FEM}$ ) and the experimental one ( $T_{exp}$ ). If  $T_{FEM} < T_{exp}$  then 1.1 is multiplied with  $h_{i-1}$  (First iterated LTCM HTC value) other-

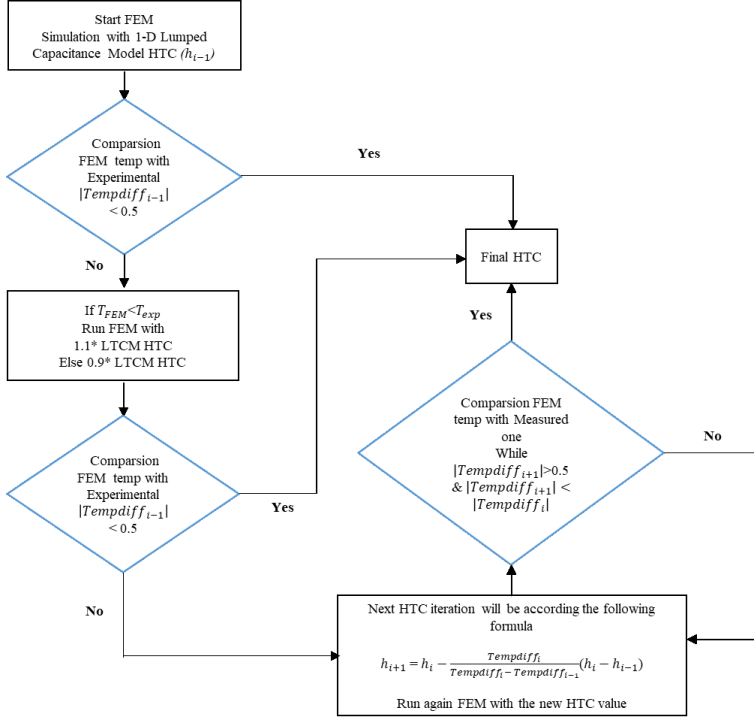


Figure 2.3: Post processing procedure flow chart.

wise 0.9 ( if  $T_{FEM} > T_{exp}$ ) is multiplied. Iteration is performed until the convergence criteria is fulfilled i.e. root mean square value of  $Tempdiff_i$  must be less than a specified value( e.g. 0.5 in the case of circular duct). Also keeping in check that the root mean square value of the temperature difference of the current iteration is less than the previous one( $Tempdiff_{i+1} < Tempdiff_i$ ) otherwise stop there.

This whole iterative procedure is performed automatically with the help of a MATLAB macro. MATLAB runs the FEM model for each time step, updating the boundary conditions for the next time step (i.e. initial temperature and coolant temperature) by executing the flow model. At the



end of the whole transient test duration the output will be compared with the experimental one and a new HTC based upon the scheme discussed above is calculated. The whole process will continue until the convergence criteria is achieved.

### 2.1.3 Fluid Model Method Issues

The fluid model which we used for updating the  $T_{air}$  during the thermal transient test is based upon some assumptions i.e. equal amount of air pass through each selected section of the geometry and assuming a known flow direction inside the geometry. Also the model is based upon energy balance equation, it doesn't consider any other phenomena( flow expansion, corresponding errors etc).

This model predicts very accurate  $T_{air}$  in the cases where the internal flow channel of the geometry is very simple and flow direction can be easily predicted i.e a circular duct or a blade with internal U-bend channel details of which will be discussed in the chapter 4. In both cases using this approach we obtained very reliable results.

But using this fluid model approach for a geometry (details of which will be discuss in chapter 5) with very complex internal cooling scheme which consists of impingement, pin batteries and channels doesn't provide the desired results. The reason behind this is that making an accurate assumption about the amount of air passing through a selected section and predicting the direction of flow inside such complex geometry is very difficult to obtain. Moreover as already mentioned that the fluid model is based upon energy balance equation and it doesn't consider any other phenomenon (like expansion) which may effect the temperature of the coolant inside the geometry.

Figure 2.4 shows the final iterated HTC distribution (for BH's nozzle) obtained with fluid model method for which the convergence criteria is achieved. The overall HTC distribution is very smooth on most of the vane but on trailing edge the value is erupt. Also if we continues to iterate HTC it diverges more and more. The reason behind this is the inability of the fluid model to calculate the accurate temperature of the coolant in

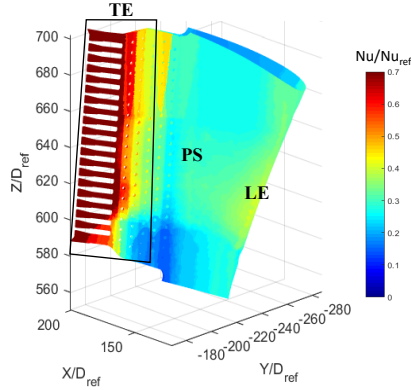


Figure 2.4: Final HTC distribution obtained with fluid model method

this region. The coolant temperature at a time step calculated by the fluid model is shown in the figure 2.5. The temperature of the fluid increases as we move from the leading to the trailing edge duct exit. The issue is that after a certain time the fluid model predicted temperature in the trailing edge channels becomes higher than the metal temperature, thus making the iterative procedure diverge. Indeed, thermocouple located approximately at the the exit of the TE ducts to investigate this phenomenon provided air temperature often lower than the inlet temperature. The one possible reason behind such drop of the temperature is expansion phenomenon which produce Joule Thompson effect not considered by our fluid model 2.5.

Now due to such drop of the temperature at trailing edge channels exit large amount of heat transfer take place in the area close to the exit. But our FEM model which is implemented with coolant temperature calculated by fluid model doesn't provide such heat transfer at the region because the coolant temperature is much higher as compared to the actual one measured with help of thermocouple. As in the description of fluid model method we iterated our next HTC using secant method which uses the temperature difference between FEM and experimental one shown

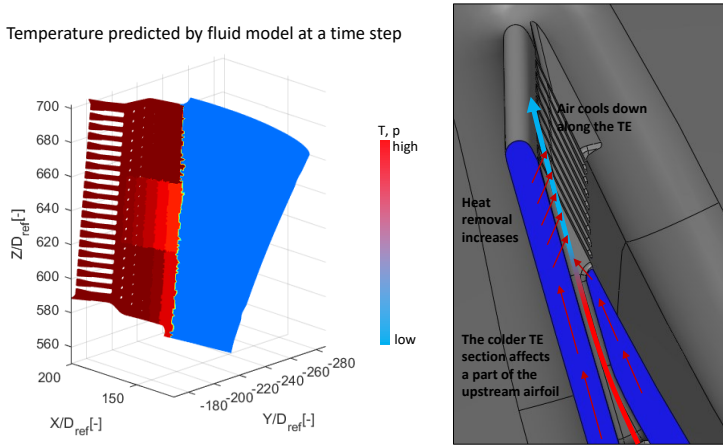


Figure 2.5: Coolant temperature calculated by fluid model vs actual temperature.

in figure 2.6. This temperature difference is obtained after executing FEM model with 3rd iterated HTC value. The temperature difference at trailing edge channel exit area is much higher than the remaining of the airfoil which almost close to  $-15\text{ }^{\circ}\text{C}$  because of lower heat transfer in the case of FEM. Now using this temperature difference value for the next iteration will provide very high value of the HTC in that region which can be observed from the fig 2.6. Further iteration will diverge the HTC value more because fluid model will predict higher temperature at TE exit than the measured one and the HTC value will never converge in this region. Although our fluid model works very reasonable in the cases of simplified geometries like circular duct and a blade with U-bend internal channel, it may not provide reasonable results as moving to more complex geometries because of the problem mentioned before. Now to overcome this issue another procedure was invented which we will be discussed in next section.

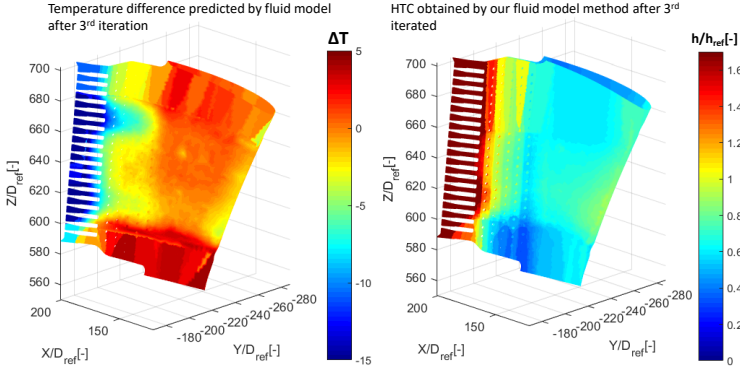


Figure 2.6: Temperature difference between FEM and Experimental one at 3<sup>rd</sup> iteration and Nu obtained at fourth iteration.

## 2.2 Regression

To overcome the limitations of our fluid model method another method is introduced. Now the variable of interest will be heat flux  $Q$  and we will not use the fluid model for updating the coolant temperature. In the previous method we compare the FEM output to the experimental one at the end of the transient test while the fluid model updates continuously the coolant temperature during the whole transient.

In the regression method we divide the total transient duration into further sub steps (i.e 4 sec sub-step for nominal case). For each sub-step duration the FEM model will be implemented with boundary conditions obtained at that sub-step like initial temperature of the geometry, initial HTC obtained with LTCM approach and any other boundary condition while the coolant temperature will be uniform along the whole geometry and will equal to the average value of the thermocouples reading insert at the inlet of the geometry. In other words, we will not use the fluid model for updating the coolant temperature but will use the thermocouples reading during that sub-step. The whole iteration process as shown in

the fig 2.3 will be followed, until the convergence between the FEM and experiment is achieved for that sub-step. Now, using final HTC iteration obtained at the end of a each sub-step , temperature of the coolant and wall temperature of the geometry during that sub-step we can calculate the average heat flux  $Q$  with the help of following equation 2.5.

$$Q = htc \cdot (T_{wall} - T_{air}) \quad (2.5)$$

At the end of each sub-step the heat flux is calculated as mentioned above. Then plotting heat flux  $Q$  against  $T_{wall}$  both obtained at the end of each sub-step and using linear regression the value of HTC can be obtained. As an example fig 2.7 shows the  $Q$  values against  $T_{wall}$  at single

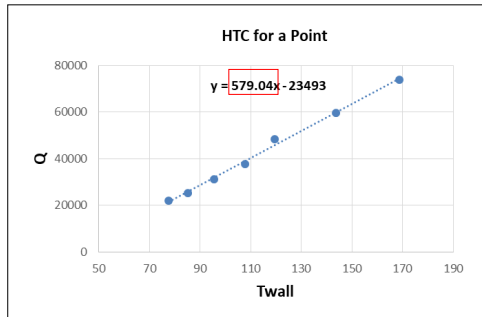


Figure 2.7: Heat flux vs  $T_{wall}$  for a single location for all 7 sub-step

location for each seven sub-step. Then by linear regression we got the HTC value at that location which is highlighted as slope of the line, which serve the linear fitting between  $Q$  and  $T_{wall}$  values (2.7). In this way we find internal HTC for all locations of the whole geometry. The following table 2.1 highlights the difference between the fluid model method and

Table 2.1: Comparison between fluid model method and regression.

	Fluid Model	Regression
<b>Transient FEM simulations</b>	One for the whole transient test duration	One for each sub-step
<b>Comparison between <math>T_{FEM}</math> and <math>T_{exp}</math></b>	Only at the end of the whole transient test	At each sub-step
<b>Target variable</b>	Convective heat transfer coefficient	Heat Flux
<b>Need for fluid model</b>	Yes	No

regression. Transient test duration in regression method is divided further into sub-step as compared to fluid model method. We don't need fluid model anymore because of this, we can easily avoid all issues we discuss in fluid model method.

Figure 2.8 show the HTC distribution of the airfoil obtained with both methods. The overall HTC distribution obtained with regression is much smoother as compared to fluid model one. Also we don't have any high erupt values as it is in the case of fluid model method specially on the TE.

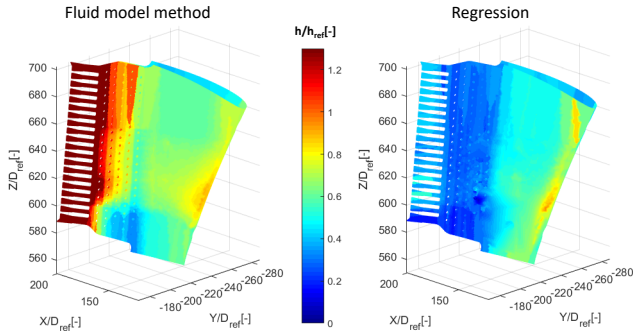


Figure 2.8: Comparison of HTC obtained by fluid model with the one obtained by regression

### 2.2.1 Advantage of regression

There are a number of advantages of regression method, the one of which is that in the regression method we don't require the fluid model. No fluid model also means that the need for underlying hypotheses relative to flow direction, local mass flow rate, etc is not revised now. These hypotheses may produce inaccurate results in the case of defects or different geometry with respect to the ideal one. Also the need to model local flow phenomena which are particularly difficult or impossible to evaluate doesn't affect results in the case of regression like expansion at trailing edge slots.

There is a larger tolerance to input data because now the main input in this case is the local temperature variation. There is improvement in the physical significance of the model because the experimental data obtained with the help of IR is used for comparison after each sub-step. This comparison of experimental data is performed all along the whole test while in the case of fluid model method it is performed once at the end of the test unreliable data can thus be easily identified and removed during the test.

### 2.2.2 Disadvantage of regression

One of the disadvantages of the method is that the HTC iteration using secant method is performed at the end of each sub-step while in the case of fluid model iteration at the end of whole transient test. So now we have more iteration cycle in the regression method leading to more noisy results as compared to fluid model method.

Also the sub-step duration needs to be defined keeping in mind that for having some heat transfer phenomenon to occur in a sub-step there must enough temperature difference between initial and final temperature of the step. We must not elongated sub-step duration because in between some necessary information will lost. Also we will considered only those step at which a reasonable temperature difference present because as we move along the transient test the difference decrease. So there is trade off

between accuracy and overall number of sub-step.



## Chapter 3

# Experimental Test Rig

The proposed methodology illustrated in chapter 2 consists of two parts one is the experimental one while the other one is finite element modeling. In the experimental part we will need to heat the desired geometry to a certain temperature, than a coolant is advanced inside the geometry which will induces a thermal transient, during which the IR camera will record the external surface temperature history. For this we need to design a test rig which will perform the said task. In this chapter we will explain in detail the test rig setup, experimental apparatus used in the experiment, the overall data acquisition system and the data postprocessing procedure.

### 3.1 Generic layout of the test rig

The overall generic layout of the complete test rig setup is shown in the fig 3.1. It consists of three sub systems which are listed below and will be explained in detail one by one.

1. Heating system
2. Air intake system
3. Data acquisition system

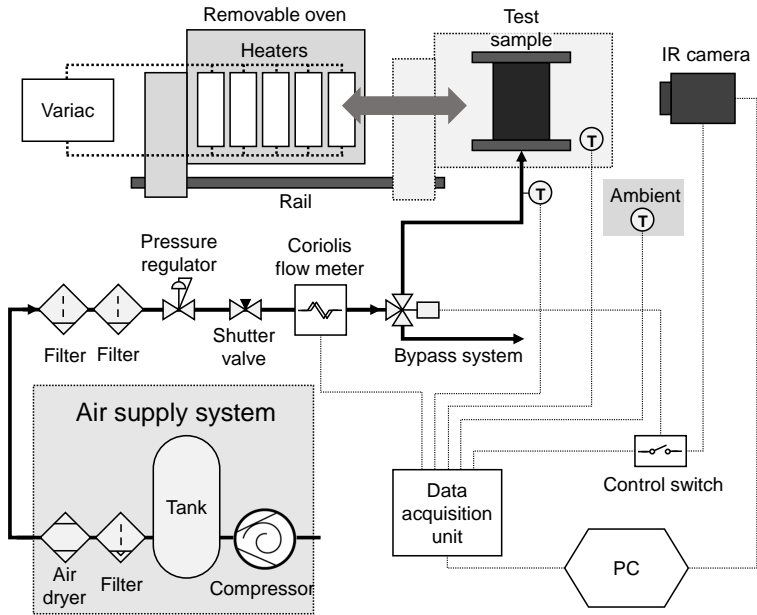


Figure 3.1: A generic layout of the complete test rig

### 3.1.1 Heating system

Heating system is the main part of the test rig and is used for heating the testing geometry to a certain temperature. The heating system consists of oven, variac for power supply and linear guide rail with carriage for oven movement (fig 3.2). The heating phase of our experimental procedure will be performed by this part.

#### 3.1.1.1 Oven

The oven (a drawing of which is shown in the fig 3.3(a)) consists of six parts named as right cover, left cover, heater right, heater left, pivot and handle which are visible from fig 3.3(b). Both cover and heaters parts of each right and left side are combined together creating the right or left

side semicircle of the oven. The main material used in the oven design was carbon steel. The external diameter of the oven is  $400\text{mm}$ , internal diameter is  $350\text{mm}$  while the height is  $203\text{mm}$ . The small circular holes in the right and left cover are used as passage for electric wire connection of ceramic heaters while rectangular shape holes is for fixing the heaters.

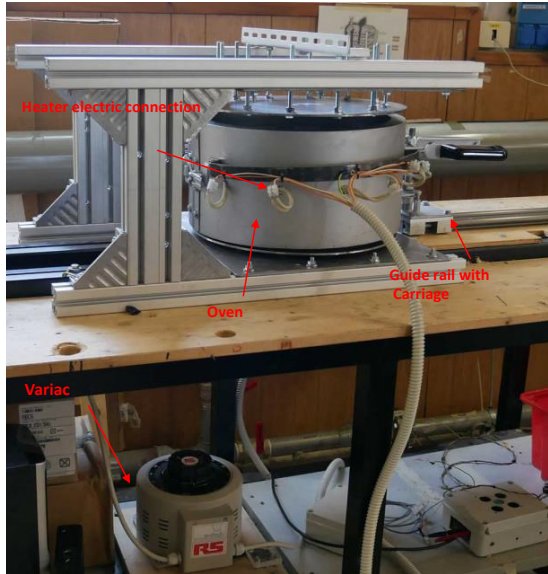


*Figure 3.2: Heating system consisting of oven, variance and guide rail with carriage*

For insulation purpose a stone wool is placed between the cover and heater part of the oven. Stone wool has very low thermal conductivity ( $\lambda$ ) which range from  $0.037$  to  $0.042\text{ W/m}^2\text{K}$ . As we know the lower is the thermal conductivity the better is the insulating property. This is how the heat loss from the oven during the heating phase is decreased. The two semicircles are fixed together at one end with the help of pivot shown in fig 3.3. A handle is attached at that end which can be used to open and close the oven, while a lock is attached to the other end to keep the

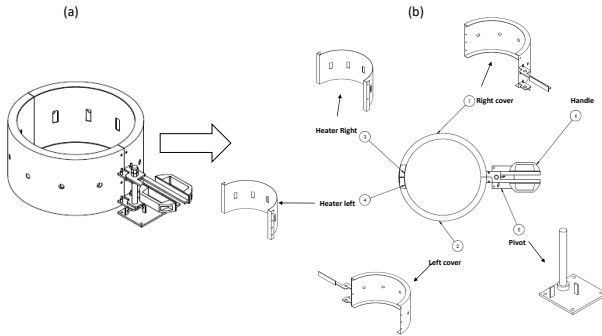


Figure 3.3: (a) oven drawing and (b) top view

oven close while heating (fig 3.4). Ten ceramic heaters will be placed one at each rectangular slots at heater right and heater left part of the oven. The heater are equal spaced so that a uniform heat is produced inside the oven. Each ceramic heater has dimension of  $122 \times 60 \times 35mm$ , power of  $325W$  and can be heated up to  $630C^{\circ}$ . These electric heaters are parallel electrically connected and a variac provides the required power.

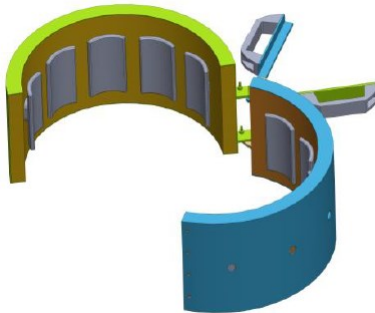


Figure 3.4: oven CAD model showing the ceramic heater fixed to heater part



Figure 3.5: Variac, RS Pro 1-Phase 4.8KVA

### 3.1.1.2 Variac

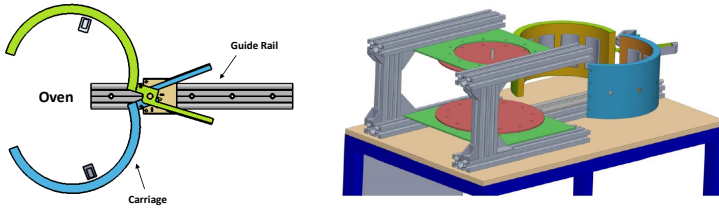
Variac model (fig 3.5) RS Pro 1-phase 4.8KVA, which is a variable transformer, is selected for providing the power to the heaters. It has a primary voltage of 240V with a single output which range from 0 – 240V which can be adjusted manually. The output voltage will be setup according to our desired temperature. While details regarding the specifics are recorded in the table 3.1.

Table 3.1: Specification of Variac RS Pro 1-phase

Specifications	
Dimension	225 × 225 × 190mm
Knob Rotation	Clockwise
Operating frequency range	50Hz to 60Hz
Standard Met	RoHS Complaint
Weight	15.3kg

### 3.1.1.3 Guide rail with carriage

After heating the geometry to a certain temperature then the thermal transient is induced by flowing a coolant inside the geometry. At that instant the heating source must be at zero value or uniform. We consider the zero case by just opening the oven with handle and moving away from the geometry. To obtain the movement the oven is fixed on guide rail with carriage as shown in the figure 3.6.



*Figure 3.6: Opening the oven after heating and moving along the guided rail*

### 3.1.2 Air supply system

A pneumatic system named as air supply system was designed to allow the coolant to flow inside the geometry (for inducing the thermal transient) and to replicate the desired flow condition inside the geometry. A schematic of the air supply system is displayed in fig 3.7. The air is taken from the environment and pressurized by a compressor outside the laboratory which is then directed to the air supply system. Air supply system consists of pressure regulator and a Coriolis flow meter and a 3-way solenoid valve which allows the air to pass through the testing geometry.

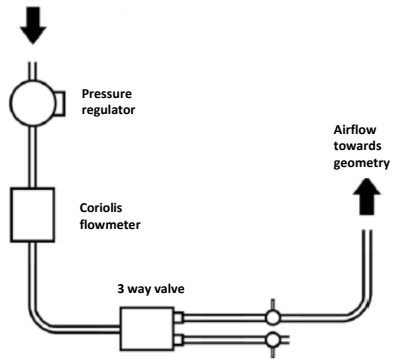


Figure 3.7: Schematic of the air supply system

### 3.1.2.1 Pressure regulator

Pressure regulator is required for adjusting the input pressure of the coolant to a desired pressure. An 20AG-X4G-PH100 Imi Norgren Series high flow pressure regulator was used for this purpose. The range of pressure is from 0.2 to 8 bar as indicated by H in the series code(20AG-X4G-PH100) of the pressure regulator.

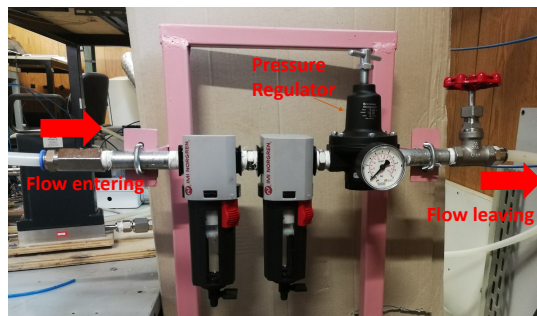


Figure 3.8: Pressure regulator

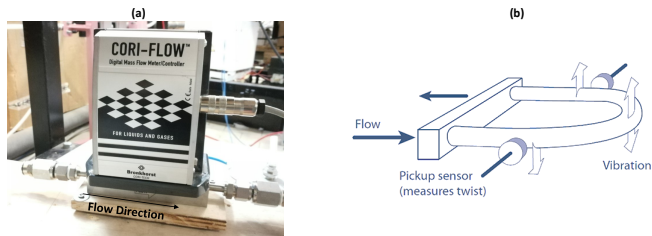


Figure 3.9: (a) *CORI – FLOW<sup>TM</sup>* flow-meter (b) Schematic of a Coriolis flow sensor

### 3.1.2.2 Coriolis flow-meter

In all test cases for each geometry, a fixed coolant mass flow rate is required. To measure the coolant mass flow rate of the coolant a *CORI – FLOW<sup>TM</sup>* by Bronkhorst is selected, which is presented in the fig 3.9(a). The figure 3.9(b) also shows the schematic of a Coriolis flow sensor

Coriolis consists of a tube which is energized by fixed vibration, when a gas is passed through this tube the mass flow momentum change the tube vibration, resulting in phase shifting which can be measured, a linear output is then derived proportional to the flow.

### 3.1.2.3 3-way solenoid valve

In order to avoid sudden mass flow variation at the beginning of the test for the air supply and measurement system, a bypass system is employed: the feeding line is split by means of an actuated 3-way valve, and a branch is connected to the test sample, while the other bypasses air to the laboratory environment. Shutter valves are installed on both branches, and are set so that the total head loss of the bypass line is the same of the one connected to the test sample, including the sample itself. In this way, it is possible to set up the desired flow conditions before the test by flowing air through the bypass line: to make the test



start, the 3-way valve is activated and the air flow is directed towards the test sample, but without any apparent variation for the upstream system. The 3-way valve is connected with a switch which synchronized with the data acquisition system for identifying the start and end of the thermal transient test.

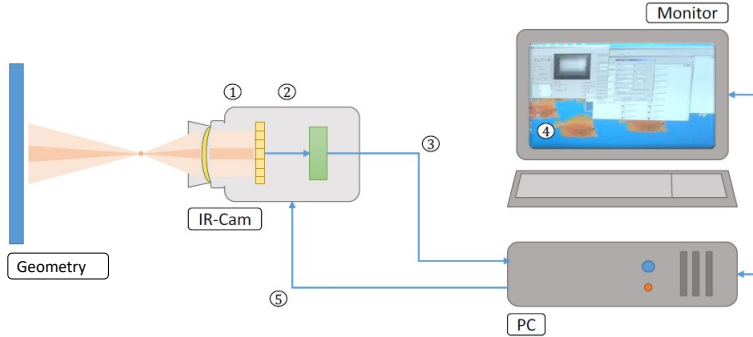


Figure 3.10: Schematic of the thermographic system

### 3.1.3 Data acquisition system

The thermal history of the geometry during the heating phase and thermal transient is recorded with the help of a data acquisition system. Data acquisition system consists of the ThermoVision™ A40M IR camera and thermocouples.

#### 3.1.3.1 ThermoVision™ A40M

The thermographic instrumentation used to conduct the experimental tests consists of a FLIR system ThermoVision™ A40M thermal imaging camera (technical specifications are described in Table 3.2), connected via a FireWire™ cable to a PC equipped with a monitor (fig 3.10). The optical lens is based on germanium and converges the electromagnetic waves towards the sensor (1), an uncooled microbolometer sensor with

Table 3.2: Technical specifications of FLIR system ThermoVisionTM A40M

<b>Image acquisition</b>	
Field of View (FOV)	24° x 18°
Spatial Resolution (IFOV)	1.3mrad
Thermal sensitivity @ 50/60Hz	0.8 °C at 30 °C
Focusing	Multiple; automatic and/or adjustable
Sensor type	Uncooled microbolometer at flat matrix (FPA)
Spectral range	7.5 $\mu m$ to 13 $\mu m$
<b>Measurements</b>	
Temperature ranges (optical filters)	Range 1: -10 °C to +55 °C NOF Range 2: -40 °C to +120 °C NOF Range 3: 0 °C to +500 °C NOF Range 4: +350 °C to +1500 °C AP1
Accuracy (% of readings)	$\pm 2$ °C ( $\pm 2\%$ )
Emissivity setting	User adjustable between 0.1 and 1
Measurement corrections	Reflected environment, distance, humidity relative, external optical properties.

a flat matrix (FPA, Focal Plane Array) of cadmium-mercury-tellurium, sensitive in the spectral band between 7.5  $\mu m$  and 13  $\mu m$  . The signal then passes through the photo-detector (2) which has the function of discretizing it and is then processed by the electronic boards (3) that amplify and convert it, by means of appropriate transducers, into video signals. The FLIR ThermoVisionTM 2.5 system software displays the thermal image (4) and acquires its thermograms. The software also allows the setting of the configuration parameters (5) (focus, optical filter, emissivity value of the observed object and properties of the measurement environment, etc.).

With help of a software interface we can vary the focus of the camera, frame rate of the picture acquisition and duration of the acquisition according

to the requirement and desire. Also other condition for image recovery like emissivity, distance between the lens and geometry, atmospheric temperature and humidity can arranged accordingly.

### 3.1.3.2 Thermocouple

In order to monitor the temperature inside the oven a number of thermocouple are placed there. We use T-type thermocouples all manufactured by Tersed with an accuracy of 0.5 K. These monitor the temperature during both heating phase and thermal transient test. Temperature measurement for the thermocouple is performed by a 20 channel multiplexer module connected to an Agilent HP34970A data acquisition unit. The cold junctions of all channels are located inside a thermally insulated hollow brass cylinder, in order to have a constant and uniform reference temperature for all the junctions, and the temperature compensation is performed thanks to a Pt100 RTD (uncertainty 0.1 K, level of confidence 95%) located inside the cylinder. The unit is connected to the acquisition personal computer by means of a GPIB interface, which allows to control the unit and to record the measured values.

## 3.2 Paint calibration

The geometry is covered with thermal paint to improve the sensitivity which helps IR camera in retrieving the data during the experimental procedure. This is necessary in order to improve the quality of the camera acquisition. The emissivity of the paint is not provided by the manufacturer and so has to be measured. The variation of emissivity with the angle between the surface and the normal to the camera must be evaluated since in the geometry there will be some surfaces which are at a certain angle to the normal of camera. A commercially available black paint is used, which is resistant to temperatures up to 800 °C. As we mentioned before, we need to find the emissivity of the selected black paint. For this purpose a rectangular test bar made of aluminum is used, painted with the black paint for which the emissivity is needed to be measured. The bar length is

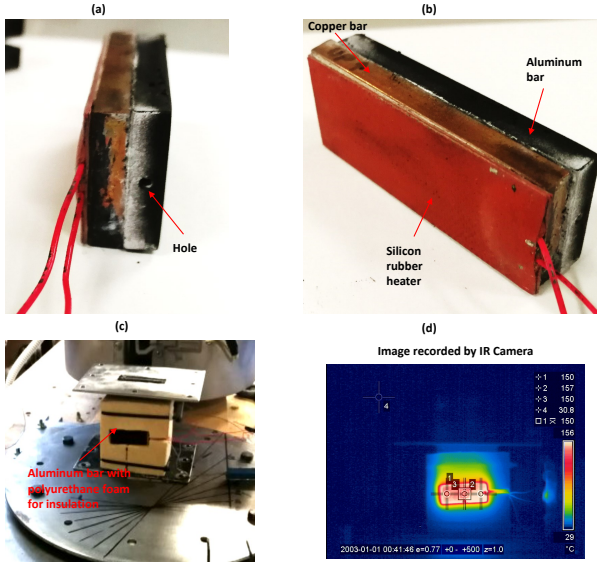


Figure 3.11: Aluminum Bar used for paint calibration

20 mm and the width is 50 mm . A silicon rubber heater is glued to a another copper bar which is then fixed to the aluminum test bar by applying a thermal paste. The copper bar is used to keep the temperature of the aluminum plate as uniform as possible. A hole is manufactured on one side of the painted bar so that the temperature of its center can be measured by inserting a thermocouple, the whole assembly is shown in the fig 3.11(a,b). The bar is thermally insulated on the back and on the sides with polyurethane foam and placed in the front of the camera as shown in the fig 3.11(c). Then we perform number of experiments by heating the bar to certain temperatures which range from 60 °C to 200 °C. As we know that we can change the emissivity value with IR software. Now our aim was to tune the emissivity value in the IR camera software so that the temperature reading of IR camera matched to thermocouple reading inserted inside the bar (fig 3.11(d)). Doing this for all the cases i.e 60 °C, 90 °C, 120 °C,

150 °C, 175 °C and 200 °C we found out that in all majority cases the tuned correct value is 0.77 which will be our desired emissivity value.

### 3.2.1 Emissivity vs angle

Some faces in our geometry will be at certain angles to the normal of IR camera lens. For this reason we try to find what will be the effect of the angle on the emissivity. We setup the test bar at certain angle to the normal of IR camera lens starting from 10° up to 70° with each time an increment of 10°. All the other conditions will be same as section 3.2, the IR camera will record an image for each case some of which are shown in fig 3.12.

During the experiments we listed the values of emissivity, angles, tem-

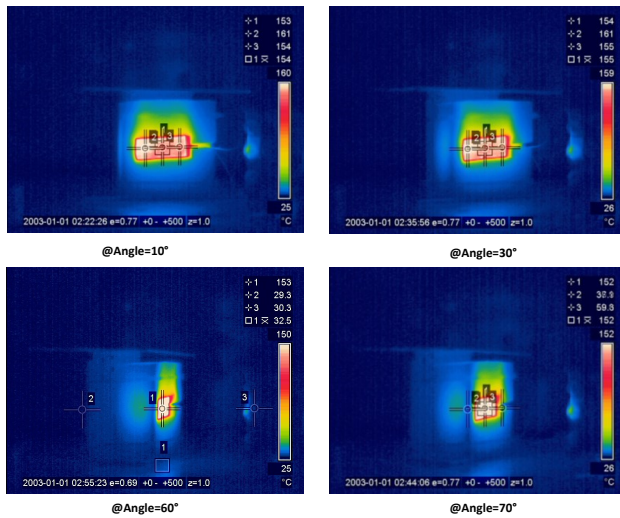


Figure 3.12: Images taken by IR by placing the bar at certain angle to its normal

perature of thermcouple, temperature measured by IR and difference between IR and TC temperature reading in table 3.3. From the table

Table 3.3: *Emissivity vs angle*

Acquisition N [°]	Angle [°]	Temperature(TC) [°C]	Temperature(IR)[°C]	Difference(IR-TC) [°C]	Emissivity [-]
1	0	153.4	153	-0.4	0.77
2	10	153.4	153	-0.4	0.77
3	20	153.5	153	-0.5	v 0.77
4	30	153.6	154	0.4	0.77
5	40	153.7	154	0.3	0.77
6	50	153.9	154	0.1	0.77
7	60	154	153	-1	0.77
8	70	153.2	144	-9.2	0.77
9	80	154.1	142.7	-11.4	0.77
Changing the emissivity value for matching temperature of IR with TC					
10	70	153.2	153	-0.2	0.69
11	80	153.2	153	-0.2	0.6

it is observed that the angle has no effect on emissivity till  $60^\circ$  but as we increase the angle its effect on emissivity becomes more visible, i.e the temperature difference at  $70^\circ$  is -9.2 by keeping the emissivity as  $60^\circ$ . So to make the temperature reading of both IR and TC same ,the emissivity value must be change as shown in the table. At  $70^\circ$  we need a emissivity of 0.69 while at  $80^\circ$  we require 0.60. The value of emissivity at which the temperature between IR and TC is equal or less than -1 is plotted against the angle shown in fig 3.13. The emissivity is 0.77 but as we across  $60^\circ$  the effect of angle starts. From our observations during testing we found out that no surface of any tested geometry is inclined more than  $60^\circ$  to the normal of IR camera.

### 3.3 Mirror selection

During the transient testing we have to record the external surface temperature of a each airfoil side. As we know that airfoil has pressure side, suction side, leading edge and trailing edge, we have to observe all of these during the test.

One way will be to fix an IR camera on each side and record the data. But the problem is the synchronization of these cameras and their availability.

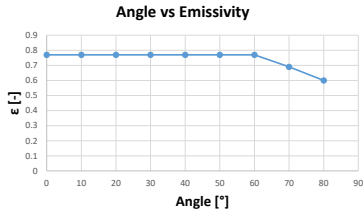


Figure 3.13: Plot of angles vs emissivity

Another way will be to use one camera which is fixed on side while other sides will be viewed through mirrors as shown in fig 3.14 as an example. In the figure the airfoil shown is a blade with U-bend internal channel, the IR camera is fixed on the pressure side while the suction side and leading edge is seen through the mirrors.

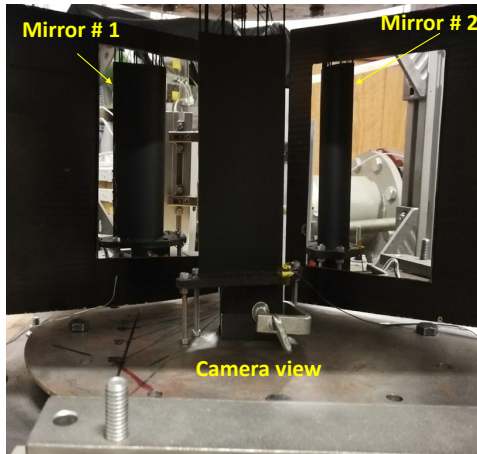
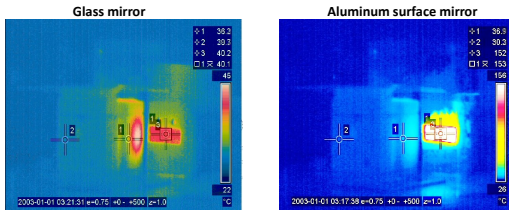


Figure 3.14: Positioning the mirror to observe each side of an airfoil with only one IR camera

**Selection of mirror** There are different types of mirrors available which are used for a number of purpose. We tried two type of mirrors one is commonly used glass mirror and other one an aluminum surface mirror. We use the same test bar by placing it in such angle that its surface can be seen through these mirrors by IR camera. All the procedure will be the same, heating the bar to a certain temperature and then recording the temperature with IR. In this case image of interest will be the one coming through mirror. We did the experiment with common used glass mirror and then with the aluminum surface mirror. The recorded images taken from both mirrors are exhibited in the fig 3.15.

The bar was heated to temperature of  $151\text{ }^{\circ}\text{C}$ , the image taken through



*Figure 3.15: Image taken by IR camera while observing through glass mirror and aluminum surface mirror*

glass mirror showed a reading of around  $40\text{ }^{\circ}\text{C}$  highlighted by point 1 and point 3 which is very lower than the actual temperature, while the image taken through aluminum surface glass shows  $152\text{ }^{\circ}\text{C}$ . So it can be easily proved that the aluminum surface mirror serves our purpose.

We also did some experiments for recording the effect of angle on the emissivity of image coming through the mirror by placing the bar at a certain angle starting from  $10\text{ }^{\circ}$  to  $80\text{ }^{\circ}$  to the normal of the mirror. While fixing the mirror at a certain angle to normal of IR camera. For example the schematic shown in the fig 3.16 tells that the mirror is placed at  $10\text{ }^{\circ}$  to the normal of IR camera while the bar can be place at different angles to the normal of mirror from  $10\text{ }^{\circ}$  to  $80\text{ }^{\circ}$ . We change the angle of mirror to the normal of IR i.e  $20\text{ }^{\circ}$ ,  $30\text{ }^{\circ}$  and  $45\text{ }^{\circ}$ . At each case the bar is rotated



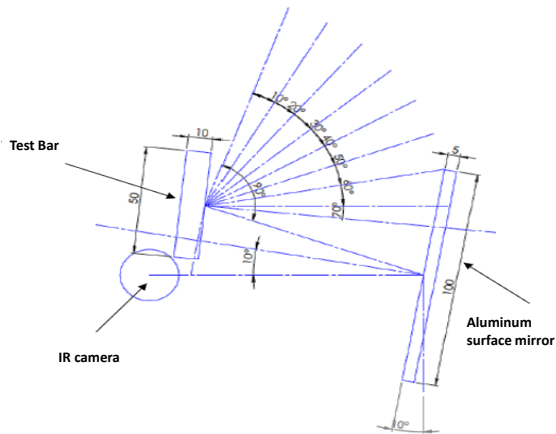


Figure 3.16: Schematic of mirror placed at certain angle while test bar is rotated from  $10^\circ$  to  $80^\circ$  degree

starting from  $10^\circ$  to  $80^\circ$ . The effect of angle on the emissivity is recorded which is demonstrated by table 3.4. The observation is the same as the previous case i.e. the angle doesn't effect the emissivity till  $60^\circ$ .

### 3.4 Test procedure

Steps of our test procedure

1. Setting up the test rig.
2. Checking the data acquisition system.
3. Closing the oven and start heating the test article.
4. After achieving the desire temperature the oven is removed.
5. Mirrors are positioned at the required place.
6. Turning on the data acquisition.

Table 3.4: *Emissivity vs angle for mirror*

Acquisition N [°]	Test bar angle [°]	Temperature(TC) [°C]	Temperature(IR)[°C]	Difference(IR-TC) [°C]	Emissivity [-]
Placing the mirror at 10 [°] to normal of IR camera					
1	0	151	152	1	0.77
2	30	151.1	151	-0.1	0.77
3	60	150.2	151	0.8	0.77
4	70	150.9	151	0.1	0.66
Placing the mirror at 20 [°] to normal of IR camera					
5	0	152.3	152	-0.3	0.77
6	30	152	152	0	0.77
7	60	151.9	152	0.1	0.77
8	70	153	152	-1	0.68
Placing the mirror at 30 [°] to normal of IR camera					
9	0	152.2	152	-0.2	0.77
10	30	152.3	153	0.7	0.77
11	60	152.1	153	0.9	0.77
12	70	152.2	152	-0.2	0.67
Placing the mirror at 45 [°] to normal of IR camera					
13	0	152.1	152	-0.1	0.77
14	30	152.3	152	-0.3	0.77
15	60	152.2	152	-0.2	0.77
16	70	151.5	152.1	0.6	0.65

7. Starting flowing the coolant to induce the thermal transient by a switch which is synchronized with data acquisition so that the start of the test is known.
8. Data acquisition system will record the data for fixed duration.
9. Post-processing of recorded data which will then be used as initial boundary condition for our FEM model like initial temperature or for comparison with FEM output (final temperature at the end of transient test).

Data obtained with thermocouples is visualized with a help of a custom LabVIEW program. The program automatically writes the recorded data into text file which can be used for further processing. Figure 3.17 shows the reading of the two thermocouples one of which is inserted at the inlet

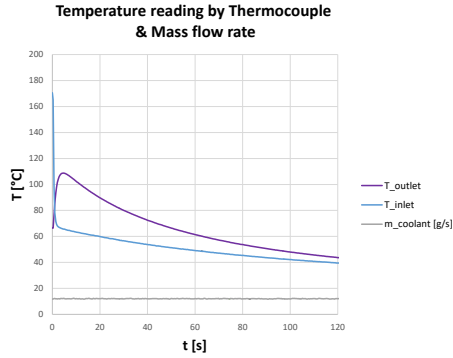


Figure 3.17: Thermocouple reading and mass flow rate during the Transient test

while the other one at the outlet of the U-band internal channel blade (Chapter 4). The figure also shows the mass flow rate during the test measured by the Coriolis flow meter. The data obtained with IR camera is in the video format from which the frames will be extracted with the help of a custom design Matlab macro. The fig 3.18 presents an image which is extracted from the video of the transient test of the blade with U-bend internal channel. It shows the temperature distribution of the external surface of the blade leading edge, pressure side and suction side.

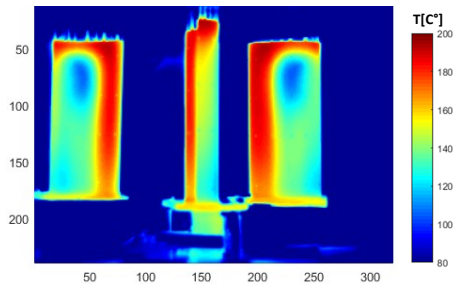
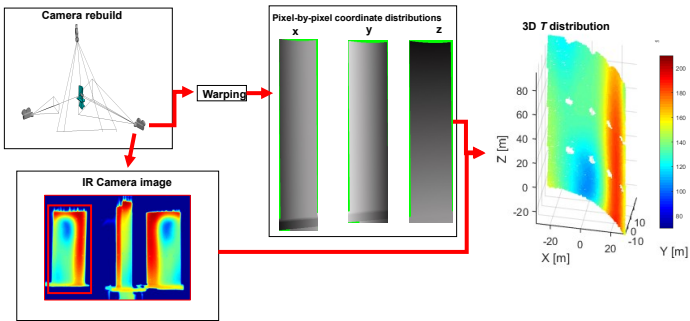


Figure 3.18: sample extracted from the IR data for a blade

### 3.5 Data postprocessing

The data obtained from the data acquisition system consists of IR videos and text files both in raw form. These contain time resolved external surface temperature, coolant temperature and mass flow rate values. One thing which must be noted from the image shown in fig 3.18 is that it is a 2D image. Now in order to use this image as initial boundary condition for FEM or for comparison of this with final FEM output it will be necessary to convert this into a 3D image. The reason behind this is that initial boundary condition and final output external surface temperature of FEM are 3D. This is performed with Matlab and the explored procedure will be explained in details below.

**3D mapping** The video obtained with IR is exported as series of frames. The frames which were recorded before the transient test can be removed thanks to switch synchronization discussed in detail before. These are in 2D format as shown in the fig 3.18.



*Figure 3.19: 3D mapping procedure for PS side of a blade*

A custom designed 3D mapping procedure as shown in fig 3.19 was developed to convert the 2D data into 3D data. First step of the procedure is to build location and viewing range of the IR camera in the test article CAD space. As there is no mirror option in the CAD space we just replace

each of the mirror view with a camera. The location and viewing range of these two cameras in the CAD space are such that the images captured by these must match with the one's obtained with two mirrors. Then in this CAD space the external surfaces of the test article are colored with linear grey scales according to the variables which needed to be mapped. In this case we have three variable i.e the coordinates  $x$ ,  $y$  and  $z$ , so three grey scale images corresponding to each variable will be obtained for each camera.

For having more accurate concordance between these grey scale images and the temperature images obtained with IR: some marker points are identified both on the actual geometry and on it's CAD model. These points on actual geometry surface are not painted, to differentiate them from the remaining of the geometry surface. By keeping correspondence between the marker points of both grey scale images and 2D temperature images, the grey scale images are warped. In this way a more accurate pixel by pixel correspondence of both grey scale and 2D temperature images is performed.

Then on the warped grey scale image the locations of two points are identified which helps to associate the coordinate values of such points with the grey intensity on the corresponding image. Linear interpolation of the grey intensity allows us to transform the grey scale images in coordinate distributions. By querying the points of the coordinate distributions having the same indices it is possible to know the spatial coordinates of any pixel in the temperature map. As visible from grey scale images in the fig 3.19 the area outside the test article surface is colored with green which helps in identifying the points which fall outside of the geometry. In this case the grey scale images are obtained with Solidworks while the whole processing is run with Matlab script. This procedure is applied for pressure side , suction side and leading edge separately then the three output are combined to get full 3D temperature distribution. The fig 3.19 shows this 3D mapping procedure and its final 3D temperature distribution output for pressure side only, but this must also be done for suction side and leading edge separately which gives a

3D outputs (fig 3.20) then the three outputs are finally combined to get a full 3D temperature distribution.

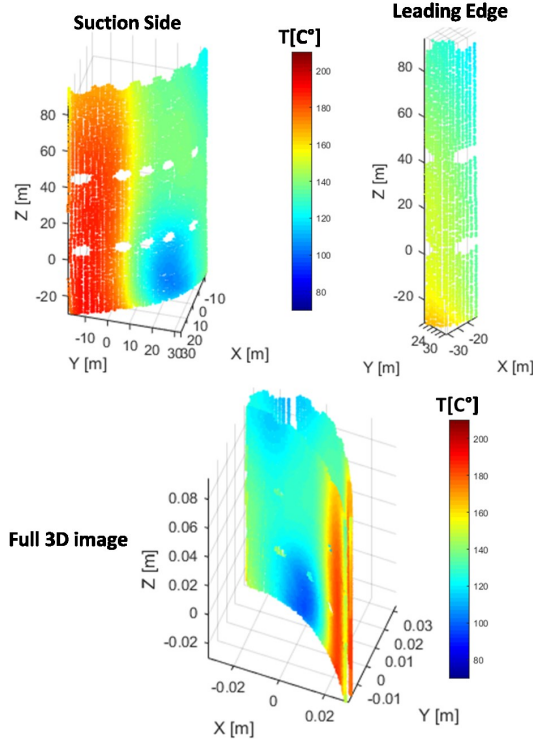


Figure 3.20: Full 3D temperature distribution of a blade

In this way the whole transient test recorded 2D data is converted into 3D. Now to implement the FEM we have all the necessary initial boundary conditions like initial 3D temperature distribution of the blade transient test, initial HTC distribution obtained from LTCM and coolant temperature. After running the FEM its output 3D external surface temperature will be compared to the final 3D temperature obtained with mapping procedure discussed above.

## Chapter 4

# Preliminary Test Cases

In this chapter we will discuss about the development of the proposed methodology which was presented before by implementing it on preliminary test cases. Two cases are selected, one is the baseline geometry a circular duct while the second is a blade with U-bend internal channel. The results obtained for each case will be discussed in detail. A comparison with available literature data will also be presented, revealing a good agreement between results and the predicted values.

### 4.1 Circular duct

A smooth circular duct made of stainless steel (thermal conductivity of  $16 \frac{W}{mK}$ ) is chosen as baseline geometry. The duct geometric features consists of inner diameter of 10 mm, external diameter of 12 mm and total length of 1000 mm (fig 4.1). A Reynolds range from 10,000 to 80,000 can be achieved with this.

There are two reasons for starting with this geometry, one is its simplicity and easiness and second one is the wide availability of reliable expected results for this including many correlations. It is clearly observed from the fig 4.1 that duct is axisymmetric, which means by considering 1D temperature history along one axis may be the representative of the whole geometry, so fully 3D mapping of the data is not needed. Also the

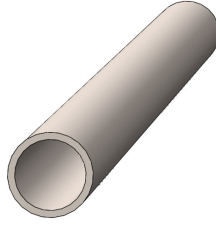


*Figure 4.1: Smooth circular duct*

interaction of the fluid model ( which will calculate the fluid temperature during thermal transient) with FEM can be easily implemented. As already mentioned our methodology consists of two parts: one is the experimental and the other is the FEM. For experimental part the test rig which is presented in chapter 3 will be explored. A schematic of the arrangement of this duct inside the test rig and positioning of data acquisition is shown in the fig 4.2. There is a number of thermocouples placed inside the test rig, some of these will be used during heating phase while some in the thermal transient phase.  $T_{surface}$ ,  $T_{lx}$ ,  $T_{rx}$ ,  $T_{top}$  and  $T_{bottom}$  are the thermocouples which will monitor the temperature during the heating phase while  $T_{int}$  and  $T_{out}$  are inserted inside the duct inlet and outlet and will measure the temperature of the coolant during the thermal transient. The reading of these thermocouples will be sent to the PC with help of multiplexer. The first step of the experimental part is to heat the geometry to a known temperature, then coolant of known temperature is passed through the geometry to induce the thermal transient. During this thermal transient the external surface temperature is measured with IR. To obtain more reliable result the external surface of the geometry is painted black . The duct portion which is positioned inside the oven is painted as shown in the fig 4.3. The paint whose emissivity is measured as sample in the previous chapter 3 will be used for this purpose. The overall length of the duct was selected so that fully developed flow is obtained in the measured section , which is the one already enclosed in



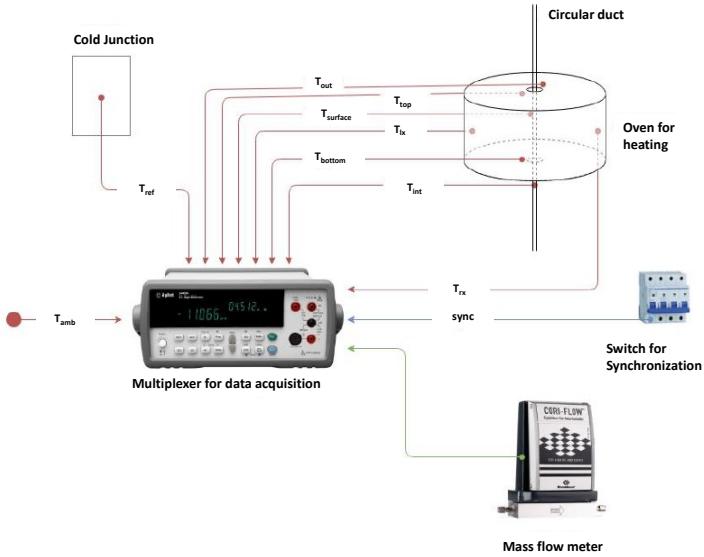


Figure 4.2: Schematic of circular duct arrangement within test rig

the oven. In this case the oven can house only 235 mm of the duct length.

To choose the cooling air flow rate, it was decided to use values compatible with those used in real cases of cooling gas turbines blades. Test conditions were defined coherently with the laboratory facilities and defined by our Reynolds number express as:

$$Re = \frac{\rho u L}{\mu} = \frac{u L}{\nu} \quad (4.1)$$

where  $u$  is the speed of free current, taken out of the boundary layer, measured ( $m/s$ ),  $L$  is still the characteristic length,  $\nu$  is the kinematic viscosity of the fluid ( $m^2/s$ ),  $\rho$  is the density of the fluid ( $kg/m^3$ ) and  $\mu$  is the dynamic viscosity of the fluid ( $kg/ms$ ).

In the tests carried out for this work, it was decided to use three values for the  $Re$  number, equal to 25000, 50000 and 75000. These values

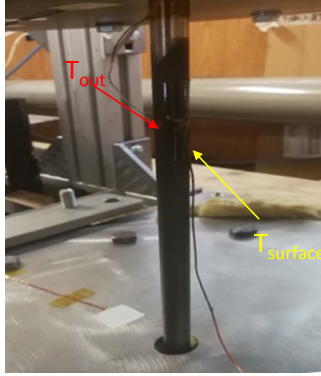


Figure 4.3: Placement of the black painted duct inside the oven

are compatible with the typical values found in turbine cooling systems. Also in this way we ensured that the motion was turbulent and that physical quantities ( mass flow rate) could be measured by the explored instruments. Mass flow rate to be employed in each test is derived from the corresponding Re number. The following table 4.1 represents the mass flow rate for each of these three test cases.

Table 4.1: Test Matrix for circular duct

Re [-]	Mass flow rate [g/s]
25,000	3.62
50,000	7.25
75,000	10.87

#### 4.1.1 Re 50,000

In order to illustrate the employed procedure and the obtained results the test with  $Re = 50,000$  was considered first. Before heating phase the desired mass flow rate  $7.25 \text{ g/s}$  ( $Re 50,000$ ) is setup with help of

air supply system. Then the heating phase starts, during which the temperature inside the oven and of duct surface is monitored continuously with the help of thermocouples. The heating phase will progress till the duct surface temperature reaches fixed temperature, which is  $220\text{ }^{\circ}\text{C}$  in this case. Although we can achieve more temperature with our test rig

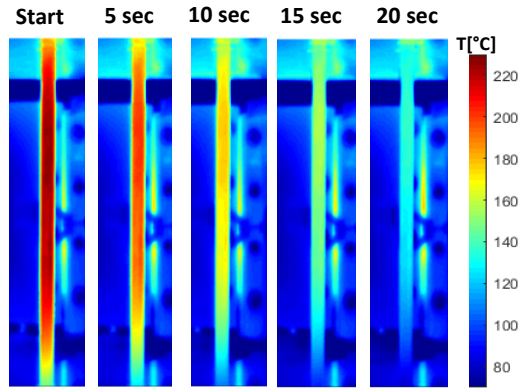


*Figure 4.4: Duct surface temperature evolution during the thermal transient*

facility but for safety reasons we don't go behind this value. Then the oven will be removed and coolant with mass flow rate is introduced inside the duct, which will induce a thermal transient during which external surface temperature of the duct is recorded by the IR camera. As we already mentioned, circular duct is axisymmetric so we don't need to measure the whole surface temperature, just along one axis which will be representative of the whole geometry. This is achieved with help of IR camera, we will not need mirrors for the coverage of the whole duct surface. The temperature at inlet and outlet of the duct will be measured with thermocouple during transient. Duct surface temperature at different instants during the transient is shown in the fig 4.4. It can be easily observed that the temperature decreases along the transient. The reading of the thermocouple insert at inlet and outlet of duct is demonstrated

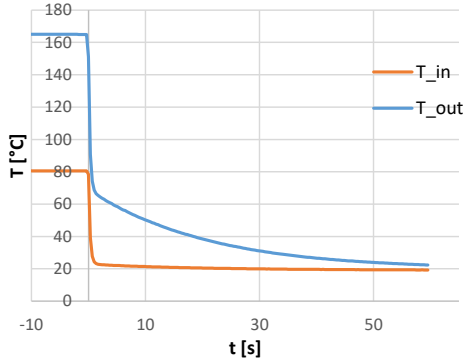


Figure 4.5: Thermocouple reading at inlet and outlet of duct during thermal transient

in the fig 4.5. Zero in the abscissa represents the start of the thermal transient. The inlet temperature is presented by  $T_{in}$  while outlet by  $T_{out}$ . Both reading shows that the temperature decreases gradually during thermal transient, especially the temperature at the outlet. First few seconds of data is omitted from the final data of the test, since these seconds are required to allow the flow conditions to stabilize to a steady state. The obtained data will be post processed to use it in our next step of the procedure which is FEM of the duct.

Thermal FEM model of the circular duct will be solved with Ansys® 18.0. Due to the duct axisymmetrical nature the FEM can be run on just a  $1^\circ$  section of duct, which will help us in minimizing computing time. The FEM model of this  $1^\circ$  section of duct consists of  $1.763 \times 10^5$  nodes and  $2.35 \times 10^4$  elements. Now the boundary conditions which will be required are initial temperature, coolant temperature, duct material properties, internal HTC distributions, external convection (value of  $9 \frac{W}{m^2K}$  obtained with correlation for natural convection [54]) and radiation. As stated in chapter 2.1.1 we will use LTCM approach to find the initial HTC, while

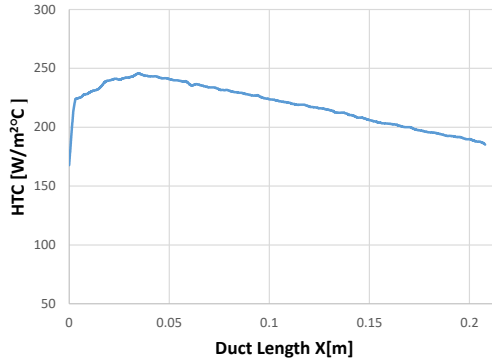


Figure 4.6: Initial LTCM HTC along the duct X-axis

initial temperature will be obtained from the experimental data. The coolant temperature during the transient will be measured with the help of fluid model based on a simple energy balance, as discussed in chapter 2.1.2. Initial obtained LTCM HTC is shown in the fig 4.6, the value is just along X-axis of the duct only (axisymmetrical nature). As seen from the figure the HTC decreases as we move to the outlet of the duct, the reason could be that the LTCM approach doesn't consider spatial variation of the flow temperature but only time by time temperature variation. Figure 4.7 presents the obtained duct initial external surface temperature. The total thermal transient duration of the FEM will be the same as the experimental one, which is 30 second in this case. The total duration is divided into 5 second sub time step. For each time step the boundary conditions will be updated continuously like coolant temperature (which will be provided by fluid model) and initial temperature.

At the end of thermal transient the FEM output external surface temperature ( $T_{FEM}$ ) will be compared with the experimental one ( $T_{Exp}$ ). If both match then LTCM HTC is our final internal HTC, otherwise we have to iterate next HTC value with secant method (chapter ??) until the convergence is achieved between both of them.

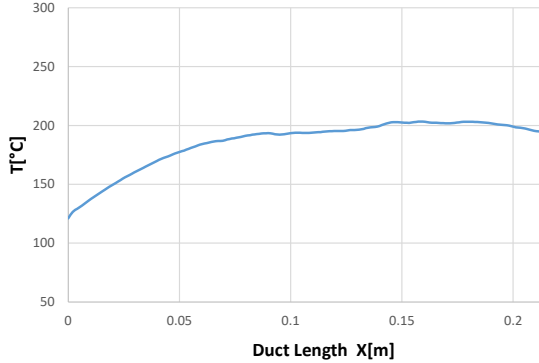


Figure 4.7: Initial temperature along the duct X-axis

The fig 4.8 shows each iterated HTC value and the corresponding temperature difference between FEM and experiment. We fixed a convergence criteria which states that the root mean square value of the temperature difference must be less than 0.5. After the fourth iteration we reach the desired convergence criteria. HTC value with number shows the sequence of iteration i.e HTC[1] means the first iteration. Same as for the temperature difference: TD[1] is the corresponding temperature at first iteration. As observed the temperature difference decreases with each iteration, going close to our convergence criteria. HTC[3] is our final HTC value where the root mean square value of TD[3] is less than 0.5. The final HTC value closely follows a horizontal trend as compared to LTCM HTC, except at inlet and outlet of the tube where the HTC value falls because of boundary effects. As a consequence for further comparisons the points near the inlet and outlet of the duct will be not considered.

**Comparison with literature data** As at the start we highlighted the reason of selection of circular duct as baseline geometry i.e. the availability of reliable literature data for comparison. In order to validate the measurement technique we compare our results to Petukhov equation

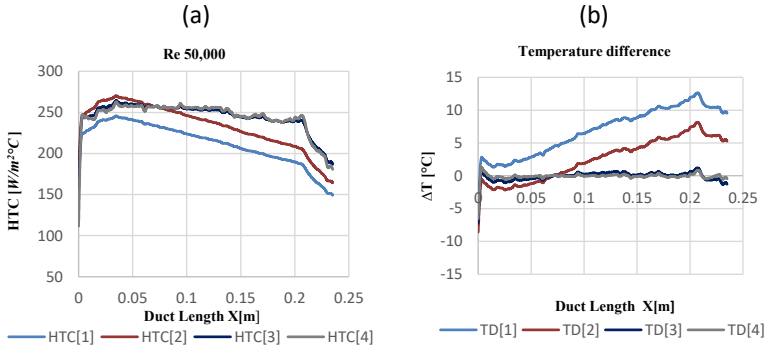


Figure 4.8: (a) HTC iteration (b) Temperature difference at each iteration

[55] which is provided below:

$$Nu = \frac{\frac{f}{8} Re Pr}{1.07 + 12.7(\frac{f}{8})^{0.5}(Pr^{\frac{2}{3}} - 1)} \quad (4.2)$$

Where  $f$  is the friction factor,  $Pr$  is the Prandtl Number and  $Nu$  is the Nusselt number. Colebrook equation [56] was employed to find the friction factor. The value of  $HTC[Corr]$  reported in the charts is directly derived from  $Nu$  using its definition ( $h = \frac{NuK}{D}$ ), where  $K$  represents the thermal conductivity and  $D$  is the internal diameter of the duct. The average value of the measured final HTC along the duct axis is  $250.34 \frac{W}{m^2K}$  which is around 3 % lower than the correlation value ( $258 \frac{W}{m^2K}$ ). This is illustrated in the fig 4.9, which compares this experimental value against correlation and LTCM HTC. The HTC value slightly decreases as we move from the inlet to outlet especially at lower 1/3 duct portion near the outlet as compared to the remaining duct. Which may be because of inaccuracy of the fluid model in this region and a small reflection (which is not modeled) coming from nearest oven wall.

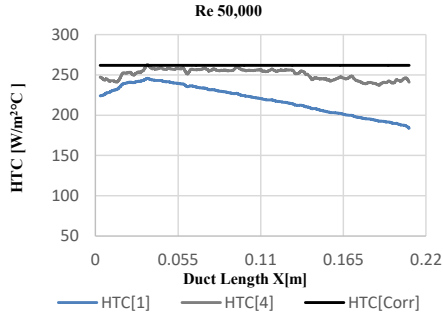


Figure 4.9: Final HTC comparison with correlation for Re 50,000

#### 4.1.2 Re 75,000

After finding reliable results in first case we move to our second test case which is Re 75,000. The corresponding mass flow rate (10.87 g/s) will be provided with the help of air supply system. Heat transfer phenomenon increases with the increase of mass flow rate so the transient test duration must also decrease to have more reliable results. As higher mass flow rate is required in this case which is higher than the previous case, so the transient duration must be decreased to 15 second. Some initial second

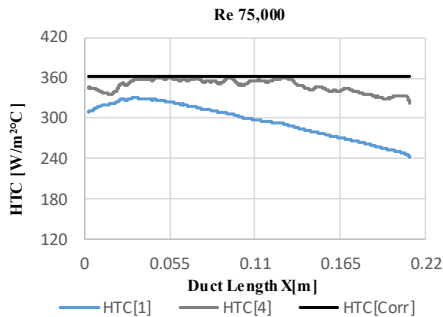


Figure 4.10: HTC comparison with correlation for Re 75,000



obtained data will be not included as like in the previous case. The final HTC obtained for Re 75,000 is shown in fig 4.10, where it is also compared with correlation and LTCM HTC. The average value in the case of Re 75,000 is  $343.63 \frac{W}{m^2.K}$  which is around 3% lower than the correlation value ( $352.4 \frac{W}{m^2.K}$ ). The overall shape of the final HTC curve is same as the previous.

### 4.1.3 Re 25,000

In the previous case we selected a higher Re value, now a lower value is chosen for conducting the test. The thermal transient duration considered in the case is 50 second because of the lower mass flow rate(3.626 g/s). Our final HTC average value in this case (fig 4.11) is  $156.8 \frac{W}{m^2.K}$  which is around 2% lower than the correlation which is  $159 \frac{W}{m^2.K}$ .

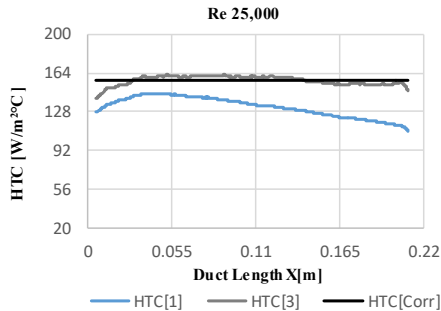


Figure 4.11: HTC comparison with correlation for Re 25,000

### 4.1.4 Nu vs Re

To justify the accuracy and robustness of our results, a comparison between  $Nu$  and  $Re$  is shown in fig 4.12.  $Nu$  is calculated from the average value of HTC along the duct for both LCTM and FEM final results. As clearly shown, the measured  $Nu$  always falls within 3 to 4% of the correlation for each Re. It can also be noticed that our calculated

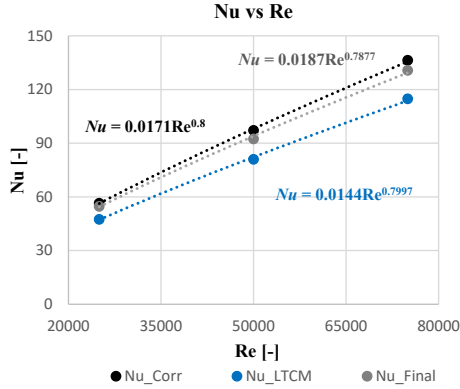


Figure 4.12:  $Nu$  vs  $Re$

$Nu$  values ( $Nu\_Final$ ) are directly proportional to  $Re^{0.7877}$  and closer to the correlation trend:  $Nu \propto Re^{0.8}$  ( $Nu\_Corr$ ), which further proves its robustness.  $Nu\_LTCM$  represents the value obtained with LTCM approach, these values are very far from the correlation as compared to our obtained results

#### 4.1.5 Uncertainty analysis

To analyse the accuracy of the proposed methodology, an uncertainty analysis is performed according to the standard ANSI/ASME PTC 19.1 [57], based upon on the Kline and McClintock method [58]. The uncertainty linked with IR camera temperature reading is  $\pm 2^\circ C$ , with thermocouples is  $\pm 0.6^\circ C$  while uncertainty of Coriolis is  $\pm (0.028 + 0.5\%$  of the reading)  $g/s$ . Uncertainties associated with the material properties of duct are  $\pm 5\%$  for specific heat capacity,  $\pm 2\%$  for density and  $\pm 5\%$  for thermal conductivity respectively. The total uncertainty on calculated heat transfer coefficient is found to be up to 5% by taking into account all the parameters uncertainties which are discussed above.

Finally it can be concluded that the proposed methodology provides very

reliable result for this geometry (circular duct). This was the first phase of our procedure development, next we will move to implement this on a blade with U-bend channel. Which is possible with little improvement like getting experimental full 3D external surface temperature history of the blade during the thermal transient test.

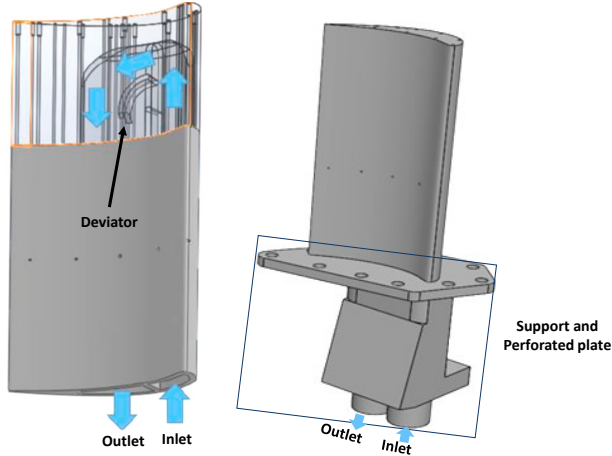


Figure 4.13: Blade with U-bend internal channel(left) and with extruded part(right)

## 4.2 Blade with U-bend internal channel

After implementation of our proposed methodology on baseline geometry and finding satisfactory results we move to a more complex geometry, a blade with U-bend internal channel. This is a prismatic blade 3D model printed in inconel. The blade profile has been built by extruding the midspan profile of a first stage rotor blade with a reduction scale factor of 1.5. This is shown in fig 4.13, having a internal U-bend smooth channel for cooling. The cooling flow is fed from the hub of the blade, as sketched in fig 4.13(left), where the top part of the blade is reported in transparency

in order to have a clear view of the coolant path in correspondence of the bend and also to see the presence of deviator. The blade is also provided with an extruded part as shown in fig 4.13 (right). This consists of perforated plate which helps to fixed it inside the test rig. Also it has inlet and outlet connection for air supply system.

As compared to circular duct, this geometry is not axisymmetrical, as a consequence just considering temperature history along one axis will be not representative of the whole geometry, so we will need a full view of blade surface during the thermal transient test. This can be achieved with the help of aluminum surface mirrors, details about this mirrors and its effect on emissivity are well explained in the chapter 3.3. After obtaining the 2D image with IR using theses mirrors it is converted into full 3D image with help of 3D mapping procedure demonstrated in the chapter 3.5. Two thermocouples are inserted at the inlet and outlet of the channel to measure the temperature of the coolant during thermal transient. The placement of the blade inside the test rig and positioning of the mirrors during the thermal transient can be seen from the fig 4.14. The blade is fixed with the help of the perforated part which is visible from the figure. Air supply system is also connected to the inlet and outlet connections which are shown in fig 4.13.

Fluid model approach which was used in the circular duct case is also followed here with some assumptions regarding the internal channel. one of which is that we considered the internal U-bend channel as a smooth circular duct: a equal amount of air mass flow rate will pass through each section of the duct. After implementing the FEM procedure with this fluid model approach we find out that our final results are converging but little far away from the literature data. The reason is that the U-bend internal channel is considered as smooth circular duct which is inaccurate assumption as visible form the CAD of the blade 4.13. The circumference of the channel changes as we moves from inlet to outlet. The mass flow rate at each section along the channel will be also not same, because of this model provide inaccurate value of coolant temperature.

To overcome the issue we considered some modification to this fluid model

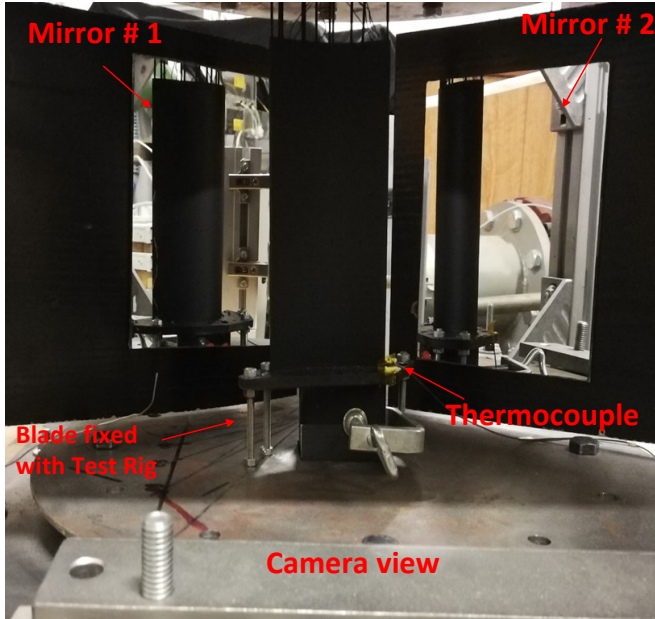


Figure 4.14: Blade positioning inside the test rig with mirrors in place

approach. As we already stated that we insert a thermocouple at outlet which continuously measured the temperature during the thermal transient. Now using this thermocouple reading as a target the fluid model find a dimensionless temperature coefficient  $\sigma T$  given by equation 4.3 and shown in fig 4.15 (left) which counters the variation of the fluid inside the U-bend internal channel. The dimensionless temperature coefficient  $\sigma T$  value starts from zero at the inlet to 1 at the outlet of the channel. Using this coefficient we find the  $T_{air}$  along the internal channel using following equation 4.4:

$$\sigma T = \frac{T_s - T_{inlet}}{T_{outlet} - T_{inlet}} \quad (4.3)$$

$$T_{air} = T_{inlet} + \sigma T(DT) \quad (4.4)$$

where  $DT = (T_{inlet} - T_{outlet})$

$T_s$  is the temperature calculated by the fluid model at a certain location in the channel,  $T_{inlet}$  represent the thermocouple temperature reading place at inlet of the channel, and  $T_{outlet}$  is the thermocouple temperature reading insert at the outlet of the channel. Coolant temperature distribution along the channel at a time step during the transient which is find by this approach is shown in the fig 4.15 (right).

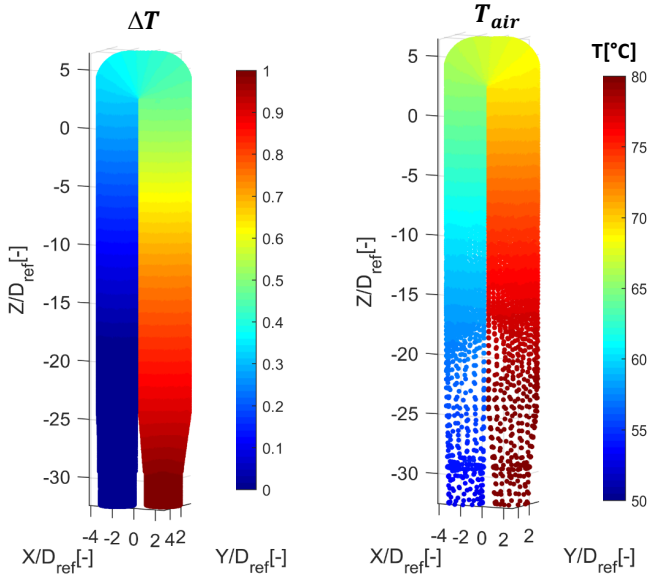


Figure 4.15: Dimensionless temperature coefficient (left) and coolant temperature inside the channel (right)

Different test cases are considered with each having a different  $Re$  number i.e.  $Re = 41220$  ,  $Re = 32026$  ,  $Re = 20375$  and  $Re = 10106$  . For achieving these  $Re$  number different mass flow rate is considered for each test case. We performed all the tests starting from the highest to lowest  $Re$  number, in the following sections first we will discussed  $Re = 41220$  test case and then the remaining test cases.

### 4.2.1 $Re = 41220$ case

The mass flow rate of the coolant will be derived from the  $Re$  number. Due to higher  $Re$  number in this case, the heat transfer phenomenon will be larger which means we will require a shorter thermal transient test duration. After heating the blade to temperature of  $220\text{ }^{\circ}C$  inside the oven, a coolant of fixed mass flow rate is initiated inside the U-bend channel of blade with the help of air supply system. This will start a thermal transient during which the external surface temperature of the blade is recording with IR. The image recorded by IR and the inlet and outlet thermocouple reading are shown in the fig 4.16. The image recorded by IR and the inlet and outlet thermocouple reading are shown in the fig 4.16. The obtained 2D (fig 4.16 a) is post processed with 3D mapping procedure which converts it into a 3D distribution. The temperature at inlet and outlet will be used by the fluid model for predicating the coolant temperature inside the channel (fig 4.16 b).

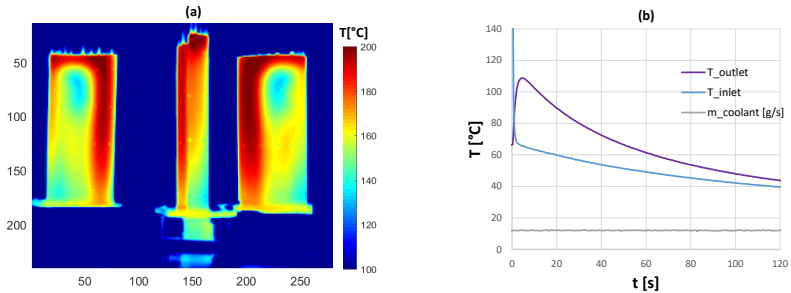


Figure 4.16: (a) IR 2D image of the blade during transient (b) Thermocouple reading at inlet and outlet of the blade

The results obtained with experimental part will be used as boundary conditions for FEM of the blade. The first boundary condition is the initial temperature of the blade which is presented in the fig 4.17(a), where each axis is divided by  $D_{ref}$ : the diameter of the LE channel internal duct. As visible there are some small holes in the temperature map, where there is no temperature reading. These holes are the marker points about

which we already discussed in the Chapter 3.5. These missing temperature values can be easily interpolated from the surrounding available values. The initial internal channel heat transfer coefficient for internal convection obtained with LTCM approach is shown in the fig 4.17(b). The left side of the internal channel close to leading edge is named as LE channel side while the one close to the trailing edge is the TE channel side. To make the data dimensionless the HTC value is divided by  $h_{LEavg}$  which is the average HTC value on LE channel side.

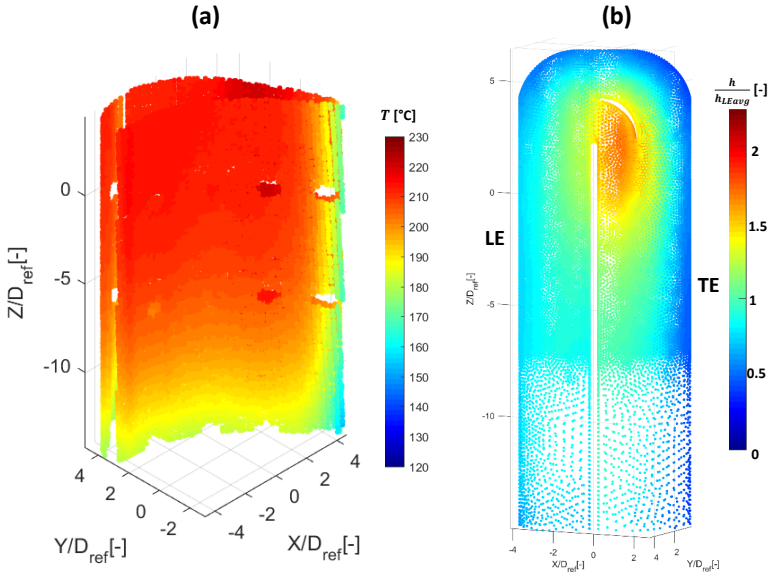


Figure 4.17: (a) External surface temperature of the blade at start of the transient (b) Initial convective internal LTCM HTC

After getting all of the boundary conditions FEM of the blade is run for same transient duration (which is 30 sec for  $Re = 41220$  case) as the experimental one. The FEM model consists in about  $2.179 \times 10^5$  solid87 elements (ten nodes tetrahedrons elements) and includes every details of



the internal cooling channel such as the deviator in the internal channel. The grid of the airfoil is properly refined to characterize each detail without significantly affecting the computational time (fig 4.18). Same procedure will be followed for the iteration as previous case, the circular duct. The temperature difference is interpolated to internal channel for iterating the HTC, iteration will continue until we reach our convergence criteria. In this test we achieve our final internal channel HTC value after fifth iteration, which is demonstrated in the fig 4.19. This is also compared to the initial HTC obtained with LTCM approach.

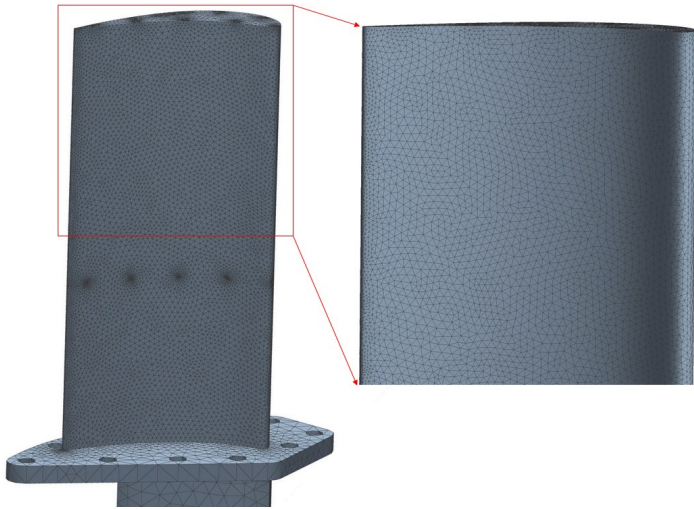


Figure 4.18: Thermal grid details

The obtained results allow us to observe the heat transfer pattern and magnitude associated with the different features of the internal cooling channel. Now talking about Final HTC, starting from the LE channel (left side channel) the HTC value is not so uniform at start of the channel but as move further the value become more uniform which may be because of the flow, fully developed in this region. As we getting closer to the C

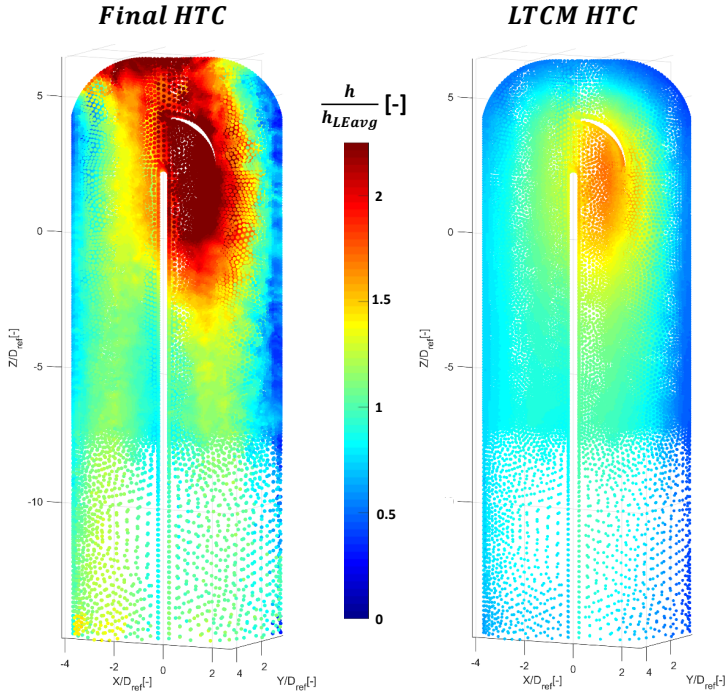


Figure 4.19: Comparison of the final obtained internal HTC vs LTCM HTC

bend area the value starts increasing which is more visible in this case (as compare to LTCM HTC). The value at the tip of the blade increase where the flow impinged which may be attributed to this increase. Due to the presence of the deviator the flow accelerates in surrounding region which could possibly increase the HTC. The HTC values at TE channel decreases as move from the left side to right side of the channel. The possible reason of this is that the TE channel is thinner at the right side as compared to its left side, which means lesser coolant flow so lesser HTC values.

These all internal cooling channel features are more prominent in the case

of Final HTC value as compared to LTCM HTC. The reason is that the Final HTC is obtained with FEM analysis of this blade which considers all the possible phenomenon which will effects its heat transfer.

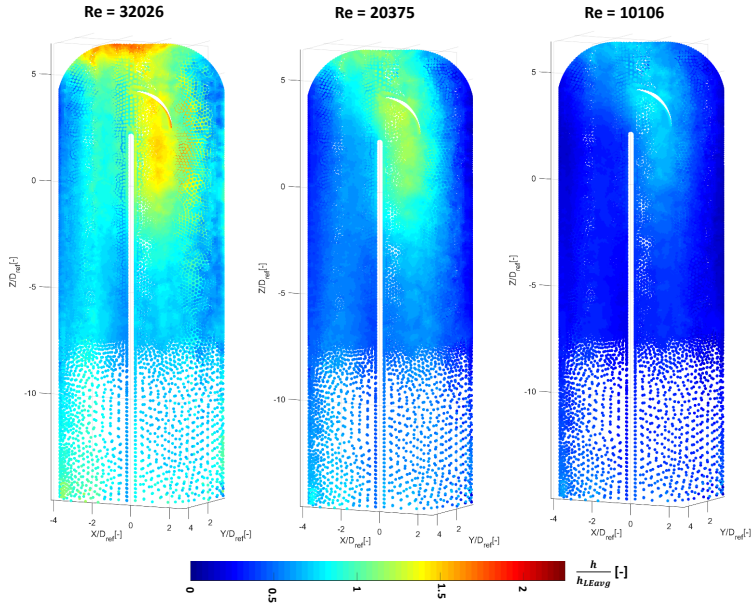


Figure 4.20: Final HTC distribution for  $Re = 32026$  ,  $Re = 20375$  and  $Re = 10106$

#### 4.2.2 Effect of Re number

As previously reported, the heat transfer measurement is performed using different coolant mass flow rates, corresponding to different Reynolds number values. By reducing the mass flow rate the heat transfer phenomenon will also decrease, so to have more reliable data the transient test duration is increased according to each mass flow rate. This is the

only condition revised as compared to the first case. We considered 40 second for  $Re = 32026$ , 50 second for  $Re = 20375$  and 60 second for  $Re = 10106$ . The final results of of such analysis are presented in fig 4.20. Internal channel HTC value distribution pattern is same for each case but the value decrease as mass flow rate decrease. In each case all of the internal cooling channel features are prominently highlighted.

### 4.2.3 Comparison with literature data

For comparison with a literature data we consider average HTC value on a selected region of LE channel as shown in the fig 4.21. This average HTC value is used to find  $Nu$  with help of a relation  $Nu = \frac{Dh}{k}$ , where  $h$  is the average HTC value,  $D$  is the characteristic length and  $k$  is the thermal

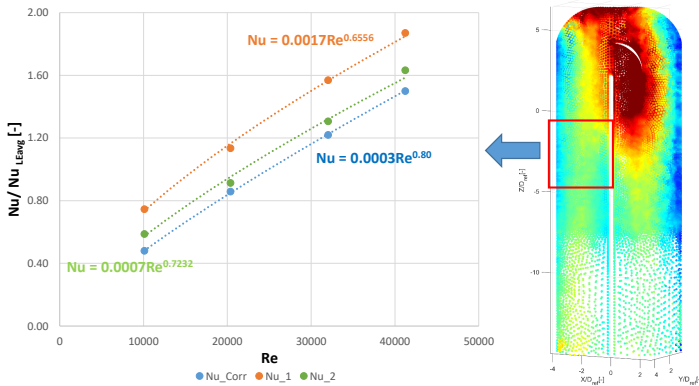


Figure 4.21:  $Nu$  vs  $Re$  for correlation and two different fluid model approaches

conductivity of the fluid. Thermal conductivity is calculated by assuming:  $T_{film} = \frac{T_{aw} + T_W}{2}$ ,  $T_{aw}$  is the fluid temperature and  $T_W$  is internal wall temperature.  $Nu$  for this region is calculated for each case and is compared to Dittus-Boelter correlation [59] which is demonstrated in the fig 4.21. As stated before we used two different fluid model approaches, so  $Nu_1$  in the chart present the first one while  $Nu_2$  is the second one. while

Dittus-Boelter correlation result is presented by Nu\_Corr. Although both of the obtained data closely follows the trend ( $Nu \propto Re^{0.8}$ ) but in the first case the values are very large as compare to the correlation values. This was the reason we proceed to the second approach, by using this approach we obtained value which are much closer to the correlation than the first one.

#### 4.2.4 Concluding remarks

Two different geometries, a circular duct and blade with U-bend internal channel were chosen for testing during the development phase of the proposed methodology. A number of tests were performed with different Re number for each cases. The obtained results were compared against literature data and good agreement was revealed in both cases. The main purpose of testing these preliminary test case was to develop our procedure for implementing it on the real gas turbine coolant geometry. We find in both cases very satisfactory results with proposed procedure and now we have all tools and skill to implement it on real gas turbine coolant geometry.



## Chapter 5

# Industrial Application

The main goal of this thesis is to develop a methodology for measurement of heat transfer coefficient of real geometry. As discussed before that many people have already described different methods for measurement of HTC but mostly are implemented on scaled-up models of the actual geometry at ambient conditions. By doing so we lost many complex geometric and flow features of the real geometries. Also the scaled-up models of the geometries are more simplified for overcoming many measurement constraints. So we introduced a methodology which will be implemented on actual geometry. The procedure was already well explained and implemented on the basic line geometries which were discussed in chapter 4 providing reliably results. In this chapter we will introduce this procedure to real geometry: a BH's engine nozzle. We will calculate the internal HTC of this vane for different Re and also try to detect some controlled faults in the vane's cooling network using our methodology.

### 5.1 BH's engine nozzle

The geometry which we will use for investigating is the BH's engine nozzle. Cooling system of this vane is based on two independent fluid flow network (fig 5.1). The acronym LE will be used for the cavity fluid network near the leading edge, while the other one housed in the cavity

near trailing edge will be named with the acronym TE. LE cooling system

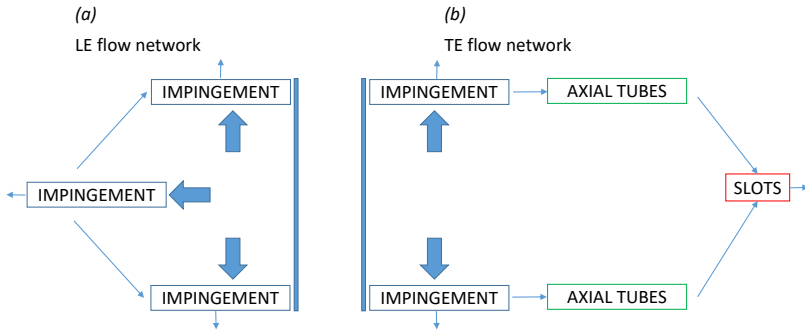


Figure 5.1: BH's engine nozzle conceptual internal cooling network which consists of first cavity network scheme (LE) and the second cavity network scheme (TE)

is characterized by an alternating pattern of impingement jets which impacts on the internal wall surface of the vane. TE cooling system consists of impingement, and axial tubes which contains several pin-fin batteries and channels slot to discharge the exhaust air at the trailing edge of the vane. This cooling architecture is typical of a high-pressure nozzle for engines within 40 MW as developed in the last 15 years.

### 5.1.1 Test rig rearrangement for the vane

Some rearrangement will be needed to place the vane on the test rig and connect with the air supply system. In the previous cases the geometries had extruded part (specially in the case of the blade with u-bend internal channel) for connecting it with the air supply system. Since this vane is taken from a real engine environment there is no such arrangement. Now for connecting it to the air supply system we need to have a intermediate design structure between the vane and air supply system which is shown in fig 5.2. It consists of three parts pipe, pipe disc part and telfon part. The pipe from one end is connected with air



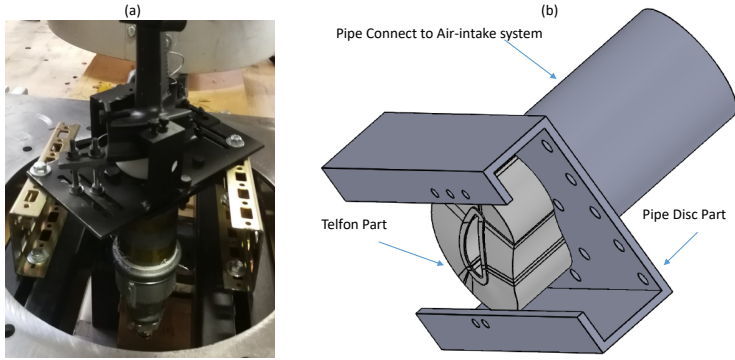


Figure 5.2: (a) Vane connection with Air-intake system (b) CAD of the intermediate structure

supply system while at the other with pipe disc part. The pipe disc part performs two purposes one as a connection to the pipe and the other as a support to which the vane can be fixed. This part is further connected with other supports which help in keeping the whole test rig intact during high pressure testing . The third part is the Teflon part which is placed between the vane and pipe disc part which also act as insulator. It is gloved with vane using thermal silicon paste which helps in blocking any leakage of air. Thermocouples were inserted in the teflon part for measuring the coolant temperature during the transient test (fig 5.3(a)). These were inserted at different location to have more reliable data. Figure 5.3(b) shows the vane position inside the oven during heating phase.

### 5.1.2 Camera view

As mentioned in chapter 3 for getting full 3D surface temperature history of the vane during the transient test we will require aluminum surface mirror. The main camera view will be fixed upon the leading

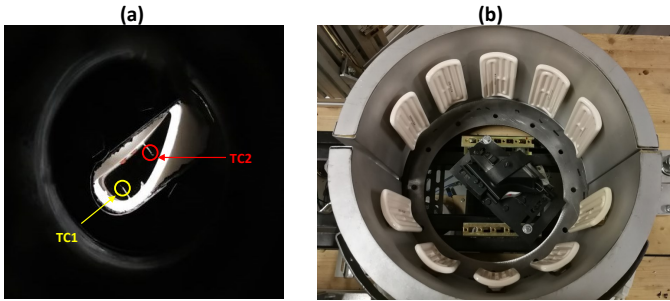


Figure 5.3: (a) Thermocouples position inserted inside the teflon part (b) Vane placement inside the oven during heating phase

edge while the suction side and pressure side will be seen through the mirrors. The mirrors will be placed on the positions as observe in the fig 5.4. The IR camera will record the surface temperature of the vane during the transient test that will be used for 3D mapping procedure which we already discussed in chapter 3.5. This will provide us the 3D surface temperature history of the vane during the transient test. This full 3D data will be used to calculate the initial HTC using LTCM approach and also as initial boundary condition for the FEM procedure. The final surface temperature shown by the fig 5.4 of the transient test will be compared with FEM final output.

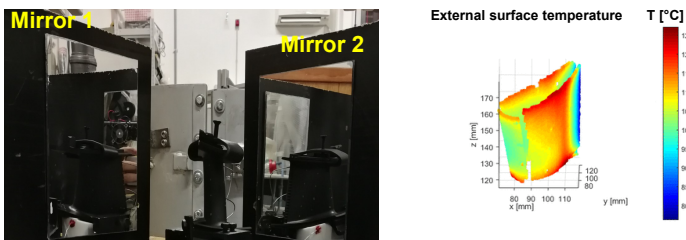


Figure 5.4: (a) Camera view with two aluminum surface mirror (b) Final surface temperature at the end of transient test

### 5.1.3 Replicating engine condition

The main theme of this work is to test actual gas turbine vane. For this purpose we also need to replicate the real engine running conditions in our testing facility. A test matrix is developed for achieving this goal.

Table 5.1: Replicating engine condition on test rig

S.no	Re <sub>measured</sub>
1	2031
2	4082
3	6145
4	8138

The table 5.1 show such test matrix where we consider four test cases with each one having a different Reynolds number which is referred to the diameter of the impingement jet hole.

## 5.2 Heat transfer calculation

In this section we will try to calculate the heat transfer coefficient of this vane with the help of our proposed methodology already discussed in chapter 2 . Starting with the  $Re = 8796$  case, the experimental part of our procedure for the vane will be the same as the previous geometries previewed in chapter 4. First the vane will be heated in the oven to a certain temperature(220 °C). The temperature will be continually monitored during the heating phase with the help of thermocouples placed inside in the oven. After achieving the desired temperature the oven is removed and mirrors are placed on the already decided position. After that a coolant of fixed mass flow rate representing the  $Re = 8796$  case is introduced to induce the thermal transient during which the IR will record the external surface temperature of the vane which is 2D in nature. Using 3D mapping procedure explained in chapter 3 converts this into full 3D which ends our experimental part.

The nozzle FEM model consists of  $6.112 \times 10^5$  *Solid87* 10 nodes tetrahedrons elements . The model include every details of the internal cooling system like pin batteries,impingement box and the TE channel slots. The material properties needed for our thermal FEM model of the Nozzle were provided by our industrial partner. We also required other boundary conditions like initial temperature obtained from the IR data, external convection and radiation, coolant temperature and initial internal HTC which will be calculated using LTCM approach.

Both natural convection and radiation on the outer surfaces of the sample were modeled in the actual FEM model, using the formulations made available by the solver (ANSYS Mechanical v18). In particular, radiation was modeled as a radiative heat transfer towards the environment (“To Ambient” condition), by setting the measured ambient temperature and calibrated paint emissivity. On the other hand, natural convection was imposed as a convective load using the same measured ambient temperature and a heat transfer coefficient value derived from literature correlations [54].After getting all these boundary conditions the FEM of the vane is implemented.

### 5.2.1 LTCM heat transfer coefficient

The LTCM approach which is used for finding the initial HTC of a geometry is already discussed and implemented in the case of circular duct and a blade with U-bend internal channel. In both cases mostly the heat transfer takes place on the internal surface of the geometry when the coolant was introduced. In the previous, getting initial HTC by the LTCM approach was easy because there was no a complex internal cooling network scheme inside the geometry.

But in this case the vane has a complex internal cooling network which consists of impingement on the internal wall surface, pin-fin and channels slots each having different effects on the heat transfer phenomenon. Three different phenomenons attribute to the vane internal wall cooling at pin battery region which are listed below and shown by the figure 5.5.

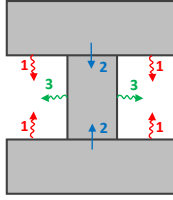


*Figure 5.5: Three different phenomena(Endwall convection(1), wall to pin conduction(2) and Pin convection(3)) attribute in heat transfer*

1. Endwall convection
2. wall to pin conduction
3. Pin convection

Now the issue is that the pin-fin surface are not accessible to IR camera so inverse heat transfer for LTCM will be strongly ill-conditioned on this, so some hypothesis will be needed. By including the pins in the FEM model will take account of wall to pin conduction. The other two phenomenons endwall and pin convection both needed to be discretized with the help of available literature data.

Many researcher proposed different theories about the heat transfer of pin vs endwall. Some suggest that the heat transfer at pin is much higher than endwall. Van fossen(1981)[18] find out that pin has 35% higher heat transfer than endwall for pin of different geometric parameters like surface to diameter ration ( $S/D = 3.46$ ) and a range of height to diameter ratio ( $0.5 \leq H/D < 2$ ). Metzger [61] concludes it is double for  $2.5 \leq S/D \leq 3.5$ ,  $1.5 \leq X/D \leq 3.5$ , and  $H/D = 1.0$ . While some find it similar or lower up to 35 % on pin as compare to endwall [[62], [63]].

These studies lead us to different and contradictory conclusions. The reason behind this was the imperfect or unrealistic thermal boundary conditions assumed in theses studies. Both pin and endwall were not generally both heated at the same time. Chyu [60] studied a case in which

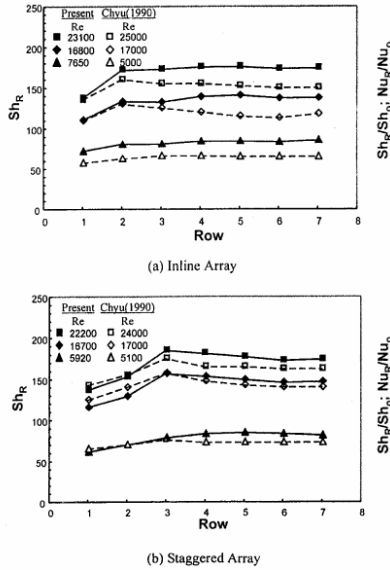


Figure 5.6: HTC comparison on the pin surface with endwall [60].

both pin and endwall wall were thermally active. He found that the heat transfer has a range from 10% to 20% at pin as compared with endwall for different geometric feature ( $S/D = X/D = 2.5$  and  $H/D = 1.0$ ) and Reynolds number ( $5,000 \leq Re \leq 25,000$ ). The following fig 5.6 shows the comparison of the HTC on the pin surface for both his previous and present studies.

Li studied [64] heat transfer phenomena of elliptic pins. He found out that the difference at the lower Reynolds numbers is quite large but with the increase of  $Re$  the difference decreases quickly. For example, for more compact array, Pin Nusselt number is about 22.6% higher than endwall Nusselt number at  $Re=1500$  but only 2.24% at  $Re=7000$  (fig 5.7). Yeh and Chyu (1998) studied heat transfer taken place in staggered pin fin

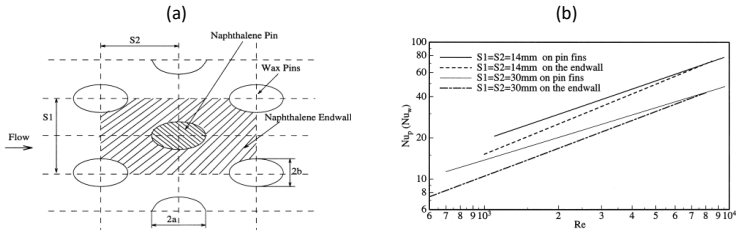


Figure 5.7: (a) Configuration of elliptic pins and their arrangement (b) Comparison of heat transfer rate between pin fins and endwall [64].

arrays[65]. They studied the heat transfer of the pin as compared to endwall for  $H/D = 1 - 2.8$  and  $Re_D = 9000 - 29000$ . They find that the heat transfer on the pin is greater than endwall from 1 to 10 % for  $H/D = 1$  pins while for  $H/D = 2.8$  pins it is from 10 to 20 % (fig 5.8). Other researcher like cunha(2006) [66] and Lyall et al.(2011) [67] also find out the pin fins have higher heat transfer than endwall.

Even so it is not easy to make any conclusion regarding heat transfer at pin vs endwall from the literature review. Different opinions are developed which depends upon the geometry, the boundary condition and also the experimental setup employed to retrieve the data. But still mostly people find that heat transfer phenomena at pin is higher than endwall from 10% to 30%.

For this study it has been evaluated as reasonable to impose a 20% higher HTC on the pin with respect to the endwall. We considered a equivalent  $h_{eq}$  on the pin area which will be 20% higher than the endwall as shown in the fig 5.9. Such condition will be imposed at the first 3D HTC value derived from the LTCM from the data obtained with IR camera. The fig 5.10 shows the LTCM HTC which will be also used in vane FEM procedure as a boundary condition. To make the data dimensionless the XYZ axes are divided by  $D_{ref}$  which is the diameter of the impingement hole while HTC value is divided by  $h_{ave\_LE}$  which is the average HTC value on LE of the vane.

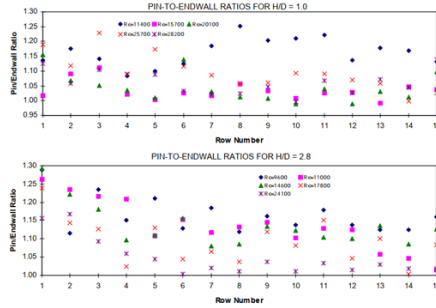


Figure 5.8: *Pin vs Endwall for  $H/D = 1 - 2.8$  [65].*

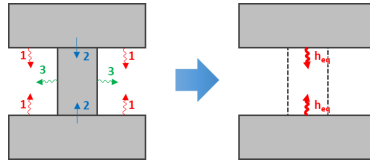


Figure 5.9: *Equivalent heat transfer on pin area*

## 5.2.2 Camera view limitation

Figure 5.11 shows the external surface temperature obtained with 3D mapping procedure from the IR camera data and the internal HTC/LTCM distribution of the vane. It can be noticed that the area where temperature is actually measured does not cover the whole internal surface. Since heat transfer data needs to be known in every internal location in order to provide a proper boundary for the FEM, data in the regions falling outside of the measurement range need to be extrapolated. The area on the bottom and top of the van which is highlighted green in the fig 5.11 are covered with fillet from external side, that is why the camera could not records the external surface temperature of this region. On the other hand, the grey area is the channel slot opening from where the coolant exhausted so camera readings were not more reliable there. As



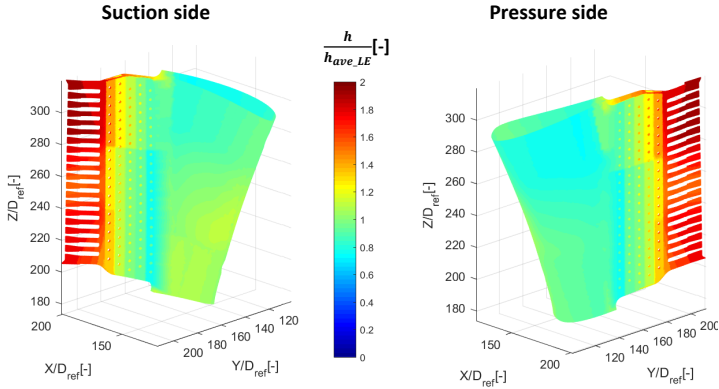


Figure 5.10: Internal HTC distribution of the vane obtained with LTCM approach

we already mentioned that HTC distribution will be extrapolated in these area, which may not the represent the reality. So from now on we will colored the values in this region with grey, so that it can be differentiate from the reliable data as example it is shown in the fig 5.12.

### 5.2.3 Final results

As discussed before in section 2.1.3 the fluid model method worked on the simple geometries cases but as we move to more complex geometries it doesn't provide reliable results. The reason is the fluid model inability to predict the correct coolant temperature at some region i.e. at LE, which results into diverging iterated HTC values. Therefore we introduced regression which provided more reliable and converging results as compare to fluid model.

Regression as described in section 2.2 requires to divide the whole thermal transient test duration (32 seconds) in further sub-steps. For first case ( $Re = 8796$ ) each sub-step will be of 4 second duration and the total number of sub-step will be eight but we will excluded the results of first sub-step because some seconds are required to allow the flow to settle. FEM

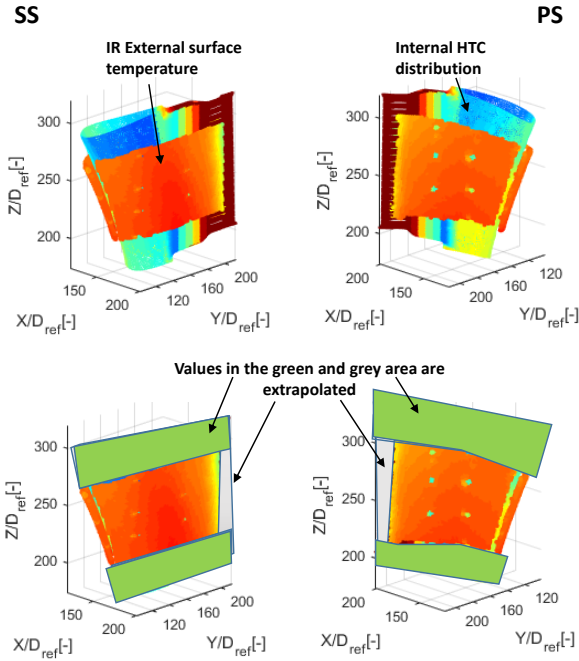


Figure 5.11: External surface temperature map vs internal LTCM HTC distribution

model of the vane is implemented for each 4 sec duration with boundary conditions like initial temperature, external convection, radiation, initial LTCM HTC and coolant temperature measured with thermocouples insert at the inlet of the vane. Some of these boundary conditions like initial temperature, initial LTCM HTC and coolant temperature will be obtained from the experimental part. At the end, the FEM output external surface temperature ( $T_{FEM}$ ) will be compared with the surface temperature ( $T_{Exp}$ ) recorded by IR. If the initial LTCM HTC represents the reality both will be same otherwise we have to iterate the HTC using procedure already mentioned in section 2.1.2 until convergence between

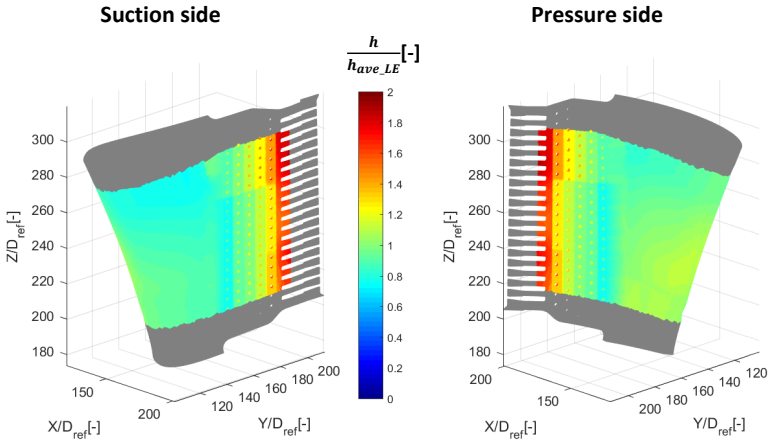


Figure 5.12: LTCM HTC distribution with masking the data of unreliable area with grey color

$T_{FEM}$  and  $(T_{Exp})$  is reached. From that final internal HTC distribution the heat flux  $q$  is calculate using the equation  $q = h(T_{wall} - T_{air})$ .

This whole process was repeated for each sub-step implementing FEM with boundary conditions obtained at that step, comparing the output results with experimental one until convergence was achieved. At the end of the all sub-steps we have corresponding  $T_{wall}$  and  $q$  for each sub-step. By plotting this  $q$  value against  $T_{wall}$  for each point of the vane's internal duct and using linear regression the HTC value can be retrieved. Considering a constant fluid temperature and a variable wall temperature,  $q$  vs  $T_w$  or  $q$  vs  $(T_w - T_f)$  can be fitted within lines of same slope. As a consequence, it is possible to retrieve the value of  $h$  from local heat flux and wall temperature only, since the knowledge of flow temperature is not needed. Moreover, in this case adiabatic wall temperature can be obtained by extrapolating the linear relation to zero heat flux [68].

In general terms, it can be directly verified from equation ( $q = h(T_{wall} - T_{air})$ ) that the error introduced on HTC estimation by approximating the flow temperature as constant along a given time step is equal to

$\Delta T_f/\Delta T_w$ , e.g. the wall temperature variation needs to be at least 20 times larger than the flow temperature one to retrieve a HTC value with less than 5% difference with respect to the correct one. An example of the

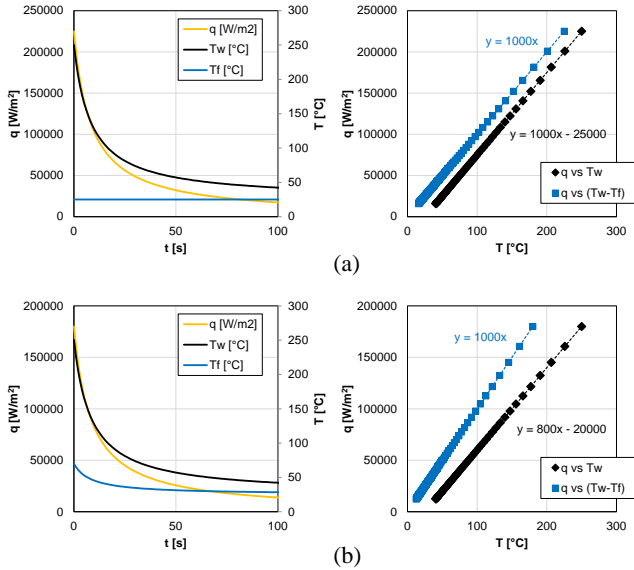


Figure 5.13: Effect of fluid temperature on the regression result

error introduced by neglecting flow temperature variation is illustrated in fig 5.13, where linear regression is carried out for a sample HTC value of  $1000\text{W}/\text{m}^2\text{K}$  using synthetic  $T_w$  and  $T_f$  evolutions. In particular, fig 5.13(a) reveals that a constant flow temperature ( $T_f$ ) has no effect on the HTC value because performing regression using  $T_w$  or  $(T_w - T_f)$  will provide same slope. But a variable flow temperature will produce a different results as demonstrated by fig 5.13(b).

**Retaining the fluid model** If the estimated fluid temperature variation during the test is comparable to wall temperature then it is necessary to evaluate its evolution in space and time. A meaningful way of finding

the flow variation is to introduce a fluid model inside the test article as same as discussed in chapter 2.1.2. By taking in account the inlet temperature and flow rate it must provide flow temperature at every location. In this, such flow model can be fed with the local heat fluxes provided by the FEM simulations at every time step, which correspond to the energy actually transferred from the solid to the fluid. From zero-dimensional model to full transient 3D CFD complex models are suitable for this purpose, however using just simple model which based upon energy balance can provide satisfactory results. In particular, given that the mass flow rate in every section of the component is known, the internal heat transfer surface can be divided into sectors, each with a single inlet and a single outlet for the flow. If the wall heat flux and the inlet flow temperature  $T_{in}$  are known, energy balance allows to retrieve the outlet flow temperature  $T_{out}$  of the sector:

$$T_{out} = T_{in} + \frac{\int_S q dS}{mc_p} \quad (5.1)$$

where  $S$  is the sector heat transfer surface,  $c_p$  is the flow specific heat capacity and  $m$  is the mass flow rate of the sector. The spatial resolution of temperature can be improved by decreasing the size of a single sector. Applying this model to the whole internal surface at a given time step, starting from a measured inlet temperature for the test article, provides a bulk temperature value  $T_f$  for the flow in every location, thus allowing to retrieve the correct  $T_w - T_f$  difference to be employed for the linear regression and so to obtain the right local HTC value. The procedural flowchart of the whole method is demonstrated in the fig 5.14. Figure 5.15(a) shows the heat transfer distribution acquired by applying the proposed technique to the investigated vane. As discussed before, using the current setup a reliable measurement of surface temperature is only possible on the vane itself, while no useful data is available neither for the hub and tip platforms nor for the filleted regions connecting the platforms to the van. As a consequence, the inner surfaces lying inside the hub and tip platforms are not included in the analysis. The terminal

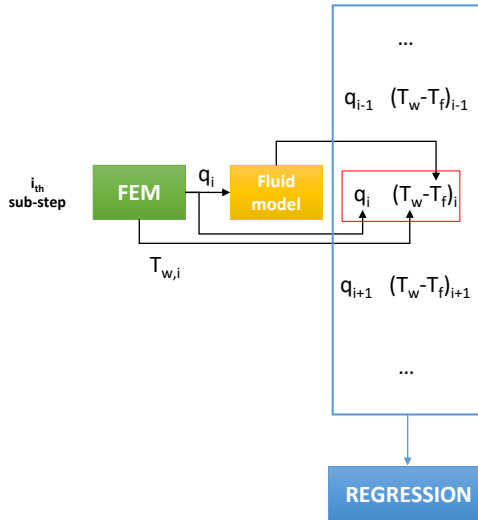


Figure 5.14: Procedural flowchart which combine fluid model with regression

part of TE ducts is also excluded, since in this region heat transfer can be significantly affected by spurious effects (e.g. forced external convection related to the entrainment of the surrounding air) and by the aforementioned compressibility effects along the ducts themselves.

The obtained results enable us to notice the heat transfer magnitude and pattern which is associated with the various features of the internal cooling scheme, also achieving a magnified resolution. Particularly, considering LE region it can be observed that the largest heat transfer values are found along a thin area aligned with the axis of the vane, located close to the actual LE of the vane. This feature could identify the region where impingement jets are not affected by crossflow, i.e. by the spent coolant flow from upstream impingement holes [69].

Coherently with this supposition, heat transfer perpetually decreases moving towards the TE, up to half the nozzle chord: in this region,

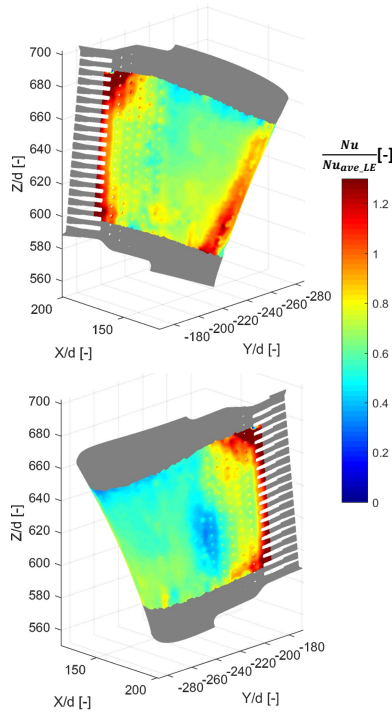


Figure 5.15: Heat transfer distribution obtained for the maximum  $Re$  value

impingement jets are expected to be deflected by the upstream crossflow, which grows stronger along the discharge direction. This phenomenon also provides a possible explanation to the fact that heat transfer is larger on the pressure side with respect to the suction side. In fact, starting from the high heat transfer region and moving along the vane internal surface, a longer path is required to reach the midchord region passing from the suction side with respect to the pressure side: this may lead to a larger crossflow effect for the impingement holes on the suction side, and thus to lower heat transfer values. A drop in heat transfer values

appears to be present in between the impingement and pin fin regions (particularly visible on the suction side), which may be attributed to the sudden enlargement in passage section and to the absence of turbulence promoters. Considering the pin fin region, an opposite trend is recorded with respect to the impingement region, since heat transfer appears to strongly increase moving towards the trailing edge. This phenomenon is likely due to the converging shape of the vane, which progressively decreases the passage area and thus leads to larger flow velocities. The trend is confirmed in the visible area of the TE discharge ducts, where the largest heat transfer magnitude of the whole cooling system is recorded. Given the employed measurement technique, the influence of the fluid model on heat transfer results increases moving from the inlet to the outlet of the geometry: in this case, it can thus be expected that the pin fin region and especially the TE ducts are particularly affected. As stated above, in the present case obtaining Reynolds number similarity in close-to-ambient conditions leads to a strong flow expansion at the exit of the TE ducts, which may induce relevant compressibility effects and in turn make the estimation of the recovery temperature challenging. Moreover, it is expected that the flow expansion may cause a significant air temperature drop, thus increasing the heat removal and strongly decreasing the wall temperature.

This results is compared to the one which is obtained without the use of fluid model, considering a constant flow temperature (5.16). Looking to the results the region where there is not such variation of flow temperature we find similar  $Nu$  distribution i.e. LE, SS and PS impingement box region. But as move towards the pin batteries region where the variation in the flow temperature increase, the difference between both of them become larger. The  $Nu$  value in the case of regression which consider fluid temperature variation is higher in this region than one which consider constant flow temperature.



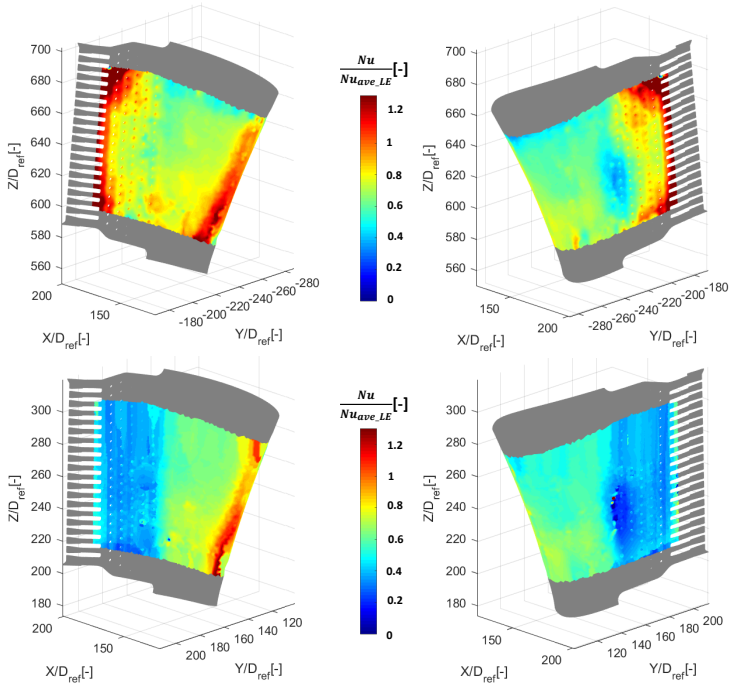


Figure 5.16:  $Nu$  distribution obtained by regression considering variable flow temperature (a) and constant flow temperature (b)

### 5.2.4 Effect of Reynolds number

To find out the effect of the Reynolds number of  $Nu$  we selected the remaining test cases which are  $Re = 6145$ ,  $Re = 4082$  and  $Re = 2031$ . The same methodology will be followed as first case just changing the mass flow rate representing each case. We know the decrease of mass flow rate will effect the overall heat transfer, it will take more time to reach a certain vane external surface temperature during the thermal transient. As already mentioned that the whole thermal transient is divided into eight sub-step each of 4 second duration i.e.  $Re = 8796$  case. At the end

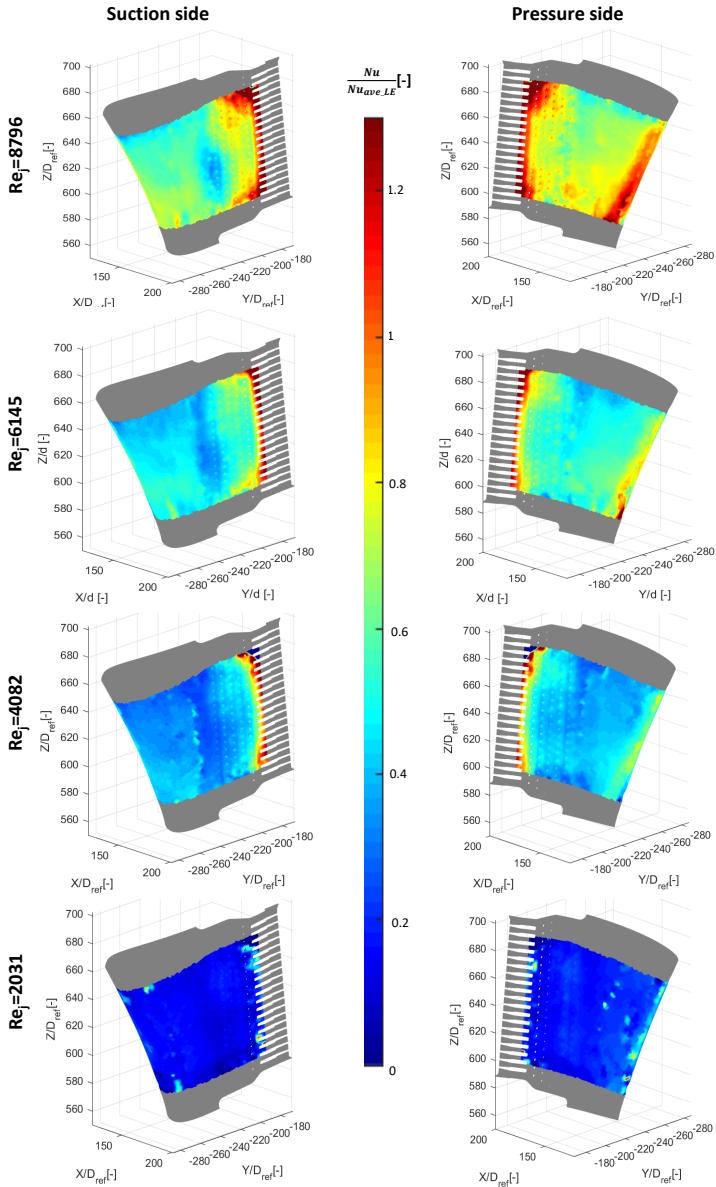


Figure 5.17:  $Nu$  distribution of SS and PS of the vane for all test cases

of the thermal transient(32 second) we achieved a certain vane external surface temperature. Now if want to achieve the same vane external surface temperature for other cases at the end of thermal transient we have to increase the total time duration of the thermal transient, 40 second for  $Re = 6145$  case, 56 second for  $Re = 4082$  case and 92 second for  $Re = 2031$  case. By keeping the same number of the sub-step for all case, each sub-step duration must increase to 5 second, 7 second and 12 second for  $Re = 6145$  case,  $Re = 4082$  case and  $Re = 2031$  case. This is the only condition which is changed as compared with first case. The HTC for all the cases shows same overall distribution pattern as demonstrated by the fig 5.17. As we move towards the lower mass flow rate the HTC value decrease.

### 5.2.5 Comparison with literature data

The final result is compared with correlation which were taken from the open literature([70], [71]). The internal cooling network was appropriately modeled through BANKS solver where correlations from the open literature were used. The model implements dedicated models for each impingement, pin-fin and channels slots, based on correlative approach.

Impingement models are solved using pressure losses and heat transfer coefficient correlations developed by Florschuetz et al. [69], pin-fin using Faulkner [20] and Metzger et al. [19] correlations, Goldstein [72] adiabatic effectiveness formula is used for the trailing edge slot cooling.

A direct local comparison with experimental data is possible by plotting the data from the correlations on the internal surface of the vane, which is performed in fig 5.18 for a sample test ( $Re=6145$ ). It can be noticed that the obtained results fit satisfactorily with the correlation values. In particular, both experimental and predicted distributions present a thin, vertically elongated region of large heat transfer at the leading edge, and the location of such region is the same for the two approaches. Considering the front region of the vane, in both cases a slightly increasing trend is retrieved for heat transfer moving from the tip to the hub. Values are also very similar in this region. Moving towards the trailing edge, a

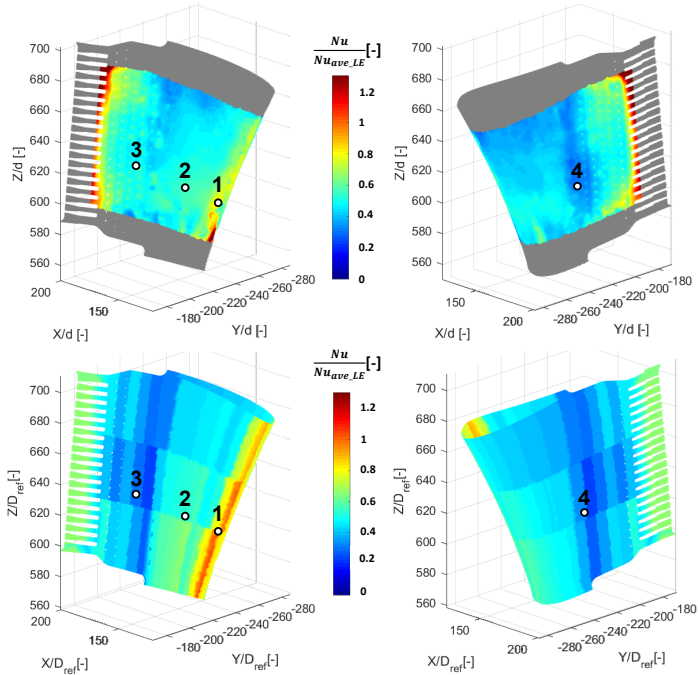


Figure 5.18: Comparison of experimental (up) and correlation data (down) for  $Re=6145$  test

decrease in heat transfer values is retrieved in both cases at the end of the impingement region, even if its magnitude on the pressure side is different between experiment and correlation. Finally, both approaches provide an increasing trend moving along the pin rows towards the discharge ducts, even if the magnitude of such growth is larger for experimental data.

A quantitative comparison between predicted and measured values can be retrieved if data is directly compared for a series of points: this is carried out in fig 5.19 for the points indicated in fig 5.18 and for the different investigated  $Re$  values. The charts of fig 5.19 reveal that a

reasonable agreement is present between experimental and correlation data in different locations of the leading edge region throughout the whole investigated Re range: in particular, similar values are obtained in both the high (point 1) and low (point 2) heat transfer regions. Comparable

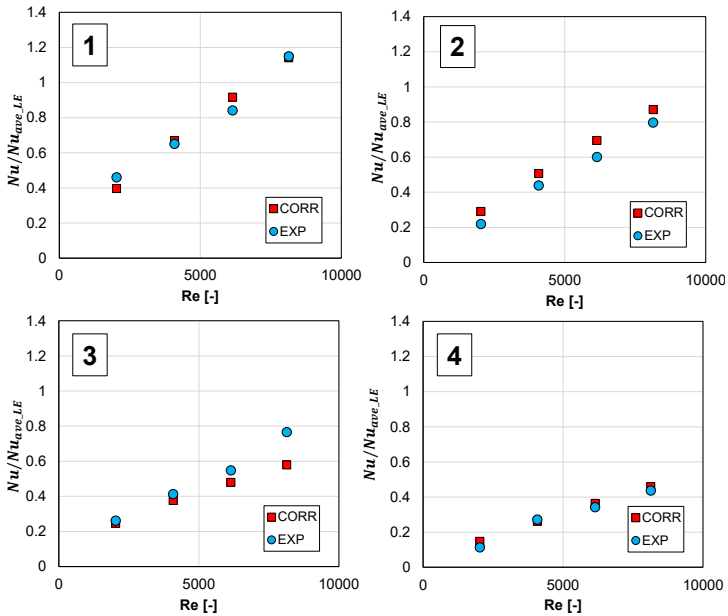


Figure 5.19: Comparison of experimental and correlation data in specific locations

values are also retrieved in the region of low heat transfer in between the impingement and pin fin zones (point 4). On the other hand, if a spot closer to the trailing edge is taken into account (point 3) the agreement seems to depend upon the Re value: in particular, similar values are obtained for low Re values, while correlation and experimental data tend to diverge as Re increases. A possible interpretation of this discrepancy can be related to the compressibility effects which are likely to occur in these regions: in fact, as already reported large Mach number values may

be present in the final part of the cooling system, which may affect the air temperature evolution and thus alter the measurement in this region. On the other hand, the employed correlations do not take into account the effects of flow Mach number, and thus the calculated result may not be totally reliable in these conditions. This interpretation is confirmed by the fact that the agreement is better for low  $Re$  values, where lower Mach numbers and thus less intense compressibility effects are expected.

### 5.3 Fault detection

The qualitative analysis of the any internal cooling network of a vane is based upon the measurement of internal HTC. HTC is the direct suitability check of any cooling scheme, if there is any fault in the internal cooling network i.e blockage of a channel slot or a impingement hole it's effect must be observed in the HTC measurement. The tested vane has no visible fault which can be evidenced from the HTC measurement discussed in the above section. But to test that our HTC measurement procedure has ability to detect any fault, we self-induce three types of fault separately, half of total channel slots blocked, two channel slots

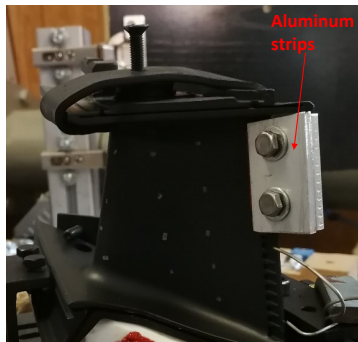


*Figure 5.20: Vane with half channel slots blocked*

blocked and three impingement holes blocked and tried to find out the

effect of these faults on HTC measurement. In the following section we will discuss these three faults and their effects on HTC one by one.

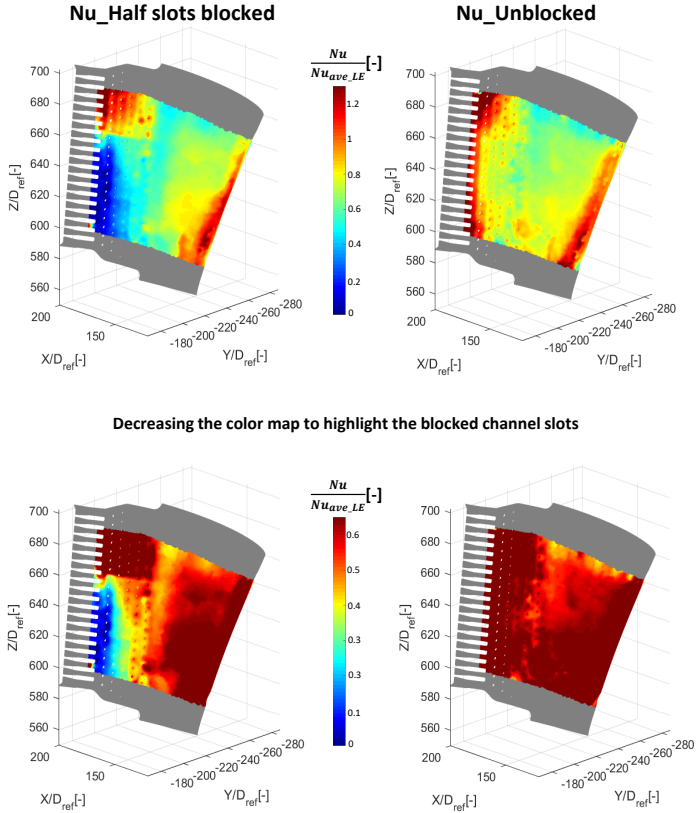


Figure 5.21: Nu distribution for half channel slots blocked and unblocked channels slots

### 5.3.1 Half channel slots blocked

We blocked half the channel slot at TE with help of two aluminum strips as shown in the fig 5.20. The two screws forces the strips against the

vane channel slots with high temperature silicon paste applied between them. Silicon paste can stand upto  $300\text{ }^{\circ}\text{C}$  and can stop any leakage. We will repeat all the step of the procedure as the previous cases. The final results are obtained and compared with the unblocked channel slots case. In fig 5.21 the  $Nu_{\text{Unblocked}}$  represents the result which we obtained where no channel slots were blocked while  $Nu_{\text{Blocked}}$  represents where we blocked half of the channels slots. It must be remembered that these maps are upside down as compare to the vane picture with blocked channels slots shown in fig 5.20. The color scale is decreased so that the difference between them can be easily differentiate. As from the figure this difference is very visible: the  $Nu$  in the blocked channels slots region is very lower as compare with un-blocked case. As there is no coolant flow in this region so there will be very little heat transfer phenomenon,  $Nu$  value almost close to zero and not negative are expected. On the base of these results we can deduce that our HTC measurement methodology has the capability of detecting any fault in the cooling scheme. As in this case we blocked half of the channel slots (10 slots) but what if we want to block less slots than this i.e. 2, did our procedure will able to detect such smaller fault. For this purpose we did another experiment of blocking only two channel slots which will be discussed in the next section.



Figure 5.22: Vane with 2 channel slots blocked



### 5.3.2 Two channel slots blocked

Using the same concept of blocking the channels slot with two aluminum strips as previous case, but in this case it is smaller and V shaped which is demonstrated by the following fig 5.22. We were able to get

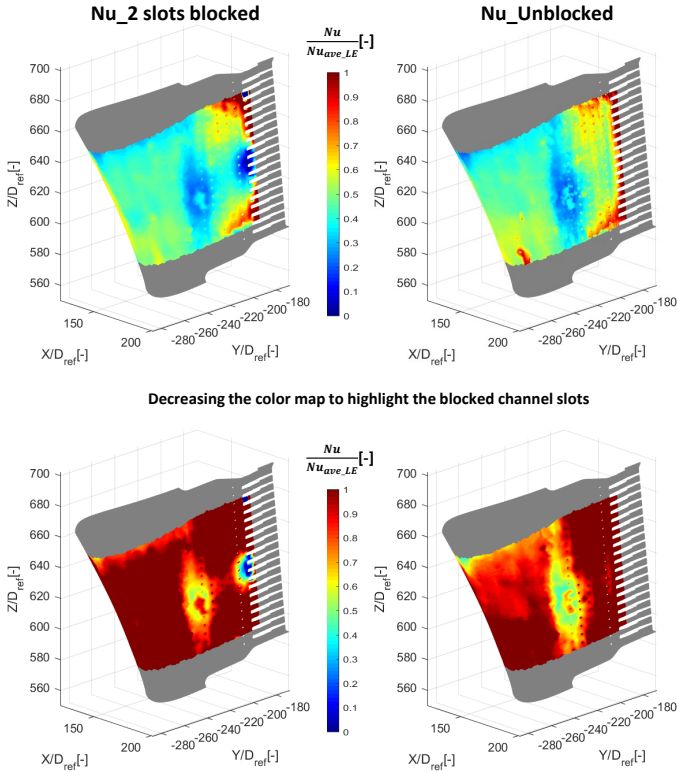


Figure 5.23: Two channel slots blocked vs Unblocked

observable different  $Nu$  distribution in the two blocked channel slots. Figure 5.23 demonstrates the results obtained and analyses this against the un\_blocked case. To show a more meaningful comparison the figure shows clear difference in the  $Nu$  at the blocked slots. This prove sensitivity

of procedure to detect smaller and smaller possible faults in the vane internal cooling scheme.

### 5.3.3 Impingement holes blocking

As in the previous cases we introduced a external fault i.e blocking channels slots. Let induce a internal fault just by applying a thermal tape on three holes of impingement box which is placed inside the vane. The thermal tape has the ability to stand against a temperature range upto  $300\text{ }^{\circ}\text{C}$  which serve our purpose. The area where the impingement holes are blocked have  $Nu$  distribution which is very lower than the unblocked one. This region is highlighted by red circle in the fig 5.24, where we observe the difference of  $Nu$  distribution . We can detect any type of fault in this vane or any other geometry. Our main goal of this work was to have a procedure which can measure the heat transfer coefficient of real geometry and can detect any fault on the base of these measurement.

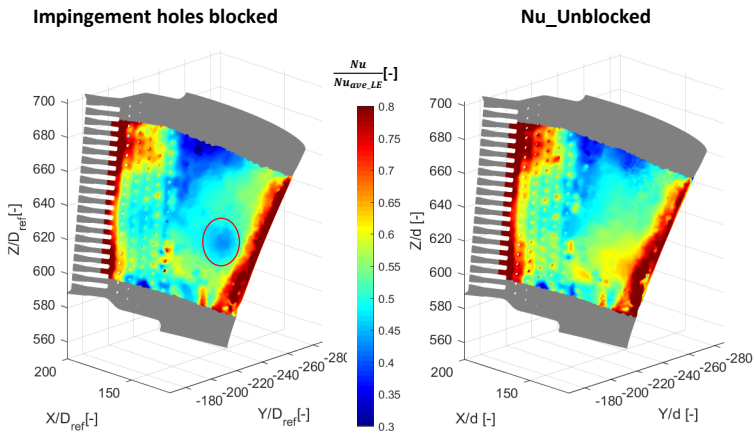


Figure 5.24:  $Nu$  distribution in case of three Impingement holes blocked

## 5.4 Uncertainty analysis

An estimation of measurement uncertainty for complex postprocessing techniques can be obtained by performing a sensitivity to the outcome of the procedure to the uncertainty of the single inputs [50], [73]. In the present case, this was obtained by adding to each input parameter the corresponding uncertainty and comparing the obtained result with the undisturbed one. The result of such analysis is summarized in Table 5.2. The contribution is split in between LE and TE region to highlight the effect of the fluid model, which amplifies the contributions of those parameters involved in the calculation of local flow temperature. The

Table 5.2: Contribution to uncertainty on  $Nu$

Parameter	Uncertainty	Typical contribution to $Nu$ uncertainty	
		LE region	TE region
$T_w$	0.6K	3%	5%
$T_f$	0.6K	0.5%	2%
$m$	0.5%	-	8%
$h_{ext}$	15%	4%	4%
$t$	0.5s	0.8%	3%
$k$	5% $s$	2%	2%
$\rho - c$	5%	5%	15%

single contributions can be combined using a quadratic error propagation model  $\varepsilon_{tot} = (\varepsilon_1^2 + \varepsilon_2^2 + \dots + \varepsilon_n^2)^{0.5}$ , thus retrieving an estimation of the global error on  $Nu$  related to the input uncertainty. A sample outcome of such analysis is reported in Figure 5.25 for the  $Re=4082$  case. The distributions reveal that, as expected, the largest uncertainty values occur in the noisy regions, which can be easily identified in the heat transfer maps (see Figure 5.17): in fact, in these zones the values are mostly driven by local numerical and convergence instabilities. Apart from these regions, an increasing trend is visible moving towards the TE, i.e. as the effect of fluid model on heat transfer increases. In particular, values around 7-8% are common on the LE region, which grow up to 20% for the last rows of pin

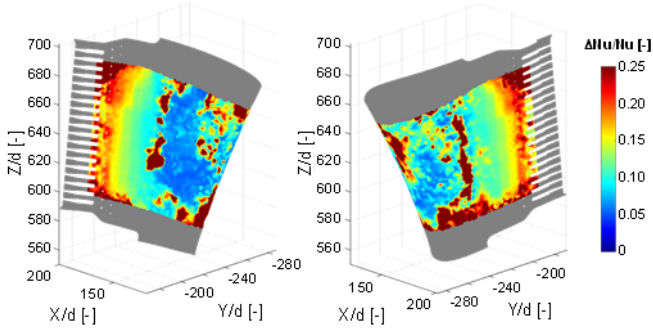


Figure 5.25: Local uncertainty for  $Re = 4082$  case

fins. Considering also noisy regions, the average value of uncertainty for the present case is 16%. Since heat transfer increases with  $Re$  while the magnitude of most uncertainty contribution is constant, smaller overall uncertainty values can be expected for the larger  $Re$  cases and larger values for the lower  $Re$  case.

## 5.5 Concluding remarks

In this chapter we extend our proposed methodology to a real geometry BH's engine nozzle vane with internal cooling scheme which consists of impingement, pin fin and channels slots. We replicated the actual engine condition on test rig and perform experiments with four different flow rates cases starting from  $Re = 8796$  case. The obtained were compared with the correlation results provided by the Industrial partner and provide a reasonable relevance with them. Then we extend our proposed methodology for detecting any fault in the cooling scheme of the vane. We were able to detect some controlled faults and found out that the procedure is sensitive to any size of fault smaller or larger etc.

# Conclusions

A nondestructive procedure is developed, which is used to measure the internal convective HTC of real gas turbine cooled geometry, the technique is based upon Nirmalan [48] approach. Geometry is heated up to a known temperature inside an oven, than a coolant is introduced inside it to induce a thermal transient. An IR camera is used for retrieving the external surface temperature of the geometry during this thermal transient. Then a FEM of the same geometry is performed with boundary conditions like initial temperature of the geometry, coolant temperature during the transient and initial convective internal HTC, which is obtained from the recorded experimental data during the thermal transient using LTCM approach. The thermal transient duration will be same for both experimental transient and FEM: this duration depends upon the mass flow rate of the coolant and geometry features. The external surface output temperature of the geometry obtained at the end of FEM thermal transient ( $T_{FEM}$ ) will be compared with the experimental one ( $T_{Exp}$ ). If the initial HTC obtained with LTCM represents the reality, than both outputs will be the same, otherwise an iterative scheme will be used to find the correct value. The HTC iteration is performed with secant method which uses the previous HTC iterations and temperature difference at these iterations. The iteration will continue until the temperature difference convergence to an already established value i.e. root mean square value of temperature difference must be less than a fixed value. The coolant temperature during the thermal transient is constantly updated with the help of the fluid model, which calculates the coolant

temperature inside the geometry. This fluid model uses the temperature of the coolant at the inlet of the geometry (measured with thermocouples), geometry wall temperature and mass flow rate for calculating the coolant temperature inside the geometry. This model is based upon the energy balance phenomenon, which is implemented section by section of the geometry. Using this model for a simplified geometry provides reliable results, but as we move to more complex geometry some issue may raise because it is based upon very simple energy balance approach. It doesn't provide more reliable and accurate coolant temperature value at some region of the geometry, which makes the temperature difference ( $T_{FEM} - T_{Exp}$ ) value very high in these region. As already stated that we use secant method for iterating HTC which use this temperature difference values. Using these value will cause the divergence of HTC value in these regions.

To solve this issue an updated version of Nirmalan [48] approach is introduced, which we is refereed as regression method. It is different form the previous approach (named fluid model method) by two aspects: one is that the total transient duration is subdivided into sub-step and the comparison between the geometry external surface temperature is performed at the end of each sub-step (not at the end of total transient) and the second one is that the FEM solution is no more coupled with the fluid model, thus obtaining more robust convergence. Our target variable will be heat flux  $q$  in this case ( not HTC as previous case). We will retrieve time-dependent internal heat flux  $q$  and wall temperature  $T_{wall}$  distributions in order to obtain the same external temperature as in the experiment. The final HTC value for whole transient duration is calculated by plotting all these sub-step heat fluxes and temperature values for each location of the geometry and then using linear regression. So to develop our proposed methodology we started from a baseline simple geometry and then move to more complex geometries. The baseline geometry is a circular duct which has 10 mm internal diameter, 12 mm external diameter and 235 mm length. The duct's axisymmetric nature (so comparison of the external surface temperature along one axis is sufficient)

and the availability of related literature data are the reasons behind its selection. Since the geometry is simple the first methodology provided reasonable results. We performed a number of tests with different Re number i.e. 25,000, 50,000 and 75,000. For each case, the results differ from the values obtained by correlation by less than 3%. An uncertainty analysis is carried out which results uncertainty of  $\pm 5\%$  in the measured data.

The second case we consider for experimentation is a blade with U-bend internal channel, which is built by extruding the midspan profile of a first stage rotor blade with a reduction scale factor of 1.5. This geometry is not axisymmetrical, so full surface temperature comparison will be required. Some addition will thus be required to the procedure: the first one is that we need to have a full view of the external surface of the geometry during the transient test. This is achieved with one IR camera which focus on LE while seeing PS and SS through two aluminum surface mirrors. The IR recorded image is of 2D nature, thus it needs to be converted to 3D using 3D-mapping scheme, which is our second addition. This 3D external surface temperature of the geometry will be compared with with FEM output at the end of thermal transient test. The remaining procedure will be same as in the case of baseline geometry, starting with initial LTCM HTC and then iterate HTC until convergence between  $T_{FEM}$  and  $T_{Exp}$  is reached. As the previous case we will perform different tests by considering different Re number and will notes their effect on the internal convective heat transfer coefficient. The results are compared with correlation by considering a average value at a selected region of the the U-bend internal channel close to LE.

After the development of the proposed methodology on some baseline and less complex geometries, we moved to more a complex geometry i.e. a cooled high-pressure vane of a Baker-Hughes heavy-duty gas turbine. Since the geometry is taken from real engine environment, so some modification in the test rig is required to fix the geometry on test rig stand. In this case, regression method was employed since the fluid model method was not able to provide converge HTC evolution 2.1.3.

As mentioned before the HTC value will be retrieved from  $q$  and  $T_{wall}$  or  $T_{wall} - T_{air}$ . As long as the  $T_{air}$  is constant linear regression will provide same HTC value by plotting  $q$  against  $T_{wall}$  or  $T_{wall} - T_{air}$  because in both case we have linear same slope lines. But if the  $T_{air}$  is not constant then it will affect the final HTC value. This effect will be more visualized in the region close to TE where  $T_{air}$  is changing a lot. Now to solve this issue the fluid model is retrieved again just for find  $T_{air}$  variation inside the geometry and performing the regression method with the already obtained  $q$ , and  $T_{wall} - T_{air}$  for each sub-step. The HTC results will not be affected much in the region where  $T_{air}$  is constant but will have different values where  $T_{air}$  is variable as compared to previous regression(which consider constant  $T_{air}$ ) results.

The results is compared to expected heat transfer values obtained from literature data, to assess the reliability of the analysis. The internal cooling network was appropriately modeled through BANKS solver where correlations from the open literature were used. It is noticed that the obtained results fit satisfactorily with the correlation values.

The proposed methodology is meant to measure HTC performance of real gas turbine cooled geometries, which can be also used for the detection of some faults in the internal cooling scheme of this geometry. Since the tested vane has no faults some controlled faults are introduced to evaluate this procedure for their detection. Three types of faults are considered: half channel slots blocked, two channel slots blocked and three impingement holes blocked. In each case the heat transfer measurement obtained with our procedure significantly identifies the region where the fault occurs, which also proves the sensitivity of our procedure for detecting any fault of any size.

Hence, the present work provides a heat transfer measurement methodology for actual gas turbine cooled geometry. This can be considered a suitable technique to investigate complex internally cooled components, as well as to perform a preliminary verification for real hardware devices in order to identify internal defects and their effect on the cooling performance.



# List of Figures

1.1	Improvement of specific power output with TIT [7]. . . .	3
1.2	TIT and material limit temperatures during the years [8].	4
1.3	Example of cooled gas turbine blade (a) and corresponding internal cooling system (b) [13]. . . . .	6
1.4	Radial single and multi-pass cooling channels,[15]. . . . .	7
1.5	Scheme of flow field induced by ribs [16]. . . . .	8
1.6	Schematic of a pin-fin array at the trailing edge of a gas turbine airfoil, [17]. . . . .	9
1.7	A typical test model for dimple cooling studies with a conceptual view of dimple induced secondary flow, [24]. .	11
1.8	Scheme of flow regions in an impingement jet, [25] . . . .	12
1.9	Classification of heat transfer measurement techniques [32].	13
1.10	Schematic of Nirmalan approach [48]. . . . .	15
2.1	Fluid Model Method. . . . .	20
2.2	A section of the geometry. . . . .	22
2.3	Post processing procedure flow chart. . . . .	24
2.4	Final HTC distribution obtained with fluid model method	26
2.5	Coolant temperature calculated by fluid model vs actual temperature. . . . .	27
2.6	Temperature difference between FEM and Experimental one at 3rd iteration and Nu obtained at fourth iteration. .	28
2.7	Heat flux vs $T_{wall}$ for a single location for all 7 sub-step .	29

2.8	Comparison of HTC obtained by fluid model with the one obtained by regression . . . . .	30
3.1	A generic layout of the complete test rig . . . . .	34
3.2	Heating system consisting of oven, variance and guide rail with carriage . . . . .	35
3.3	(a)oven drawing and (b)top view . . . . .	36
3.4	oven CAD model showing the ceramic heater fixed to heater part . . . . .	36
3.5	Variac, RS Pro 1-Phase 4.8KVA . . . . .	37
3.6	Opening the oven after heating and moving along the guided rail . . . . .	38
3.7	Schematic of the air supply system . . . . .	39
3.8	Pressure regulator . . . . .	39
3.9	(a) <i>CORI – FLOW<sup>TM</sup></i> flow-meter (b) Schematic of a Coriolis flow sensor . . . . .	40
3.10	Schematic of the thermographic system . . . . .	41
3.11	Aluminum Bar used for paint calibration . . . . .	44
3.12	Images taken by IR by placing the bar at certain angle to its normal . . . . .	45
3.13	Plot of angles vs emissivity . . . . .	47
3.14	Positioning the mirror to observe each side of an airfoil with only one IR camera . . . . .	47
3.15	Image taken by IR camera while observing through glass mirror and aluminum surface mirror . . . . .	48
3.16	Schematic of mirror placed at certain angle while test bar is rotated from 10 ° to 80 ° degree . . . . .	49
3.17	Thermocouple reading and mass flow rate during the Transient test . . . . .	51
3.18	sample extracted from the IR data for a blade . . . . .	51
3.19	3D mapping procedure for PS side of a blade . . . . .	52
3.20	Full 3D temperature distribution of a blade . . . . .	54
4.1	Smooth circular duct . . . . .	56

---

4.2	Schematic of circular duct arrangement within test rig . . .	57
4.3	Placement of the black painted duct inside the oven . . . .	58
4.4	Duct surface temperature evolution during the thermal transient . . . . .	59
4.5	Thermocouple reading at inlet and outlet of duct during thermal transient . . . . .	60
4.6	Initial LTCM HTC along the duct X-axis . . . . .	61
4.7	Initial temperature along the duct X-axis . . . . .	62
4.8	(a) HTC iteration (b) Temperature difference at each iteration . . . . .	63
4.9	Final HTC comparison with correlation for $Re$ 50,000 . . .	64
4.10	HTC comparison with correlation for $Re$ 75,000 . . . . .	64
4.11	HTC comparison with correlation for $Re$ 25,000 . . . . .	65
4.12	$Nu$ vs $Re$ . . . . .	66
4.13	Blade with U-bend internal channel(left) and with extruded part(right) . . . . .	67
4.14	Blade positioning inside the test rig with mirrors in place	69
4.15	Dimensionless temperature coefficient (left) and coolant temperature inside the channel (right) . . . . .	70
4.16	(a)IR 2D image of the blade during transient(b) Thermocouple reading at inlet and outlet of the blade . . . . .	71
4.17	(a)External surface temperature of the blade at start of the transient (b) Initial convective internal LTCM HTC .	72
4.18	Thermal grid details . . . . .	73
4.19	Comparison of the final obtained internal HTC vs LTCM HTC . . . . .	74
4.20	Final HTC distribution for $Re = 32026$ , $Re = 20375$ and $Re = 10106$ . . . . .	75
4.21	$Nu$ vs $Re$ for correlation and two different fluid model approaches . . . . .	76

5.1	BH's engine nozzle conceptual internal cooling network which consists of first cavity network scheme(LE)and the second cavity network scheme (TE) . . . . .	80
5.2	(a) Vane connection with Air-intake system (b) CAD of the intermediate structure . . . . .	81
5.3	(a) Thermocouples position inserted inside the teflon part (b) Vane placement inside the oven during heating phase .	82
5.4	(a) Camera view with two aluminum surface mirror (b) Final surface temperature at the end of transient test . .	82
5.5	Three different phenomena(Endwall convection(1), wall to pin conduction(2) and Pin convection(3)) attribute in heat transfer . . . . .	85
5.6	HTC comparison on the pin surface with endwall [60]. . .	86
5.7	(a)Configuration of elliptic pins and their arrangement (b)Comparison of heat transfer rate between pin fins and endwall [64]. . . . .	87
5.8	Pin vs Endwall for $H/D = 1 - 2.8$ [65]. . . . .	88
5.9	Equivalent heat transfer on pin area . . . . .	88
5.10	Internal HTC distribution of the vane obtained with LTCM approach . . . . .	89
5.11	External surface temperature map vs internal LTCM HTC distribution . . . . .	90
5.12	LTCM HTC distribution with masking the data of unreliable area with grey color . . . . .	91
5.13	Effect of fluid temperature on the regression result . . . .	92
5.14	Procedural flowchart which combine fluid model with regression . . . . .	94
5.15	Heat transfer distribution obtained for the maximum Re value . . . . .	95
5.16	Nu distribution obtained by regression considering variable flow temperature (a) and constant flow temperature (b) .	97
5.17	Nu distribution of SS and PS of the vane for all test cases	98

---

5.18 Comparison of experimental (up) and correlation data (down) for $Re=6145$ test . . . . .	100
5.19 Comparison of experimental and correlation data in specific locations . . . . .	101
5.20 Vane with half channel slots blocked . . . . .	102
5.21 Nu distribution for half channel slots blocked and unblocked channels slots . . . . .	103
5.22 Vane with 2 channel slots blocked . . . . .	104
5.23 Two channel slots blocked vs Unblocked . . . . .	105
5.24 Nu distribution in case of three Impingement holes blocked	106
5.25 Local uncertainty for $Re = 4082$ case . . . . .	108



# List of Tables

2.1	Comparison between fluid model method and regression. .	30
3.1	Specification of Variac RS Pro 1-phase . . . . .	37
3.2	Technical specifications of FLIR system ThermoVisionTM A40M . . . . .	42
3.3	Emissivity vs angle . . . . .	46
3.4	Emissivity vs angle for mirror . . . . .	50
4.1	Test Matrix for circular duct . . . . .	58
5.1	Replicating engine condition on test rig . . . . .	83
5.2	Contribution to uncertainty on $Nu$ . . . . .	107





# Bibliography

- [1] Grand view research, gas turbine market size, share and trends analysis report by capacity ( $< 200mw$ ,  $> 200mw$ ), by technology (open cycle, combined cycle), by application (power generation, industrial, aviation), and segment forecasts, 2018-2025, Jul 2018.
- [2] Hitchin, P. “Complementing renewable energy with gas turbines.” *GE Power Transform*, 2017.
- [3] ICAO. Long-term traffic forecasts - passenger and cargo, Jul 2016.
- [4] ACARE. Strategic research & innovation agenda, 2017.
- [5] EASA, EUROCONTROL EEA. European aviation environmental report 2016.
- [6] Giampaolo, T. *Gas turbine handbook: principles and practice*. Fairmont Press, 2002.
- [7] Han, J.C., Dutta, S., and Ekkad, S. *Gas turbine heat transfer and cooling technology*. CRC Press, 2012.
- [8] Ballal, D.R. and Zelina, J. “Progress in aeroengine technology (1939–2003).” *Journal of aircraft*, 41(1):43–50, 2004.
- [9] Giuntini, S. *Transient modelling of whole gas turbine engine: an aero-thermo-mechanical approach*. PhD thesis, Università degli Studi di Firenze, 2018.

- 
- [10] Pievaroli, M. *Matrix Cooling Systems for Gas Turbine Nozzles and Blades: Experimental Investigations and Design Correlations*. PhD thesis, Università degli Studi di Firenze, 2014.
- [11] Winchler, L. *Design tools and innovative concepts for gas turbine cooling applications*. PhD thesis, Università degli Studi di Firenze, 2016.
- [12] Simpson, T.W. “Am needs mes.” *ASME Mechanical Engineering*, 137:30–35, 2015.
- [13] Amano, R.S. “Advances in gas turbine blade cooling technology.” *Advanced Computational Methods and Experiments in Heat Transfer X*, B. Sunden, and CA Brebbia, eds., WIT Press, Southampton, UK, 2008.
- [14] Bunker, R.S. *Innovative gas turbine cooling techniques*. WIT Press, Southampton, UK, 2008.
- [15] Rolls-Royce plc. *The Jet Engine*. Fifth edition, 1996.
- [16] Han, J.C. “Recent studies in turbine blade cooling.” *International Journal of Rotating Machinery*, 10(6):443–457, 2004.
- [17] Ostanek, Jason K. “Improving pin-fin heat transfer predictions using artificial neural networks.” *Journal of Turbomachinery*, 136(5): 051010, 2014.
- [18] VanFossen, G James. Heat transfer coefficients for staggered arrays of short pin fins. In *ASME 1981 International Gas Turbine Conference and Products Show*, pages V003T09A003–V003T09A003. American Society of Mechanical Engineers, 1981.
- [19] Metzger, DE, Shepard, WB, and Haley, SW. Row resolved heat transfer variations in pin-fin arrays including effects of non-uniform arrays and flow convergence. In *ASME 1986 international gas turbine conference and exhibit*, pages V004T09A015–V004T09A015. American Society of Mechanical Engineers, 1986.

- [20] Faulkner, FE. “Analytical investigation of chord size and cooling methods on turbine blade cooling requirements. book 1: Sections 1 through 8 and appendixes a through i.” 1971.
- [21] Armstrong, JEFFREY and Winstanley, DAVID. “A review of staggered array pin fin heat transfer for turbine cooling applications.” 1988.
- [22] Ligrani, Phil. “Heat transfer augmentation technologies for internal cooling of turbine components of gas turbine engines.” *International Journal of Rotating Machinery*, 2013, 2013.
- [23] Ligrani, Phillip. Dimple array effects on turbulent heat transfer and flow structure. In *ICHMT DIGITAL LIBRARY ONLINE*. Begel House Inc., 2006.
- [24] Gupta, S., Chaube, A., and Verma, P. “Review on heat transfer augmentation techniques: Application in gas turbine blade internal cooling.” *Journal of Engineering Science & Technology Review*, 5(1), 2012.
- [25] Cho, Hyung Hee, Kim, Kyung Min, and Song, Jiwoon. Applications of impingement jet cooling systems. In *Cooling Systems: Energy, Engineering and Applications*. Nova Science Publishers, Inc., 2011.
- [26] Martin, H. Heat and mass transfer between impinging gas jets and solid surfaces. In *Advances in heat transfer*, volume 13, pages 1–60. Elsevier, 1977.
- [27] Gardon, Robert and Akfirat, J Cahit. “Heat transfer characteristics of impinging two-dimensional air jets.” *Journal of Heat Transfer*, 88 (1):101–107, 1966.
- [28] Bradbury, LJS. “The structure of a self-preserving turbulent plane jet.” *Journal of Fluid Mechanics*, 23(1):31–64, 1965.

- [29] Sparrow, Ephraim M and Wong, TC. "Impingement transfer coefficients due to initially laminar slot jets." *International Journal of Heat and Mass Transfer*, 18(5):597–605, 1975.
- [30] Goldstein, RJ and Behbahani, AI. "Impingement of a circular jet with and without cross flow." *International Journal of Heat and Mass Transfer*, 25(9):1377–1382, 1982.
- [31] Goldstein, Richard J and Seol, WS. "Heat transfer to a row of impinging circular air jets including the effect of entrainment." *International journal of heat and mass transfer*, 34(8):2133–2147, 1991.
- [32] Von Wolfersdorf, J. and Weigand, B. Turbine blade internal cooling - selected experimental approaches, May 2010.
- [33] Park, JS, Han, JC, Huang, Y, Ou, S, and Boyle, RJ. "Heat transfer performance comparisons of five different rectangular channels with parallel angled ribs." *International Journal of Heat and Mass Transfer*, 35(11):2891–2903, 1992.
- [34] Ekkad, Srinath V and Han, Je-Chin. "A transient liquid crystal thermography technique for gas turbine heat transfer measurements." *Measurement Science and Technology*, 11(7):957, 2000.
- [35] Pape, Detlef, Jenkins, Sean, von Wolfersdorf, Jens, Weigand, Bernhard, and Schnieder, Martin. The influence of including a partially smooth section in the 2nd leg of an internally ribbed two pass cooling channel. In *ASME Turbo Expo 2006: Power for Land, Sea, and Air*, pages 633–645. American Society of Mechanical Engineers Digital Collection, 2006.
- [36] Poser, Rico, von Wolfersdorf, Jens, and Semmler, Klaus. Transient heat transfer experiments in complex passages. In *ASME 2005 Summer Heat Transfer Conference collocated with the ASME 2005 Pacific Rim Technical Conference and Exhibition on Integration and Packaging of MEMS, NEMS, and Electronic Systems*, pages 797–804. American Society of Mechanical Engineers Digital Collection, 2005.

- [37] Poser, R, Von Wolfersdorf, J, and Lutum, E. “Advanced evaluation of transient heat transfer experiments using thermochromic liquid crystals.” *Proceedings of the Institution of Mechanical Engineers, Part A: Journal of Power and Energy*, 221(6):793–801, 2007.
- [38] Ekkad, Srinath V, Ou, Shichuan, and Rivir, Richard B. “A transient infrared thermography method for simultaneous film cooling effectiveness and heat transfer coefficient measurements from a single test.” *J. Turbomach.*, 126(4):597–603, 2004.
- [39] Bantel, Thomas E and Mack, David C. Cooling hole inspection, February 17 1987. US Patent 4,644,162.
- [40] Bantel, Thomas E. Apparatus and method for inspecting cooling holes, May 5 1992. US Patent 5,111,046.
- [41] Daniels, Arnold. Nondestructive pulsed infrared quantitative evaluation of metals. In *Thermosense XVIII: An International Conference on Thermal Sensing and Imaging Diagnostic Applications*, volume 2766, pages 185–201. International Society for Optics and Photonics, 1996.
- [42] Carl, Sperling A Becker E. Thermography inspection system for gas turbine blades. In *Proceedings of 7th European Conference on Non-Destructive Testing*, volume 3. ECNDT, 1998.
- [43] Stiglich, JJ, Bishop, CC, Eelkema, TE, Boone, DH, and Daleo, J. “The thermal inertia analysis technique in gas turbine component reliability assessment.” *Materials Solutions’98*, pages 138–144, 1998.
- [44] Lynch, Stephen P and Thole, Karen Ann. “The effect of combustor-turbine interface gap leakage on the endwall heat transfer for a nozzle guide vane.” *Journal of Turbomachinery*, 130(4), 2008.
- [45] Cocchi, L, Facchini, B, Giuntini, S, Winchler, L, Tarchi, L, Innocenti, L, Andrei, L, and Bonini, A. Experimental investigation on impingement array cooling systems through ir thermography. In

- ASME Turbo Expo 2016: Turbomachinery Technical Conference and Exposition*. American Society of Mechanical Engineers Digital Collection, 2016.
- [46] Goodro, Matt, Park, Jongmyung, Ligrani, Phil, Fox, Mike, and Moon, Hee-Koo. “Effects of mach number and reynolds number on jet array impingement heat transfer.” *International Journal of Heat and Mass Transfer*, 50(1-2):367–380, 2007.
- [47] Carlomagno, Giovanni Maria and Cardone, Gennaro. “Infrared thermography for convective heat transfer measurements.” *Experiments in fluids*, 49(6):1187–1218, 2010.
- [48] Nirmalan, Nirm V, Bunker, Ronald S, and Hedlund, Carl R. “The measurement of full-surface internal heat transfer coefficients for turbine airfoils using a nondestructive thermal inertia technique.” *J. Turbomach.*, 125(1):83–89, 2003.
- [49] Bunker, Ronald S, Osgood, Sarah J, and Nirmalan, Nirm V. The determination of in-situ film hole flow rates using a transient thermal inertia method. In *ASME Turbo Expo 2003, collocated with the 2003 International Joint Power Generation Conference*, pages 443–450. American Society of Mechanical Engineers Digital Collection, 2003.
- [50] Heidrich, Peter, von Wolfersdorf, Jens, and Schnieder, Martin. Experimental study of internal heat transfer coefficients in a rectangular, ribbed channel using a non-invasive, non-destructive, transient inverse method. In *ASME Turbo Expo 2008: Power for Land, Sea, and Air*, pages 275–286. American Society of Mechanical Engineers Digital Collection, 2008.
- [51] Egger, Christian, von Wolfersdorf, Jens, and Schnieder, Martin. “Combined experimental/numerical method using infrared thermography and finite element analysis for estimation of local heat transfer distribution in an internal cooling system.” *Journal of Turbomachinery*, 136(6):061005, 2014.

- [52] Egger, Christian, Wolfersdorf, Jens von, and Schnieder, Martin. "Heat transfer measurements in an internal cooling system using a transient technique with infrared thermography." *Journal of turbomachinery*, 135(4), 2013.
- [53] Christensen, Louis E and Mathison, Randall M. Measurement of heat transfer inside a channel using external infrared thermography. In *2018 Joint Propulsion Conference*, page 4430, 2018.
- [54] Incropera F. P., Lavine A. S. Bergman T. L. DeWitt D. P. *Fundamentals of Heat and Mass Transfer*. 1981.
- [55] Petukhov, BS. Heat transfer and friction in turbulent pipe flow with variable physical properties. In *Advances in heat transfer*, volume 6, pages 503–564. Elsevier, 1970.
- [56] Colebrook, Cyril Frank, Blench, T, Chatley, H, Essex, EH, Finnicome, JR, Lacey, G, Williamson, J, and Macdonald, GG. "Correspondence. turbulent flow in pipes, with particular reference to the transition region between the smooth and rough pipe laws.(includes plates)." *Journal of the Institution of Civil engineers*, 12(8):393–422, 1939.
- [57] ASME. "Measurement uncertainty." In *Instrument and apparatus*, vol. ANSI/ASME PTC 19.1-1985 of *Performance Test Code*, 1985.
- [58] Kline, Stephen J. "Describing uncertainty in single sample experiments." *Mech. Engineering*, 75:3–8, 1953.
- [59] Dittus, FW and Boelter, LMK. "Heat transfer in automobile radiators of the tubular type." *International Communications in Heat and Mass Transfer*, 12(1):3–22, 1985.
- [60] Chyu, MK, Hsing, YC, Shih, TI-P, and Natarajan, V. Heat transfer contributions of pins and endwall in pin-fin arrays: effects of thermal boundary condition modeling. In *ASME 1998 International Gas Turbine and Aeroengine Congress and Exhibition*, pages

- V004T09A037–V004T09A037. American Society of Mechanical Engineers, 1998.
- [61] Metzger, DE, Fan, CS, and Haley, SW. “Effects of pin shape and array orientation on heat transfer and pressure loss in pin fin arrays.” *Journal of Engineering for Gas Turbines and Power*, 106(1):252–257, 1984.
- [62] Chyu, MK. Heat transfer and pressure drop for short pin-fin arrays with pin-endwall fillet. In *ASME 1989 International Gas Turbine and Aeroengine Congress and Exposition*, pages V004T08A011–V004T08A011. American Society of Mechanical Engineers, 1989.
- [63] Dabagh, AM Ai and Andrews, GE. Pin-fin heat transfer: Contribution of the wall and the pin to the overall heat transfer. In *ASME 1992 International Gas Turbine and Aeroengine Congress and Exposition*, pages V004T09A022–V004T09A022. American Society of Mechanical Engineers, 1992.
- [64] Li, Qingling, Chen, Zhong, Flechtner, Ulrich, and Warnecke, Hans-Joachim. “Heat transfer and pressure drop characteristics in rectangular channels with elliptic pin fins.” *International Journal of Heat and Fluid Flow*, 19(3):245–250, 1998.
- [65] Yeh, Joseph J and Chyu, Mingking K. Heat transfer of staggered pin fin arrays. In *Graduate student conference*. Carnegie Mellon University, 1998.
- [66] Cunha, FJ and Chyu, Minking K. “Trailing-edge cooling for gas turbines.” *Journal of propulsion and power*, 22(2):286–300, 2006.
- [67] Lyall, Michael E, Thrift, Alan A, Thole, Karen A, and Kohli, Atul. “Heat transfer from low aspect ratio pin fins.” *Journal of Turbomachinery*, 133(1):011001, 2011.
- [68] Rogers, Nathan, Ren, Zhong, Buzzard, Warren, Sweeney, Brian, Tinker, Nathan, Ligrani, Phil, Hollingsworth, Keith, Liberatore, Fred,



- Patel, Rajeshriben, Ho, Shaun, et al. “Effects of double wall cooling configuration and conditions on performance of full-coverage effusion cooling.” *Journal of Turbomachinery*, 139(5):051009, 2017.
- [69] Florschuetz, LW, Truman, CR, and Metzger, DE. Streamwise flow and heat transfer distributions for jet array impingement with cross-flow. In *ASME 1981 International Gas Turbine Conference and Products Show*, pages V003T09A005–V003T09A005. American Society of Mechanical Engineers, 1981.
- [70] Andrei, Luca, Andreini, Antonio, Facchini, Bruno, and Winchler, Lorenzo. “A decoupled cht procedure: application and validation on a gas turbine vane with different cooling configurations.” *Energy Procedia*, 45:1087–1096, 2014.
- [71] Winchler, Lorenzo, Andreini, Antonio, Facchini, Bruno, Andrei, Luca, Bonini, Alessio, and Innocenti, Luca. “Conjugate heat transfer methodology for thermal design and verification of gas turbine cooled components.” *Journal of Turbomachinery*, 140(12):121001, 2018.
- [72] Goldstein, Richard J. Film cooling. In *Advances in heat transfer*, volume 7, pages 321–379. Elsevier, 1971.
- [73] Kinell, Mats, Utriainen, Esa, and Jaksch, Peter. An alternative experimental method for establishing detailed internal heat transfer coefficient distributions of complex cooling geometries using ir thermography. In *ASME Turbo Expo 2014: Turbine Technical Conference and Exposition*. American Society of Mechanical Engineers Digital Collection, 2014.